PIEZOELECTRIC ACTUATORS FOR ULTRASONIC WIRE BONDING APPLICATIONS

SUBMITTED BY

TANG KWAN WAI

FOR THE DEGREE OF

MASTER OF PHILOSOPHY IN PHYSICS

AT

THE DEPARTMENT OF APPLIED PHYSICS

THE HONG KONG POLYTECHNIC UNIVERSITY

OCTOBER 2001

Abstract

Soft lead zirconate titanate (PZT-552 from PKI Inc.) and lead magnesium niobate - lead titanate (0.9PMN-0.1PT) are used in this project for fabricating multilayer actuators because of their large strain responses. PZT-552 has the largest piezoelectric coefficient compared to other PZTs and 0.9PMN-0.1PT has high field induced strain of about 0.1 % under an electric field of 1 kV/mm. Moreover, 0.9PMN-0.1PT is a relaxor ferroelectric material which has no displacement hysteresis.

According to the results of materials characterizations including measurements of the polarization - electric field (P-E) loop, elastic properties, perovskite phase purity, dielectric permittivity and most importantly the strain response, 0.9PMN-0.1PT of 1 wt% excess of lead oxide (PbO) and 1 wt% excess of magnesium oxide (MgO) with a sintering temperature of 1250 °C shows the best results. Hence, this composition and sintering temperature are used in the 0.9PMN-0.1PT multilayer actuator fabrications.

Guided by the result of thermogravimetric analysis (TGA) and by sandwiching the green multilayer samples in-between two brass plates during binder burnout to release heat, the PZT multilayer actuator with 70 active layers and the 0.9PMN-0.1PT multilayer actuator with 60 active layers are fabricated without cracks or delaminations in a faster process. The electrical properties of the two multilayer actuators including impedance measurement of the PZT actuator, dielectric property and P-E loop of the 0.9PMN-0.1PT actuator are presented in this thesis. When voltage is applied to the actuators, they deform and generate displacements due to piezoelectricity or electrostriction. Moreover, for 0.9PMN-0.1PT actuator, piezoelectricity will be induced under a dc bias voltage. According to the piezoelectric effect of PZT and dc bias voltage induced piezoelectric effect of 0.9PMN-0.1PT, the PZT and 0.9PMN-0.1PT multilayer actuators can generate displacements of 3.8 μm and 5.2 μm respectively, under a dc voltage of 100 V.

Because of the advantages of having compact size, lightweight and fast response, the PZT and 0.9PMN-0.1PT multilayer actuators are installed into wireclamps as driving elements. The opening motions of the two modified wireclamps are monitored under dc and ac driving signals in order to show the feasibility of using piezoelectric / electrostrictive actuators in wireclamp applications. Under a dc voltage of 100 V, the PZT and 0.9PMN-0.1PT wireclamps can generate displacements of 35 μm and 53 μm respectively, which are about 10 times that of the driving elements. The displacement can be further amplified by improving the design of the wireclamp or by increasing the number of layers in the actuator.

Acknowledgements

I would like to express appreciation to my supervisor Prof. H. L. W. Chan for her constant support, valuable suggestions and guidance throughout this two-year research study. Grateful acknowledgement is made to my industrial supervisor Dr. Y. M. Cheung of ASM Assembly Automation Ltd. and the Technical Director of ASM, Dr. Peter C. K. Liu for their encouragement and supports.

I also want to express my appreciation to Dr. S. W. Or for his stimulating comments on experimental techniques and technical suggestions.

Thanks are due to the following staff of ASM: Mr. H. L. Li for his efficient assistance in engineering drawing of the wireclamp, Mr. M C. Cheung and Mr. W. Y. Ng for their technical advice in piezoelectric technology.

I would also like to thank the research personnel in the Department of Applied Physics: Dr. N. Chong, Dr. K. W. Kwok and Dr. K. H. Pang for their enlightening discussions in materials sciences and Mr. K. Li and Mr. Y. Zhang for their assistance in materials processing.

Thanks are also due to Dr. R. Zeng, Mr. M. N. Yeung, Mr. K. H. Ho, Ms W. M. Fung, Ms. M. P. Tsang, Mr. K. H. Lam, Mr. Y. T. Or, Mr. D. Y. Wang, Mr. S. F. Wong and Mr. K. C. Cheng for their support and assistance.

I would like to acknowledge the ASM Assembly Automation Ltd. and the Industrial Department of the Hong Kong Special Administrative Region Government for their financial support in this Teaching Company Scheme. Centre for Smart Materials of the Hong Kong Polytechnic University is also acknowledged for the support of equipment.

I want to express my appreciation to my family and to Ms. M. S. M. Lam for their continuous support and understanding.

Finally, I wish to thank God for his presence.

Table of Contents

Chapter 1 Introduction

Chapter 2 Preparation of Ceramic Materials

Chapter 4 Fabrications of Multilayer Actuators

Chapter 5 Characterizations of Multilayer Actuators

Chapter 6 Multilayer Actuators for Wire Clamp Applications

Chapter 7 Conclusions and Future Work

Appendix

List of Figure Captions

List of Table Captions

Chapter 1.
Introduction

1.1 Motivations

Wireclamps currently used in ultrasonic wire bonders are actuated by electromagnetic actuators – e.g. solenoids or voice coils. The solenoid is an electromagnetic type actuator composed of a helical coil of wire that produces a magnetic field when a current flows through the wire. It is an assembly consisting of a single coil, a fixed core of soft iron and a moving soft iron armature. A current carrying coil causes a force on the movable armature in the direction of increasing magnetic flux linkage. The magnetic flux is related to the current and the force is proportional to the square of the current [Kamm 1996]. It is usually used for an on / off device. "Voice-coil" comes from the idea of audio speakers. It is usually used as a position control device such that a feedback system is required. It consists of a movable coil in a gap and a magnet that provides a dc magnetic field in the gap. When a current flows in the coil, the coil experiences a force (Lorentz force) and accelerates. The direction of its motion is determined by the direction of the current in the coil [Chai 1998].

These kinds of actuators can generate large displacements but the long response time (~1 ms) is their disadvantage. As shown in Figure 1.1 a, a wireclamp actuated by a solenoid needs 1.1 ms to open and takes 0.48 ms to close. However, it oscillates for 7-8 ms when it closes. This long delay time is the big drawback. In order to reduce the response time, a new driving mechanism is required in wireclamp actuations. In this project, piezoelectric and electrostrictive actuators are evaluated for wireclamp actuations.

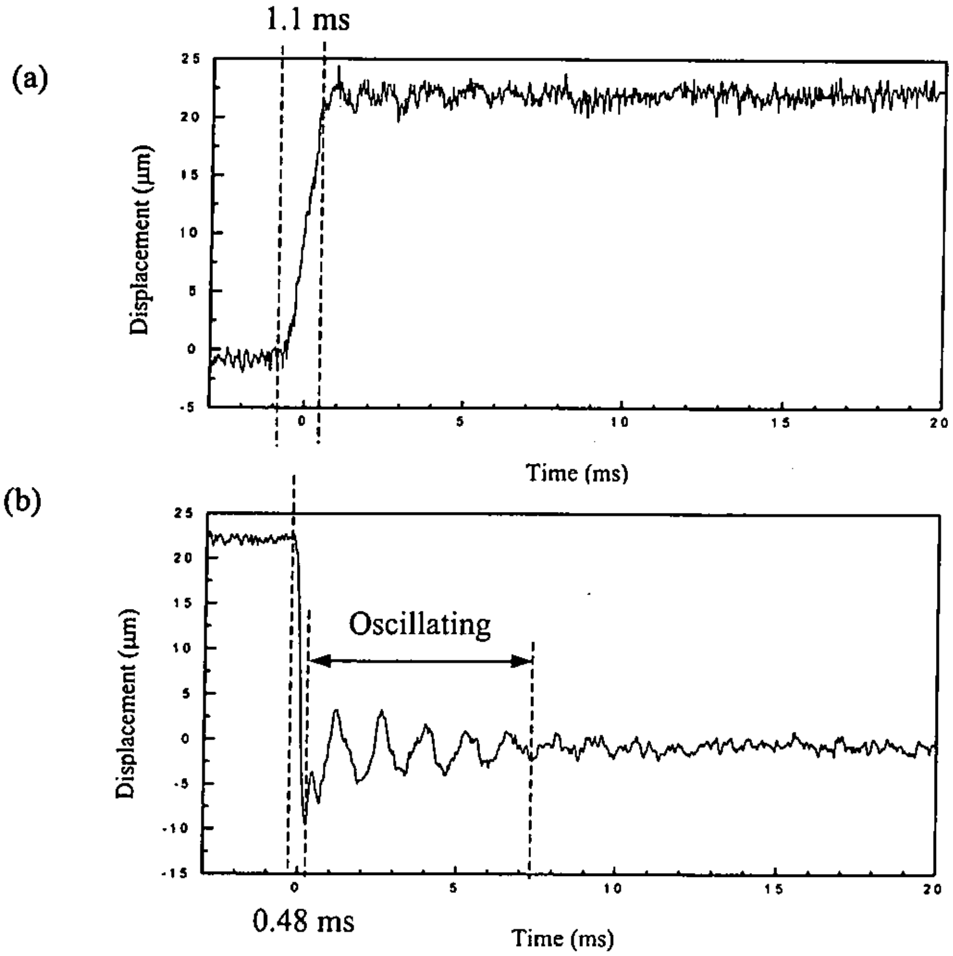

Figure 1.1 (a) Opening and (b) closing behavior of a solenoid-actuated wire clamp as a function of time.

Piezoelectric / electrostrictive actuators are new types of actuator mechanisms for industrial applications. In wire bonding applications, the fast response time of a multilayer piezoelectric / electrostrictive actuator has made it a promising candidate for wire clamping application. However, the small displacement generated is one of its drawbacks as it can generate only about 5-6 μm under 100 V. In order to clamp wires in current thin wire bonding, the wireclamp requires 130 gf clamping force and should be able to open from a minimum of about 60 μm for clamping a 1.25-mil wire to a maximum of 100 μm for clamping a 2-mil wire. Hence, a mechanical amplifier has to be designed in the wireclamp to enlarge the displacement generated by these actuators.

1.2 Piezoelectricity and Electrostriction

1.2.1 Piezoelectricity

The prefix *piezo~* means that it is "pressure" related. It comes from the Greek word which means "to press". When pressure is applied to a piezoelectric material, its crystalline structure will produce a voltage proportional to the pressure; this is called *direct piezoelectric effect.* Conversely, when an electric field is applied, its physical dimensions will change, this is called *converse piezoelectric effect.* This kind of piezoelectric material should have a non-centrosymmetric structure and the commonly used piezoelectric material has the perovskite type crystal structure ABO_3 as shown in Figure 1.2.

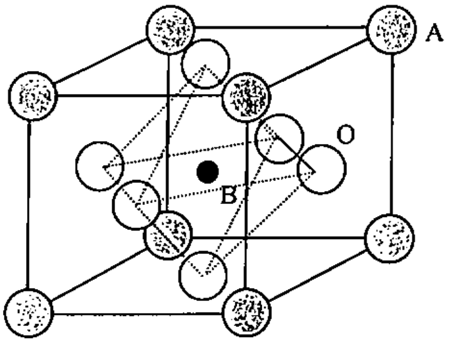

Figure 1.2 Perovskite crystal structure of (ABO_3).

Materials with the structure shown in Figure 1.2 can undergo a phase transition on cooling from a cubic phase to a non-centrosymmetric ferroelectric phase. This phase transition temperature is called the Curie temperature T_c.

The material exhibits piezoelectricity after a large electric field is applied to the material such that the dipoles are aligned in one direction. This is the "poling" process. After poling, the material becomes anisotropic. Piezoelectric effect allows the material to generate a voltage when it is subjected to a compressive or tensile force (Figure 1.3a) or its physical dimension will change along the poling axis when the material is subjected to an electric field lower than the poling field (Figure 1.3b).

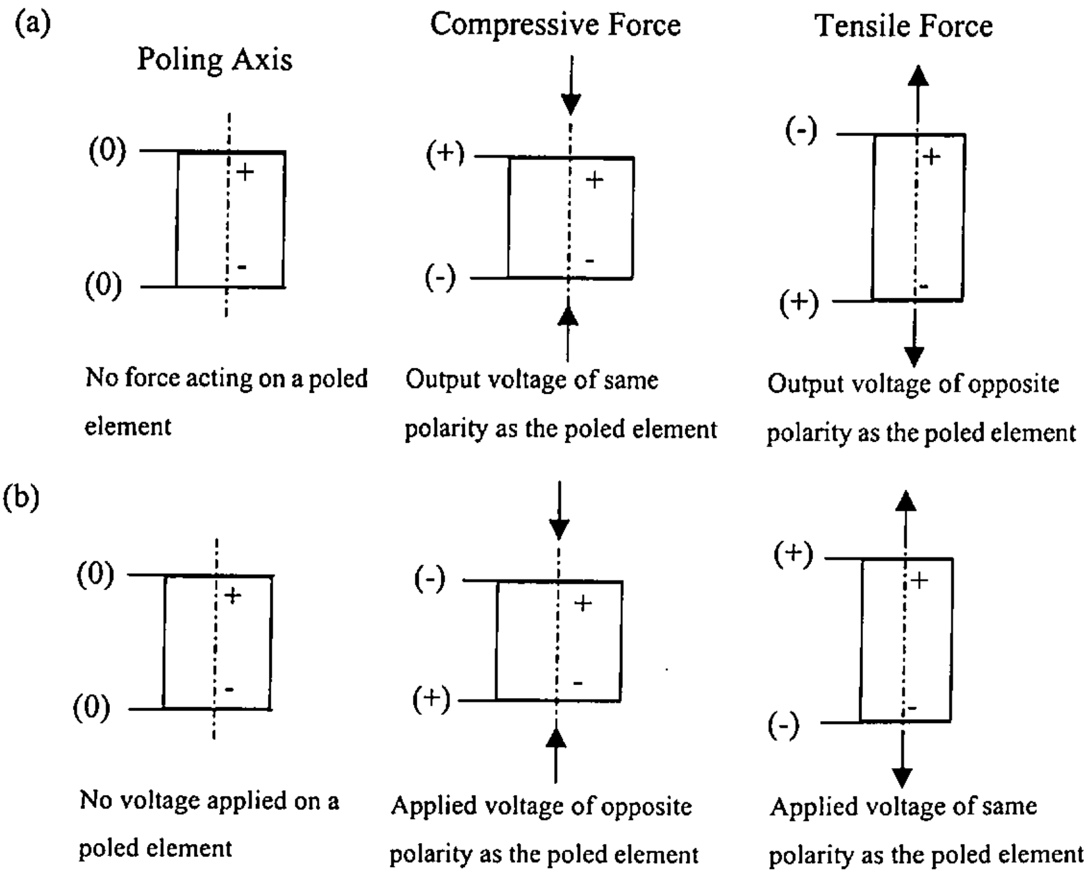

Figure 1.3 (a) Direct and (b) converse piezoelectric effect.

The following two equations can be used to describe the electrical and mechanical variables in linear piezoelectric theory:

$$S_{ij} = s^{E}_{ijkl}T_{kl} + d_{mij}E_m \tag{1.1}$$

$$D_i = d_{ikl}T_{kl} + \varepsilon^{T}_{ij}E_j \tag{1.2}$$

where S_{ij} is the strain matrix, s^{E}_{ijkl} is the elastic compliance matrix under short circuit condition, T_{kl} is the elastic stress matrix, d is the piezoelectric coefficient matrix, E (E_m, E_j) is the electric-field matrix, D_i is the dielectric displacement matrix and ε^{T}_{ij} is the dielectric permittivity at constant stress. The first equation describes the converse piezoelectric effect and the second equation describes the direct piezoelectric effect. [Hom 1994]

1.2.2 Electrostriction

The electrostrictive effect is a nonlinear coupling effect between the elastic strain and electrical field. This effect is present in all material, regardless of the symmetry. If an electric field is applied to a material, the material will change its physical dimensions and this strain response is proportional to the square of the applied electric field. The deformation is independent of the polarity of the applied electric field. The electrostrictive strain S_{ij} can be expressed as [Ealey 1990]:

$$S_{ij} = s^{E}_{ijkl}T_{kl} + M_{ijmn}E_mE_n \tag{1.3}$$

or

$$S_{ij} = s^{P}_{ijkl}T_{kl} + Q_{ijmn}P_mP_n \tag{1.4}$$

where s_{ijkl} is the elastic compliance under appropriate stress, T_{kl} is the elastic stress, E_m and E_n are the electric fields, M_{ijmn} and Q_{ijmn} are the fourth rank electrostrictive constants, P_m and P_n are the polarizations. Lead magnesium niobate (PMN) is one of the commonly used electrostrictive materials. [Swartz 1982, Shrout 1987]

1.3 0.9PMN-0.1PT Ceramic Material

0.9PMN-0.1PT is a relaxor ferroelectric material. Being different from normal ferroelectrics (eg. PZT), relaxor ferroelectrics have a broad-diffuse and dispersive phase transition. The temperature of maximum dielectric permittivity is denoted by T_m which will shift to a higher value but of a smaller dielectric maximum when the measuring frequency is increased. Also, its remanent polarization will gradually decrease to zero when the temperature increases above T_m. (Figure 1.4) [Shrout 1990]

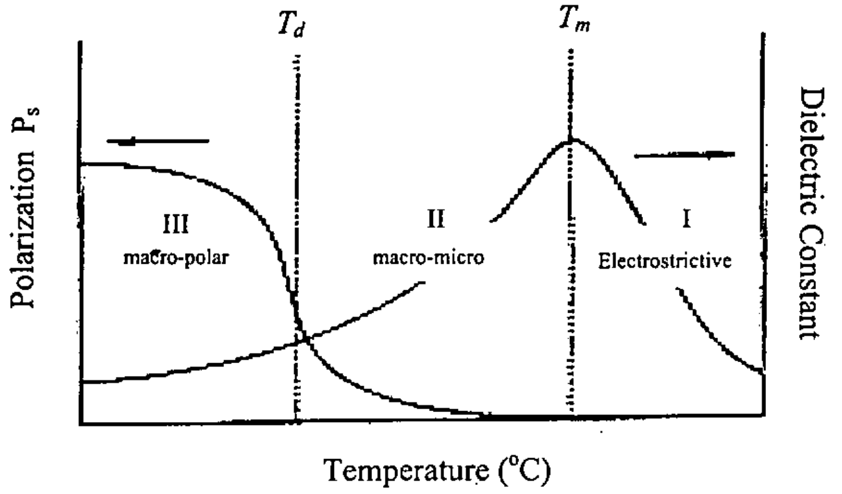

Figure 1.4 Dielectric and polarization behavior of 0.9PMN-0.1PT as a function of temperature. [Shrout 1990]

For 0.9PMN-0.1PT, its T_m is around room temperature. Since its depolarizing temperature T_d is well below T_m, it cannot be poled at room temperature at which it shows no piezoelectric effect. But when a dc bias voltage is applied, polarization is induced and it exhibits the piezoelectric effect. The induced piezoelectric strain coefficient d_{ij} can be expressed as [Shrout 1987, Damjanovic 1998]:

$$d_{ij} = 2\varepsilon_o\varepsilon_i Q_{ij} P_i \quad (1.5)$$

where ε_o is the permittivity of free space, ε_i is the dielectric permittivity, Q_{ij} is the two rank electrostrictive constant and P_i is the polarization. In general, the induced piezoelectric effect is small in most materials. 0.9PMN-0.1PT is an exception because it has a phase transition near room temperature. Hence, if a 0.9PMN-0.1PT ceramic is driven by an ac electric field together with a suitable dc bias field, its strain response will be much greater than that driven by an ac signal only. This strain response which combines the electrostrictive and induced piezoelectric effects will be greater than that of common piezoelectric materials like PZTs.

1.4 Piezoelectric Actuators

Actuator is a device that can produce a mechanical movement. For the wireclamp application, the clamping arms are opened by an applied electrical signal. Electrical energy supplied to the actuator is transformed to mechanical energy due to piezoelectric or electrostrictive effect and hence pushing the clamping arms to open.

Actuators can be classified into two categories, according to the difference in the driving methods and to the nature of their strain responses. (1) *Rigid displacement device* is the actuator which displaces unidirectionly by a dc field; (2) *resonating displacement device* is the actuator which is driven by an ac field at its mechanical resonant frequency such that the strain alternates (ultrasonic motors) [Uchino 1997].

The rigid displacement devices can also be divided into two categories. The first type is the *servo displacement transducer* (positioner) in which the actuator is controlled by a feedback control system. The second type is the *pulse-driven actuator*, which is operated by an on / off-switching mode. For the wire-clamp application, the actuator is driven by a specified electrical pulse signal. Therefore, *pulse-driven actuator* is being used in this application [Uchino 1997].

There are various types of solid-state actuators: *cymbal*, *moonie*, *bimorph*, *inchworm*, *multilayer* [Ealey 1990, Uchino 1997] etc... Cymbal [Dogan 1996] and moonie [Xu 1991] are ceramic-metal composites. The metal parts act as a displacement amplifier, whereas a bimorph is composed of two transverse-expander plates which can also generate large displacement. However, their low force capability and slow response time are their disadvantages. "Inchworm" is a linear motor that accumulates small steps with respect to time. The main advantage of this type of actuator is the high resolution per step, (1 nm), but its movement is quite slow, (0.2 mm/s) [Uchino 1995]. Multilayer actuator is composed of many simple ceramic sheets which stacked mechanically in series and connected electrically in parallel. The model of a multilayer piezoelectric actuator is shown in Figure 1.5.

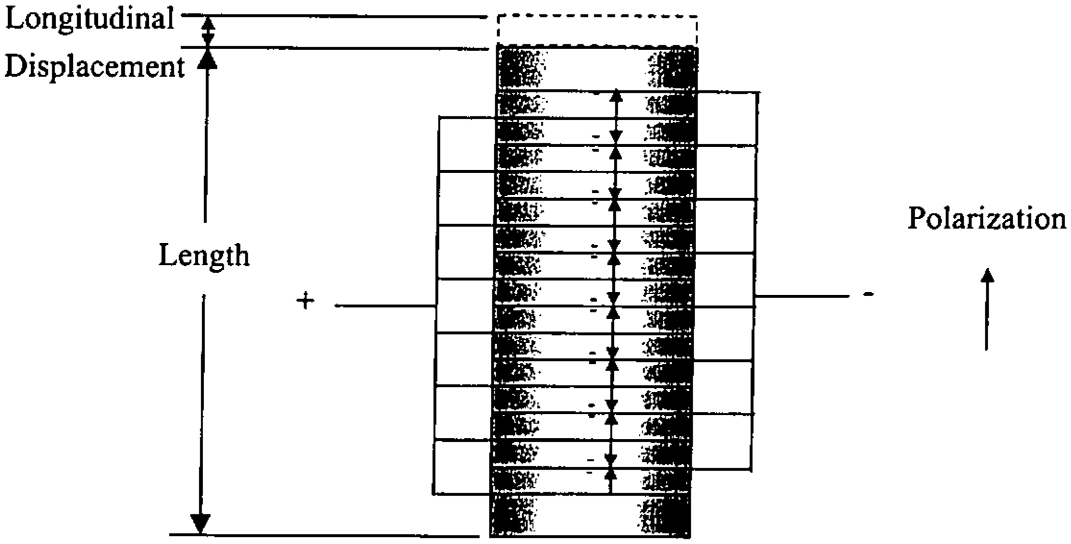

Figure 1.5 A simple model of multilayer actuators

Although the multilayer actuator is costly and its generated displacement is comparatively small, its high force capability, fast response time and good reliability have made it a suitable candidate for wireclamp applications. Other than wireclamp devices, multilayer actuators are widely used in many different fields; various applications of this type of actuator are listed in Table 1.1.

Table 1.1 Examples of applications of multilayer piezoelectric actuators. [Tokin 1995]

Apparatus	**Examples of Applications**
Precision machinery, mechatronics	*Sewing machine, robot, vibration of parts feeder, positioning of equipment, pressure sensor*
Semiconductor manufacturing system	*Dicing saw, positioning of etching apparatus and various equipment, vibration*
Household electrical appliance, audio equipment	*Pump, speaker*
VTR, VD (visual equipment)	*Autofocusing, vibration control*
Printer	*Paper feeder (transducer), ink drive driver*
Computer, OA equipment	*Pressure sensor, transducer (head tracking) for memory device (data storage or other)*
Optical equipment, PPC	*Positioning of stage, autofocusing, vibration*
Communications	*Polarization control*
Medical equipment	*Micropump, ultrasonic transducer*
Measuring instrument	*Pressure sensor, acceleration sensor, fine positioning*
Automobile	*Vibration control*
Camera	*Autofocusing*
Valve	*Electropneumatic proportional control valve*

1.5 Literature Review on Using Multilayer Actuators in Wire Bonding Applications

One of the Japanese wire-bonding companies, Shinkawa, has conducted a series of research projects on the area of piezoelectric wireclamps. They have several patents on this topic in the United States: 5323948 [Nobuto 1994], 5388751 [Kuniyuki 1995], 5435477 [Minoru 1994], and 5746422 [Minoru 1998].

According to patent US5323948 by Shinkawa, the wire clamper is a pair of clamping arms used in wire bonding apparatus being opened and closed via the electric strain effect or magnetic strain effect of a piezoelectric or magnetostrictive element. The clamper expands when the piezoelectric element is energized. This lightweight wire clamper has improved response characteristics and has provided a steady clamping load. Since the clamping load is obtained by the driving force of a piezoelectric element, the clamping parts will clamp wire steadily even when the bonding head moves at a high speed. [Nobuto 1994] (The design is shown in Appendix A.1)

The second patent of the Shinkawa wireclamp US5388751 is based on the same wire clamp design as the previous patent. The wire clamp is actuated by the electrostrictive strain effect or magnetostrictive strain effect of an actuator. Furthermore, a temperature compensation component is connected to the piezoelectric element to correct for the fluctuations in the clamping load imposed on the clamping elements by temperature changes in the clamp. [Kuniyuki 1995] (The design is shown in Appendix A.1)

Based on the two previous patents, Shinkawa used the same design, but added a claim for the load adjustment screw which was installed at the end of the wire clamper to set an initial clamping load for the clamping elements (US5435477). [Minoru 1994] (The design is shown in Appendix A.1)

The invention stated in patent US5746422 by Shinkawa is a new type of wire clamp which can greatly reduce the bending or deformation of the contact plate so that destruction of the piezoelectric element is prevented. This can be done by introducing a pressure adjustment screw, which applies a prescribed pressure to the piezoelectric element via a contact plate, where the contact plate is connected to a screw mounted element. The pressure adjustment screw capable of expansion and contraction are located between the contact plate and the screw mount element. [Minoru 1998] (The design is shown in Appendix A.2)

Other than Shinkawa, another Japanese company, Matsushita Electric Industrial Co. Ltd., also filed an U.S. patent (US5314175) [Akihiro 1994] describing a piezoelectric wire-clamping device. The invention of a wire-clamping device by Matsushita comprises a fixed arm and a movable arm. The movable arm faces the fixed arm with a small gap in between. When applying a voltage across the piezoelectric element, it will deform and will bend the movable arm towards the fixed arm, and the wire will be clamped by the two arms. [Akihiro 1994] (The design is shown in Appendix A.3)

Toshiba Corp. [Tsuyoshi 1998], Hitachi Ltd. [Kenji 1982], Kaijo Corp. [Tetsutaka (A), (B) 1997] filed their patents in Japanese. They have emphasized the use of wire clamp with a piezoelectric element.

The wire clamp invented in patent JP10242196 by Toshiba is a pair of metal clampers consisting of two piezoelectric elements. The two piezoelectric elements are located between the movable elements and the metal clampers and are arranged into a lattice shape. A driving unit which opens or closes the metal clampers along with the movable elements, and a control unit which controls the driving unit electrically, are provided. [Tsuyoshi 1998] (The design is shown in Appendix A.4)

The patent JP57159034 by Hitachi was released in 1/10/82; it was the first one that introduced a piezoelectric element to the wire-clamping device. With respect to that design, the piezoelectric element is placed in the vicinity at the end of one branch, and a clamping plate is mounted at the position facing the element at the other branch. Once the electric field is applied to the element, it elongates longitudinally at a high speed by the electrostrictive or magnetostrictive characteristics. [Kenji 1982] (The design is shown in Appendix A.5)

The design in patent JP09051012 by Kaijo claims that it can provide fine adjustment of clamping force by using the piezoelectric element. When voltage is applied through the element, it expands and moves in the closing direction. Therefore, the gap between the holding sections can be set with higher accuracy and alignment can be realized easily. [Tetsutaka (A) 1997] (The design is shown in Appendix A.6)

The other wire clamp designed in patent JP09051013 by Kaijo is driven by a generating vibrational force from a piezoelectric element. It makes use of a lever mechanism. When both members are holding the wire, the collision energy required can be reduced by changing the distance between the fulcrum point and the working point of the two clampers. Consequently, damage of the wire can be prevented. [Tetsutaka (B) 1997] (The design is shown in Appendix A.7)

Table 1.2 shows the patents on piezoelectric wire clamp owned by the various companies. It is thus seen that using a piezoelectric element to drive a wire clamp is an actively pursued trend in wire bonding applications.

Table 1.2 Patents of piezoelectric wire clamps for wire bonding.

Patent number	Issued Date	Applicant	Title
US5323948	28/6/1994	Kabushiki Kaisha Shinkawa	*Wire Clamper*
US5388751	14/2/1995	Kabushiki Kaisha Shinkawa	*Wire Clamper*
US5435477	25/7/1995	Kabushiki Kaisha Shinkawa	*Wire Clampers*
US5746422	5/5/1998	Kabushiki Kaisha Shinkawa	*Clamping Device*
US5314175	24/5/1994	Matsushita Electric Industrial Co.	*Wire Clamping Device and Wire Clamping Method*
JP10242196	11/9/1998	Toshiba Corp.	*Wire Bonding Apparatus*
JP57159034	1/10/1982	Hitachi Ltd.	*Wire Clamping Device*
JP09051012	18/2/1997	Kaijo Corp.	*Wire Clamping Mechanism and Wire Bonding Apparatus comprising the same mechanism*
JP09051013	18/2/1997	Kaijo Corp.	*Wire Clamping Mechanism and Wire Bonding Apparatus comprising the same mechanism*

1.6 Scope of Project

The present work on piezoelectric and electrostrictive actuators for ultrasonic wire bonding applications is presented as follows:

In Chapter 2, the fabrication processes of PZT and 0.9PMN-0.1PT ceramics are presented. The method to suppress pyrochlore phase formation in fabricating 0.9PMN-0.1PT ceramic is discussed in this Chapter.

Materials characterizations of PZT and 0.9PMN-0.1PT ceramics presented in Chapter 3 include density measurements using the Archimedes' principle, hysteresis measurements by the Sawyer Tower bridge, elastic properties measurements by the ultrasonic immersion method, impedance measurements of PZT, dielectric measurements, X-ray diffraction and grain size observation by SEM of 0.9PMN-0.1PT.

Chapter 4 presents the fabrication technology of multilayer actuators using the PZT and 0.9PMN-0.1PT ceramic materials. Modifications of the binder burnout process are described in this Chapter.

Multilayer actuator characterizations are presented in Chapter 5. In this Chapter, effective densities of the two actuators are measured. Microstructures of the actuators are analyzed, and impedance measurement of the PZT multilayer actuator is discussed. Dielectric behavior and ferroelectric hysteresis loop of 0.9PMN-0.1PT multilayer actuator are presented. Finally, displacement measurements of the two actuators are compared.

Descriptions on the wire-clamping mechanism and installations of the two actuators into the metal parts of the wireclamp are presented in Chapter 6. Evaluations of the opening displacements of the wireclamps by using the Fotonic sensor and the vibrometer are also presented.

Conclusions and suggestions for future work are given in Chapter 7.

1.7 Original Contributions

To the best of our knowledge, the original contributions reported in this research are:

The optimum fabricating condition of 0.9PMN-0.1PT ceramics was found by using the strain response as the figure of merit. The ceramic composition and sintering temperature were optimized to give the highest strain response under the same dc bias field.

In this research, a new method is developed to speed up the binder burnout process in multilayer actuator fabrications. Firstly, the binder decomposition profile was measured by thermogravimetric analysis (TGA). The temperatures at which there were rapid gas evolution were taken as "hold points" during binder burnout. Hence, the time and temperature for the process could be controlled more accurately. Secondly, the binder burnout process was performed by sandwiching the sample in-between two brass plates so as to release heat during binder burnout. This has greatly shortened the time required for the binder burnout process. This result has been published in Ferroelectrics.

Displacement of the PZT and 0.9PMN-0.1PT multilayer actuators are characterized and compared under dc and ac driving voltages. Accordingly, the effective piezoelectric coefficient of the two multilayer actuators and effective electrostrictive coefficient of the 0.9PMN-0.1PT actuator were found. The results have been summarized in a paper entitled "Longitudinal Strain Response of a 0.9PMN-0.1PT Multilayer Actuator" and submitted to the journal "Materials Chemistry and Physics (Elsevier)".

The wireclamps installed with the PZT and 0.9PMN-0.1PT multilayer actuators were evaluated. The displacement characteristics of the wireclamps driven by the two actuators were investigated and compared. The magnification factors of the wireclamps were also found.

Chapter 2.

Preparation of Ceramic Materials

2.1 Introduction

Two ceramic materials PZT-552 and 0.9PMN-0.1PT were used in fabricating the multilayer actuators. Before using the materials for multilayer fabrications, their material parameters should be characterized. This Chapter discussed the preparation of ceramic samples used in material parameter characterizations.

2.1.1 Lead Zirconate Titanate (PZT)

Modified lead zirconate titanate powder, PZT-552 (Navy type VI) supplied by Piezo Kinetics Inc., USA was used in this project. According to the commercial specifications, PZT-552 has the largest piezoelectric charge coefficients d_{33} and d_{31}. Especially the longitudinal piezoelectric coefficient d_{33}, it is essential for determining the longitudinal strain produced by a multilayer actuator when electric field is applied along its poling direction. Table 2.1 is a list of selected properties of 4 commercial PZT materials. PZT-552 has been widely used in fabricating sensitive receivers, hydrophone, ink jet printers and used in fine movement control. However, aging and low applicable temperature range are its weaknesses.

Table 2.1 Some important electrical properties of four commercial PZT materials [Piezo Kinetics Inc. 2001].

	Dielectric permittivity K^T_{33}	**Longitudinal coupling factor k_{33}**	**Piezoelectric coefficient d_{33} (10^{-12} m/V)**	**Piezoelectric coefficient d_{31} (10^{-12} m/V)**
PZT 402	1250	0.67	275	-120
PZT 502	1800	0.69	400	-175
PZT 552	**3400**	**0.75**	**593**	**-274**
PZT 802	1000	0.61	220	-100

2.1.2 0.9 Lead Magnesium Niobate – 0.1 Lead Titanate (0.9PMN-0.1PT)

The solid solution of lead magnesium niobate-lead titanate used in this study has a composition of $0.9Pb(Mg_{1/3}Nb_{2/3})O_3$-$0.1PbTiO_3$ (0.9PMN-0.1PT). It is prepared by the mixed oxide method. Care must be taken to ensure that the compositions and fabrication procedure are correct. Otherwise, a lead niobate-based pyrochlore phase is formed [Swartz 1984] which will deteriorate the overall dielectric performance as dielectric permittivity of the pyrochlore phase is about 200 only [Chen 1990].

According to the literature, some methods are suggested for fabricating stoichiometric perovskite 0.9PMN-0.1PT. From Swartz and Shrout [Swartz 1982], they suggested a columbite-precursor method which pre-reacted magnesium oxide and niobium pentoxide to form a columbite magnesium niobate prior to reacting with lead oxide and titanium oxide. If lead oxide and titanium oxide reacts with the columbite to form pyrochlore, it has to release niobium pentoxide first, thus the pyrochlore formation will be inhibited [Shrout 1987].

Another suggestions to suppress the pyrochlore phase formation are to add excess amount of lead oxide and magnesium oxide [Guha 1988, Gupta 1995, Kang 1988, Kusumoto 1998, Villegas (A), (B) 1999, Wang 1990]. It is important to control the amount of lead oxide excess. A large amount of excess lead oxide in the grain boundary can reduce the dielectric permittivity and mechanical strength and cause aging [Kang 1988]. Some of the literatures revealed that if MgO exists only in the stoichiometric amount, it is hard to produce a single perovskite phase in the solid solution [Kusumoto 1998]. Although it is hard to prove that excess MgO can increase the dielectric permittivity, it is generally believed that it decreases the amount of grain boundaries which contained the pyrochlore [Kusumoto 1998]. But excessive amount of MgO would cause detrimental effects since its precipitation would form another phase which is MgO rich.

2.2 Fabrication of PZT Ceramics

2.2.1 Dry Pressing

Samples for materials characterizations in Chapter 3 are all in disc form. The first fabrication step was dry pressing to densify the sample before binder burnout and sintering. It was accomplished by placing the ceramic powder into a mould and then a uniaxial pressure of about 185 MPa was applied for several minutes. This pressure is large enough to drive out the excess air to form a closely packed disc.

Lubricant was used to improve the flow in the die and to reduce the chance of sticking onto the die. The as-supplied powder already contained the required amount of binder and there is no need to add binder prior to pressing [Richerson 1982]. Figure 2.1 shows the ceramic powder inside the pressing mould during pressing. Finally, the ceramic sample was taken out for another process.

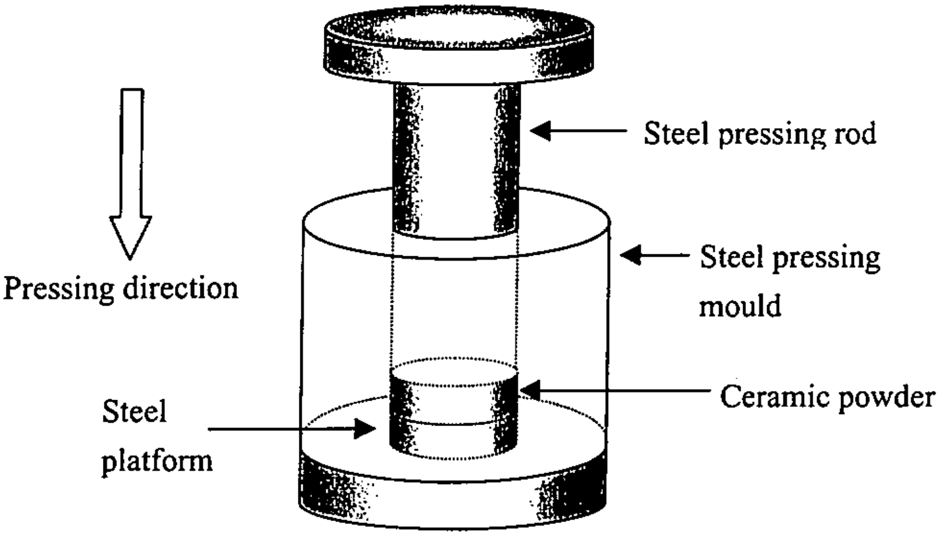

Figure 2.1 Schematic diagram of dry pressing a PZT ceramic disc.

2.2.2 Binder Burnout and Sintering

Binder burnout and sintering are essential procedures for producing ceramic samples. Since the pressed disc contained PVA (polyvinyl alcohol) which will react with lead oxide to form another compound other than PZT, so it is necessary to burn out the binder before sintering. During the burnout process, the binder can be burnt away at 550 °C for an hour using the Lindberg / blue furnace. The ceramic sample was placed inside the crucible with a little air gap between the crucible and the alumina cover, so that the organic components could be evaporated away from the sample during the process (Figure 2.2).

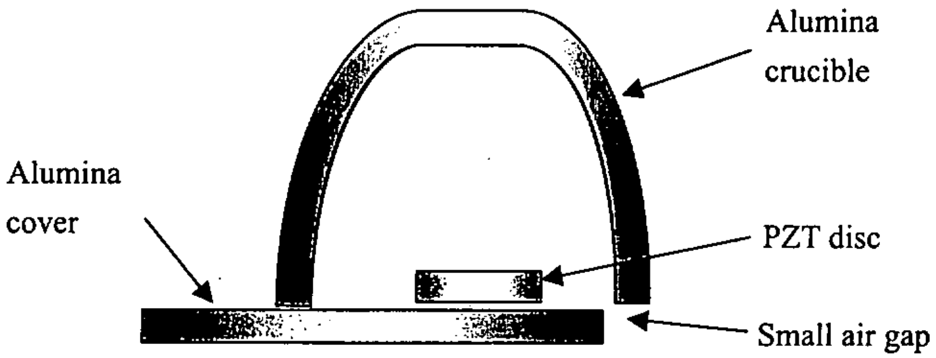

Figure 2.2 Schematic diagram of a PZT ceramic in a crucible for binder burnout.

The binder burnout schedule is shown in Figure 2.3. Temperature of the furnace was set at 550 °C with a rising rate of 3 °C/min, and was kept at that temperature for an hour so as to fire away the binder. Then the temperature was raised to 790 °C with the same speed and was kept for an hour to allow the binder to completely evaporate. After the 1-hour binder burnout process was completed, the furnace was switched off to allow natural cooling.

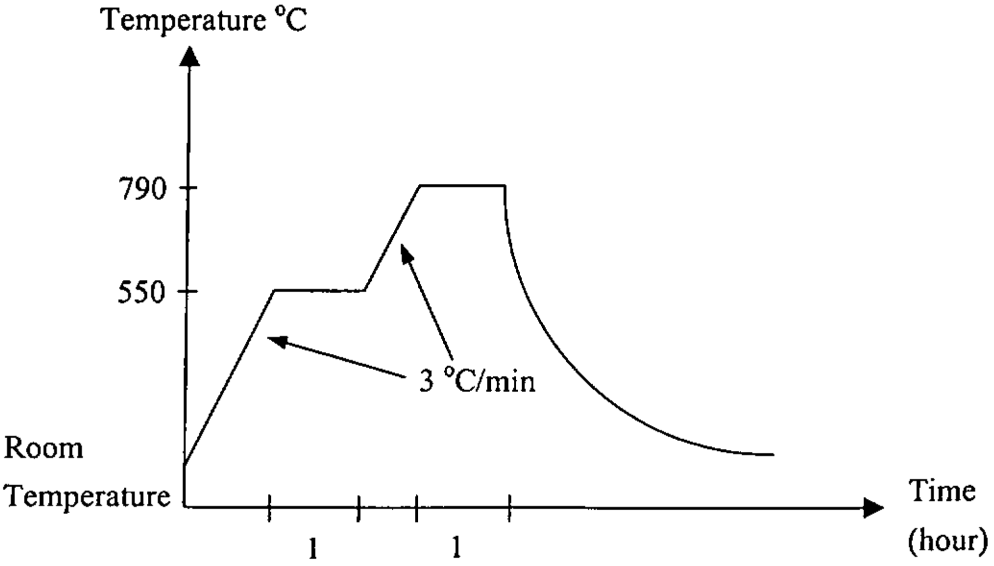

Figure 2.3 Binder burnout schedule of PZT ceramic.

Lead will diffuse out of the sample when the temperature is higher than 888 °C, which will consequently cause the loss of lead content of the sample. Therefore, the sample must be insulated from the outer atmosphere during sintering. The most efficient way is to immerse the sample in the sintered PZT ceramic powder when placed in the crucible during sintering. Moreover, the crucible should be totally covered by the alumina cover (Figure 2.4). The PZT ceramic disc was sintered at 1285 °C using the programmable Carbolite RHF furnace. The temperature profile during sintering is shown in Figure 2.5. The thickness shrinkage of the sintered sample is about 20 % and its radial shrinkage is about 13 %-14 %.

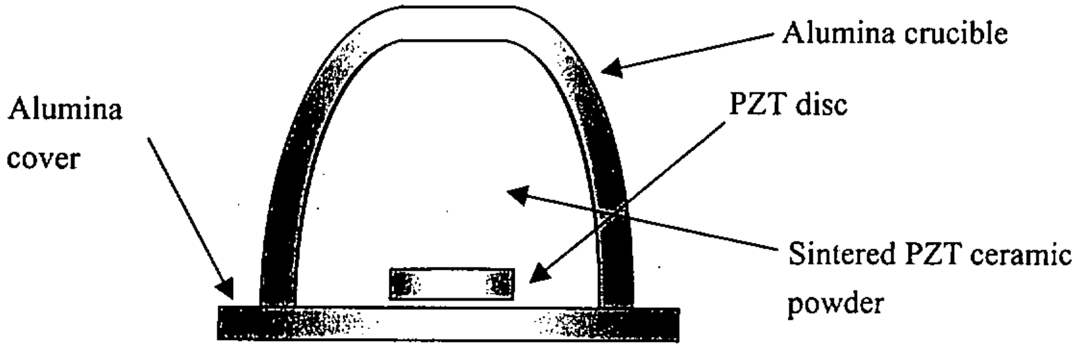

Figure 2.4 Schematic diagram of a PZT sample covered by ceramic powder during sintering.

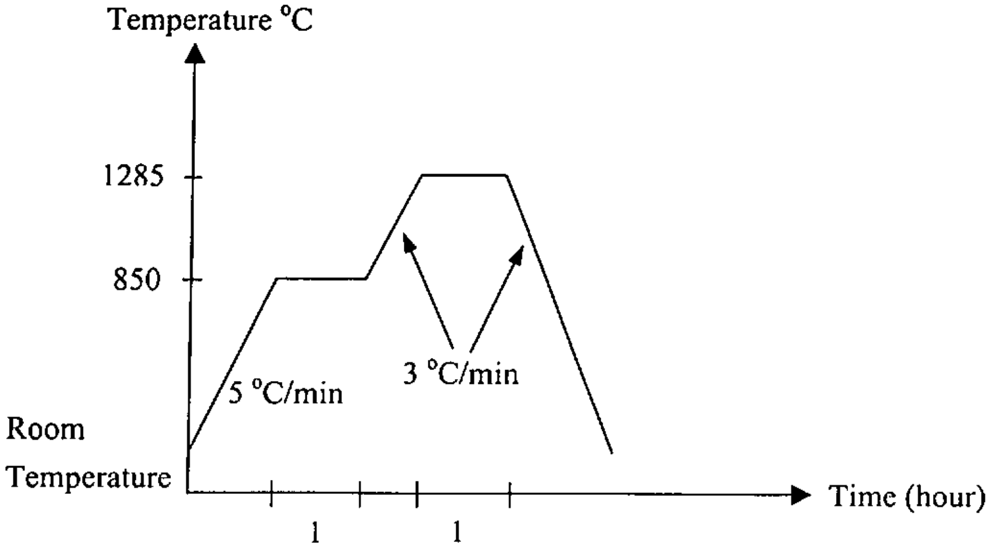

Figure 2.5 Sintering schedule of PZT 552 sample.

2.2.3 Poling and Short-Circuit Annealing

A sintered PZT disc does not show any piezoelectric property before poling. The crystals or grains are all randomly oriented, and the material is isotropic, so no piezoelectric effect occurs. When a large dc electric field is applied, the grains will then be oriented in one direction, and the ceramic becomes anisotropic, so that a permanent polarization occurs. The process to induce this permanent polarization is called poling.

An air-dried G3691 Agar Scientific silver-paint was used as electrodes on the top and bottom surfaces of the sintered PZT sample. The PZT sample was immersed in silicone oil which was kept in a programmable MEMMERT oven at about 130 °C and was held for 15 minutes to stabilize the temperature before a voltage was applied. The poling circuit is shown in Figure 2.6.

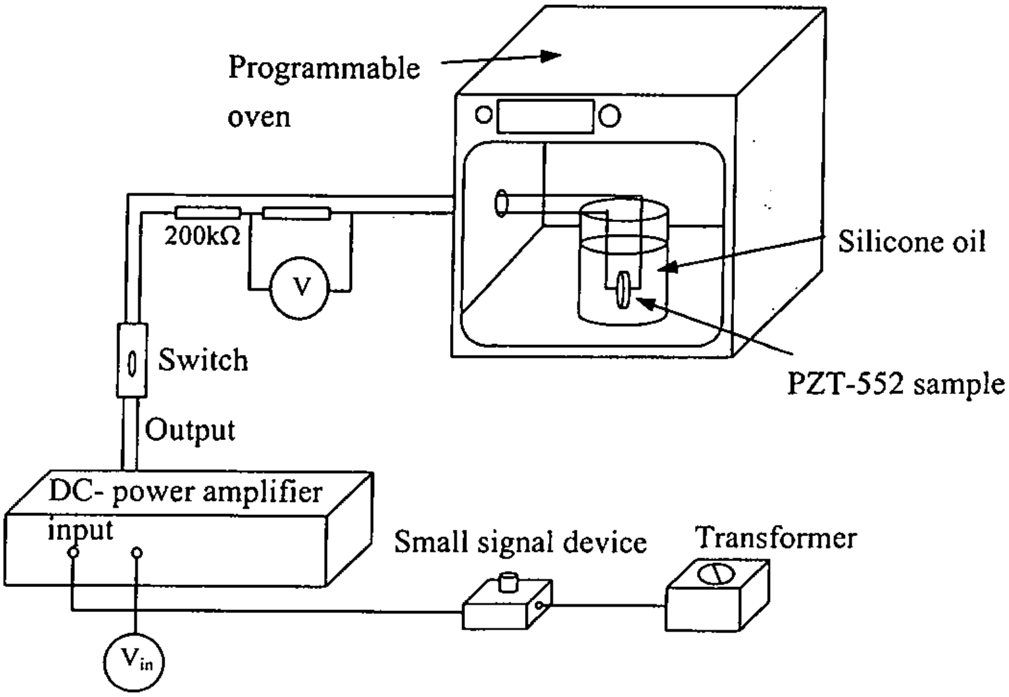

Figure 2.6 Circuit for D.C. poling of PZT ceramic disc.

A poling field of 2 kV/mm was applied in the thickness direction of the ceramic disc. The signal generator was turned in a clockwise direction to V_{in} which is the input voltage to the TREK 609C-6 high voltage D.C. power amplifier. Voltage required for poling is 1000 V_{in}; it can be calculated by using the following equation.

$$Poling\ voltage = 1000V_{in} = 2kV / mm \times Thickness\ of\ sample \qquad (2.1)$$

After the signal generator has been tuned to the required voltage, it was held for 20 minutes, and then the heater was switched off but the same poling field was maintained. When the temperature was decreased to 70 °C, the field was switched off.

After poling, the domain orientation and surface charges induced on the surface caused induced stress in the sample. After a period of time, the piezoelectric properties of the sample may be weakened by the stress relief. This is called the aging effect. In order to speed up this aging effect, sample should be short-circuit annealed. The poled sample was packed by aluminum foil and was placed inside a programmable oven at about 45 °C for 1 day. The moderate temperature enhances charge mobility. The aluminum foil connected both electrodes of the sample which provide a short-circuit condition. Then the stress in the sample can be released and the piezoelectric property is stabilized.

2.3 Fabrication of 0.9PMN-0.1PT Powders

2.3.1 Formation of Magnesium Niobate

In order to suppress the pyrochlore phase formation, the columbite precursor method was used instead of the traditional mixed oxide method. Proper amount of MgO (Acros Organics, New Jersey, USA, 99 %) and Nb_2O_5 (SCR, Shanghai, China, 99.5 %) was weighted and mixed together by ball milling in ethanol for 4 hours. After drying out the mixed powders, it was put into an alumina crucible for calcination. Two calcination temperatures were selected for comparison, 1050 °C and 1100 °C. Powder was calcined from room temperature to 1050 °C / 1100 °C at a rate of 5 °C /min and was kept for 4 hours and then the temperature was dropped to room temperature at the same rate in a Carbolite RHF furnace. Figure 2.7 shows the X-ray diffraction (XRD) pattern of the magnesium niobate (MN) calcined at (a) 1050 °C and (b) 1100 °C for 4 hours. It was conducted by a Philips Analytical X-Ray Diffractometer and the PC-APD diffraction software which is a line type scanning program.

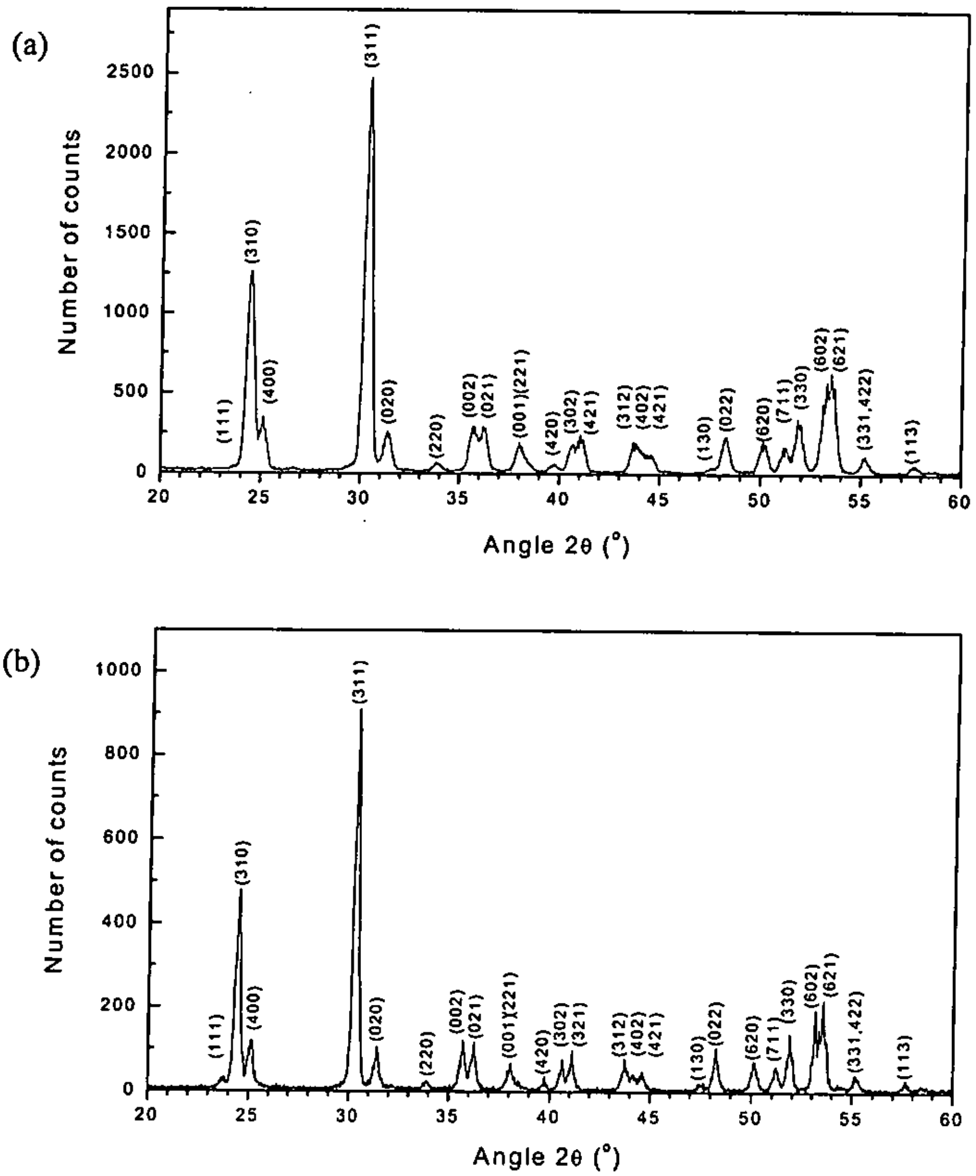

Figure 2.7 XRD pattern of magnesium niobate calcined at (a) 1050 °C and (b) 1100 °C for 4 hours.

Peaks shown in Figure 2.7b are sharper than those in Figure 2.7a, hence, 1100 °C was selected to be the calcination temperature because a more complete reaction resulted at this temperature.

2.3.2 Mixing and Ball Milling

Mixing is a very important procedure in ceramic fabrication. Piezoelectric and dielectric properties will be deteriorated if the solid solution is inhomogeneous. According to the chemical formula of lead magnesium niobate- lead titanate, $0.9Pb(Mg_{1/3}Nb_{2/3})O_3$-$0.1PbTiO_3$, the mole ratio of lead oxide (PbO) to magnesium niobate (MN) to titanium oxide (TiO_2) is 1:0.3:0.1. Although the columbite precursor method was used to suppress the pyrochlore phase formation, the final composition would also depend on the lead content. Lead will be lost during sintering (>888 °C), therefore, excessive lead oxide is essential for compensating lead loss. Some literature [Kang 1988, Kusumoto 1998] stated that excess magnesium oxide could contribute to the homogeneity of 0.9PMN-0.1PT. To try out those methods suggested which could suppress the pyrochlore formation, three different compositions were used to find out the composition that could achieve optimum properties. They were:

1. 0.9PMN-0.1PT with 1 wt% excess of MgO
2. 0.9PMN-0.1PT with 1 wt% excess of MgO and 1 wt% excess of PbO
3. 0.9PMN-0.1PT with 1 wt% excess of MgO and 2 wt% excess of PbO

Exact amount of PbO (Acros Organics, New Jersey, USA, 99.9 %), TiO_2 (Farco Chemical Supplies, Beijing, China, 99 %) and the calcined $MgNb_2O_6$ were weighted with different excess amount of MgO and PbO. After that, they were put inside ethanol to ball-mill for 4 hours.

2.3.3 Calcination

After ball milling, calcination followed. It is a thermochemical reaction among the constituent oxides to form the desired solid solution. Another purpose is to reduce volume shrinkage in the final firing. [Jaffe 1971] Temperatures for calcination must be high enough for complete reaction, but low enough to avoid excessive lead loss, so 850 °C was selected to be the calcination temperature, since less lead would be lost at that temperature (<888 °C). After calcination, the colour of powder changed from orange to pale yellow. The calcination temperature profile is shown in Figure 2.8.

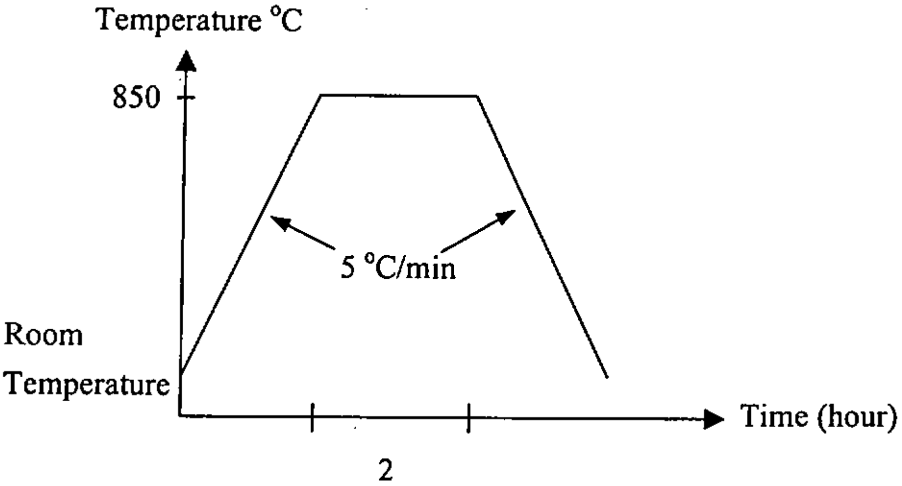

Figure 2.8 Calcination profile of the 0.9PMN-0.1PT powder.

After calcination, the 0.9PMN-0.1PT powder was ball-milled for an hour again to increase the uniformity. Since at high temperature, lead is very active such that powder in the upper part of the crucible would be Pb rich but the lower part would be Pb deficient.

2.4 Fabrication of 0.9PMN-0.1PT Ceramics

2.4.1 Dry Pressing

Unlike from the commercial PZT-552 powder, there is no binder included in the calcined 0.9PMN-0.1PT powder. Then binder should be added to the powder prior to further processing. The binder used was polyvinyl alcohol (PVA). For fabricating bulk ceramics, a concentration of 5 wt% PVA is enough. It was produced by mixing PVA and distilled water at a weight ratio of 5:95. PVA solution was added to the ceramic powder with a weight percentage of 5-10 % and was hand milled together such that the PVA solution could wet all ceramic particles uniformly. After mixing with PVA, the powder was placed in an oven so as to evaporate the water. The following step was dry pressing. The condition was the same as dry pressing a PZT-552 ceramic disc, which has been described in Section 2.2.1.

2.4.2 Binder Burnout

The 0.9PMN-0.1PT ceramic disc was put into a Lindberg / blue furnace for binder burnout. PVA can be burnt out at 550 °C by holding for one hour. Its burnout temperature profile is shown in Figure 2.9.

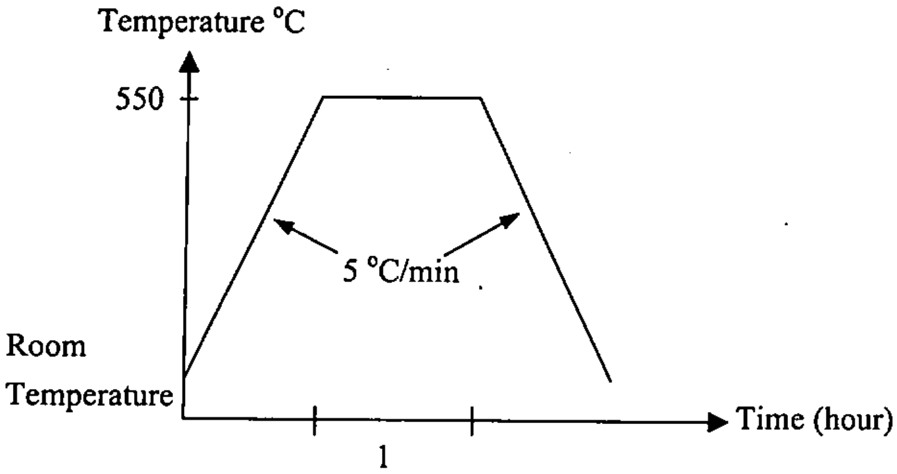

Figure 2.9 Binder burnout profile of the 0.9PMN-0.1PT ceramic.

2.4.3 Sintering

After the binder burnout, the 0.9PMN-0.1PT disc was sintered in the Carbolite RHF programmable furnace. Since lead will diffuse out of the sample during sintering and in turn degrade the ceramic performance, therefore, prevention should be taken to avoid lead loss. The best way is to bury the sample in 0.9PMN-0.1PT powder so that a lead rich atmosphere is provided to minimize lead loss.

Sintering temperature directly affects the ceramic grain growth, which consequently determines the ceramic performances. In this study, three sintering temperatures, 1150 °C, 1200 °C and 1250 °C were used so as to examine which sintering condition can give optimum properties of 0.9PMN-0.1PT for multilayer actuator fabrication. Figures 2.10 shows the sintering profile of 0.9PMN-0.1PT ceramic discs.

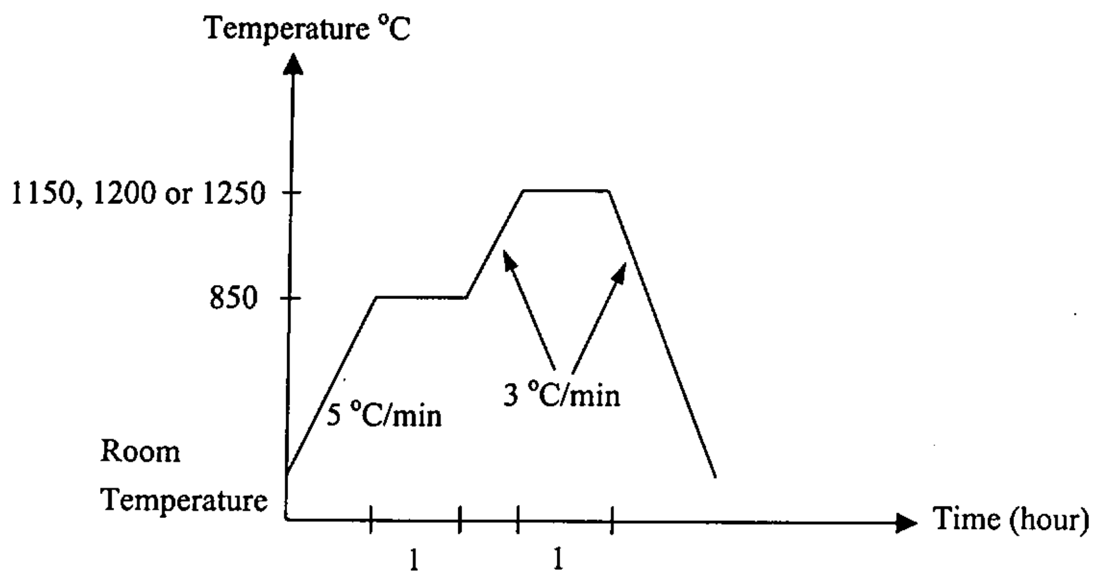

Figure 2.10 Sintering schedule of the 0.9PMN-0.1PT ceramic disc.

2.4.4 Polishing and Electroding

During sintering, the ceramic shrinks and its surface becomes rough. So polishing is essential to ensure its surface flatness. Wet and dry sandpaper of numbers 400, 800 and 1200 were used to polish the ceramic discs. After polishing, it was electroded by coating a chromium / gold layer onto its surfaces for subsequent measurements.

Chapter 3.

Characterizations of PZT and 0.9PMN-0.1PT Ceramics

3.1 Introduction

According to the method described in the previous Chapter, PZT and 0.9PMN-0.1PT ceramic discs were fabricated. PZT is a commercial grade material (PKI-552) with its specifications provided, hence, the measured material parameters can be compared to the prescribed data. 0.9PMN-0.1PT is self-made and its properties have to be optimized in order to select the most suitable fabricating conditions. Other than these two reasons, knowledge of the material properties is a key to design devices for the end applications.

In this Chapter, both types of ceramic samples were characterized by measuring the density using the Archimedes' principle, the hysteresis loops by the Sawyer Tower bridge [Sawyer 1930], and the elastic properties by the ultrasonic immersion method [Read 1978].

As PZT is a piezoelectric material poled in the thickness direction, so through measuring the planar and thickness resonance modes excited by applying a small ac signal, its electromechanical properties can be evaluated according to the IEEE Standards for Piezoelectricity [ANSI / IEEE Std. 1988]. For 0.9PMN-0.1PT, its single-phase purity was measured by X-ray diffraction [Kang 1988] and its grain size was observed through the scanning electron microscope. Permittivity and loss of the ceramic materials were obtained from the dielectric measurements [Villegas (A) 1999].

3.2 Density Measurements

Density of ceramics is an indicator of the quality of the materials. For 0.9PMN-0.1PT fabricated under different conditions, if the sintering temperature is too low, grains of the ceramics will not well grown, then the density will drop. If it is over sintered, excessive lead loss will also cause a drop in density.

In this part, ceramics densities were determined by the Archimedes' principle and by measuring the ceramics masses and dimensions. According to the Archimedes' principle, dry mass of the testing sample in air (m_{dry}) and mass of that sample suspended in water ($m_{suspended}$) were measured. Sample density can be found by the following equation:

$$\rho = \frac{m_{dry}}{m_{dry} - m_{suspended}} \rho_{water} \tag{3.1}$$

ρ is density of the sample and ρ_{water} is density of water which is assumed to be 1000 kg/m^3. By measuring the mass and dimensions, dry mass of the sample in air (m_{dry}) was measured together with its volume (vol). Hence, the sample density can be found by:

$$\rho = \frac{m_{dry}}{vol} \tag{3.2}$$

For a circular disc sample, its volume is the area times its thickness, so the density becomes:

$$\rho = \frac{m_{dry}}{\pi r^2 t} \tag{3.3}$$

where r is the radius and t is the thickness of the sample.

By the Archimedes' principle, density of PZT sample is about 7520 kg/m^3, while it is about 7580 kg/m^3 by measuring the ceramic mass and dimensions. Both values are close to the nominal density given by the PKI-552 specification list (7600 kg/m^3). For 0.9PMN-0.1PT ceramics, densities of the ceramics fabricated under different conditions are listed in Table 3.1.

Table 3.1 Average densities of 0.9PMN-0.1PT ceramics with different sintering temperatures and weight percent excess of lead oxide.

		Sintering temperature °C		
wt % excess of MgO	*wt % excess of PbO*	*1150*	*1200*	*1250*
1	*0*	**7050 kg/m^3**	**7756 kg/m^3**	**7872 kg/m^3**
1	*1*	**7100 kg/m^3**	**7850 kg/m^3**	**7934 kg/m^3**
1	*2*	**7343 kg/m^3**	**7731 kg/m^3**	**7650 kg/m^3**

According to the average densities listed in Table3.1, the maximum value is 7934 kg/m^3 for ceramic fabricated with 1 wt% excess of lead oxide and sintered at 1250 °C. Densities of the 0.9PMN-0.1PT ceramics with no excess of lead oxide and 1 wt% excess of lead oxide increase with sintering temperatures. It can be explained as the grain growth with increasing temperatures up to 1250 °C. After being sintered at 1250 °C, density of the ceramic with 1 wt% excess of lead oxide is greater than that of the sample with no lead oxide excess, because the excess lead oxide compensate for the Pb loss during sintering. Density of ceramic with 2 wt% excess of lead oxide is higher than that of the ceramics with other excess percentages under 1150 °C because over excess lead oxide reduced the optimum sintering temperature of the ceramic, further increase in sintering temperature results in poorer quality ceramics [Guha 1988].

3.3 Ferroelectric Hysteresis Measurements

For ferroelectric materials, ferroelectric hysteresis loop measurements is one of the most important characteristics. This hysteresis loop refers to the polarization (P) induced as a function of applied electric field (E). When electric field increases, polarization increases up to a certain point, but it would saturate when all domains are aligned. This is called the saturated polarization (P_s). But when the field reduces, some domains still remain aligned and polarization would not reduce to zero even when $E = 0$, this is called the remanent polarization (P_r). This P-E relationship forms a loop called the P-E loop. After passing through a critical field (coercive field, E_c), the polarization reduced to zero. Ferroelectric hysteresis loop can be observed by the use of a Sawyer-Tower bridge [Sawyer 1930]. This is actually measuring the dielectric displacement D, but it can be assumed that $P \cong D$ as the electric susceptibility χ<<1.

An ac signal of 10 Hz was applied to the test sample from a HP 8116A function generator, which was amplified by a Trek 609D-6 power amplifier. Figure 3.1 shows a schematic circuit of the Sawyer-Tower bridge for the observation of ferroelectric hysteresis loop. Data extracted from the oscilloscope was analyzed through a computer program, and a P-E loop was obtained.

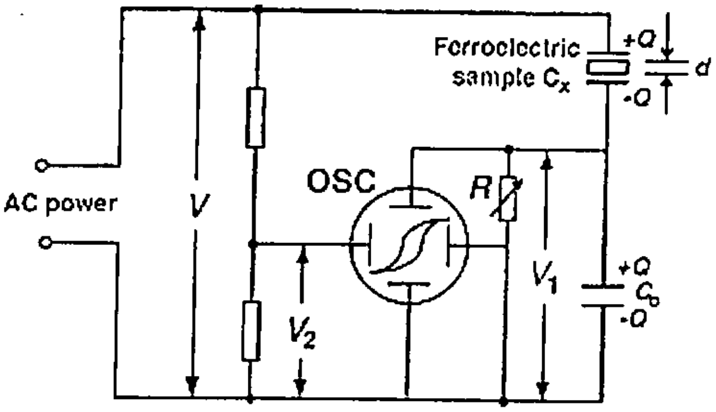

Figure 3.1 A schematic circuit of the Sawyer-Tower bridge for the observation of ferroelectric hysteresis loop.

Figure 3.2 shows a hysteresis loop of a 1 mm thick PZT sample. Coercive field of the PZT sample is found to be 1.1 kV/mm and its remanent polarization is 27 $\mu C/cm^2$. Polarization becomes saturate when the electric field approaches 2 kV/mm.

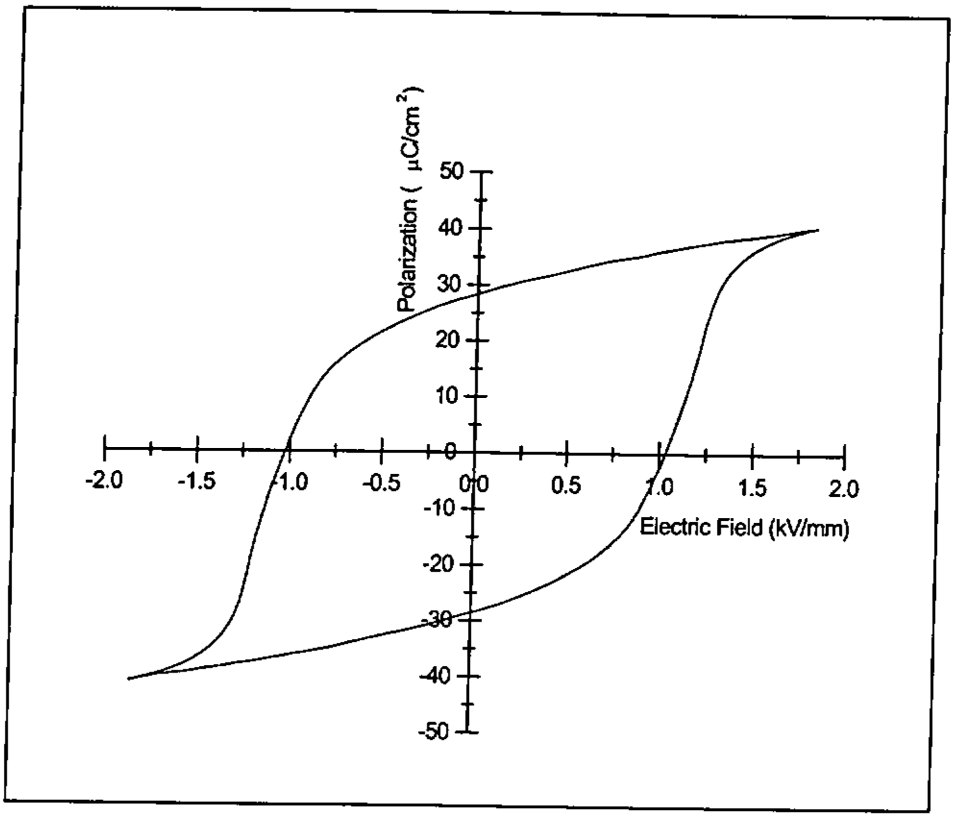

Figure 3.2 P-E loop of the PZT ceramic.

Figures 3.3-3.5 show the P-E loops measured at room temperature for the 0.9PMN-0.1PT ceramics of the three different compositions: with no lead oxide excess, 1 wt% excess of lead oxide and 2 wt% excess of lead oxide, respectively. As shown in Figures 3.3-3.5, in 0.9PMN-0.1PT, slim P-E loops are observed and weak remanent polarizations resulted showing that this relaxor ferroelectric material exhibits weak ferroelectricity and its polarization hysteresis is weak. Polarization becomes saturated when the electric field is increased up to 2 kV/mm.

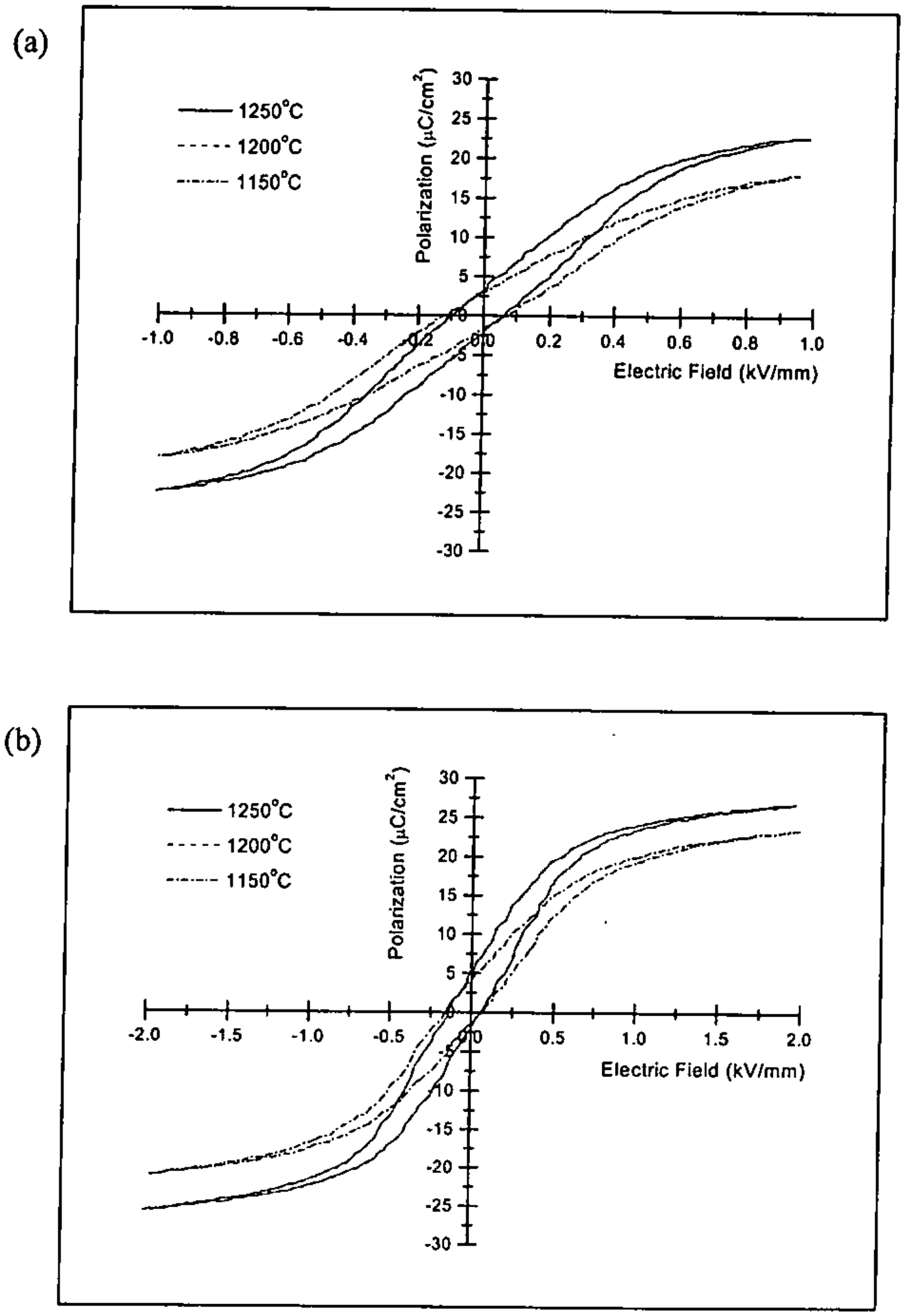

Figure 3.3 P-E loops of the 0.9PMN-0.1PT ceramic with 1 wt% excess of MgO but no excess of PbO measured at (a) 1 kV/mm, (b) 2 kV/mm.

(a)

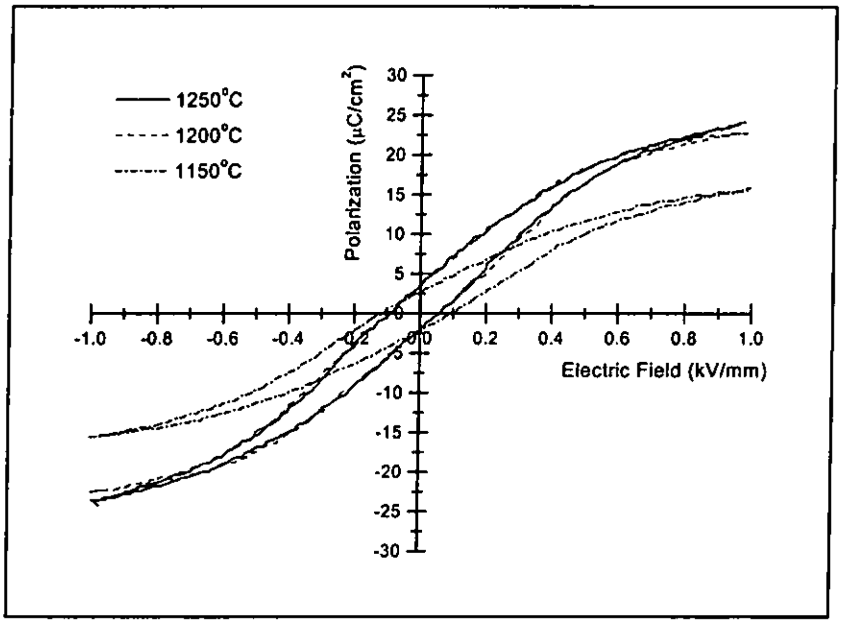

(b)

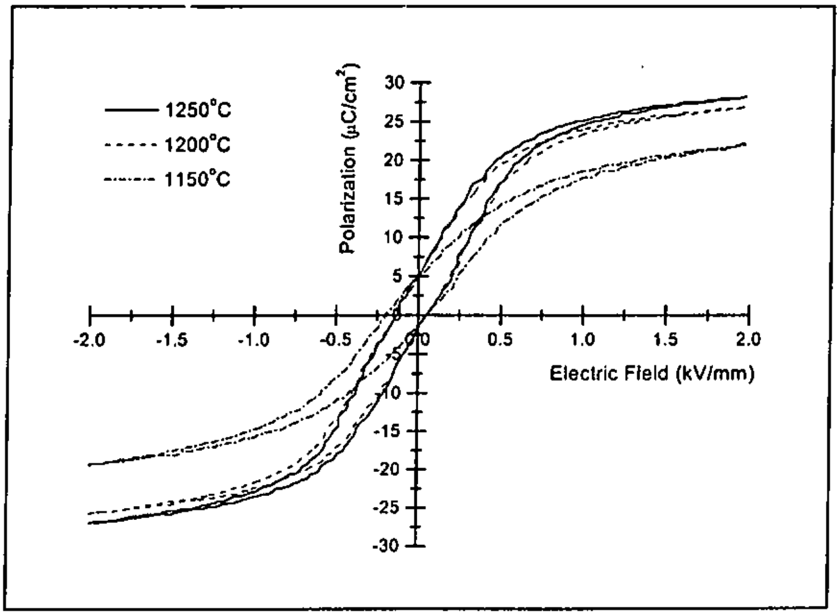

Figure 3.4 P-E loops of the 0.9PMN-0.1PT ceramic with 1 wt% excess of MgO and 1 wt% excess of PbO measured at (a) 1 kV/mm, (b) 2 kV/mm.

(a)

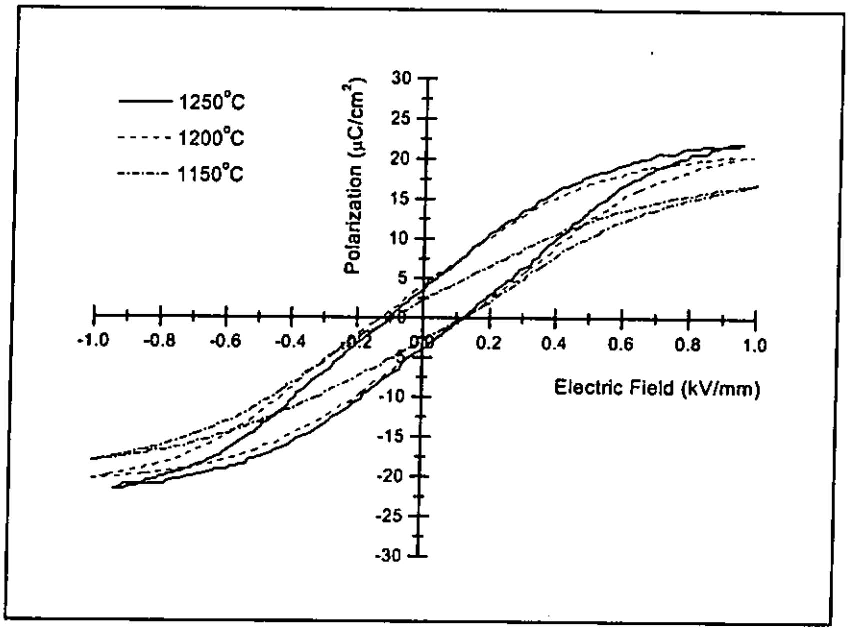

(b)

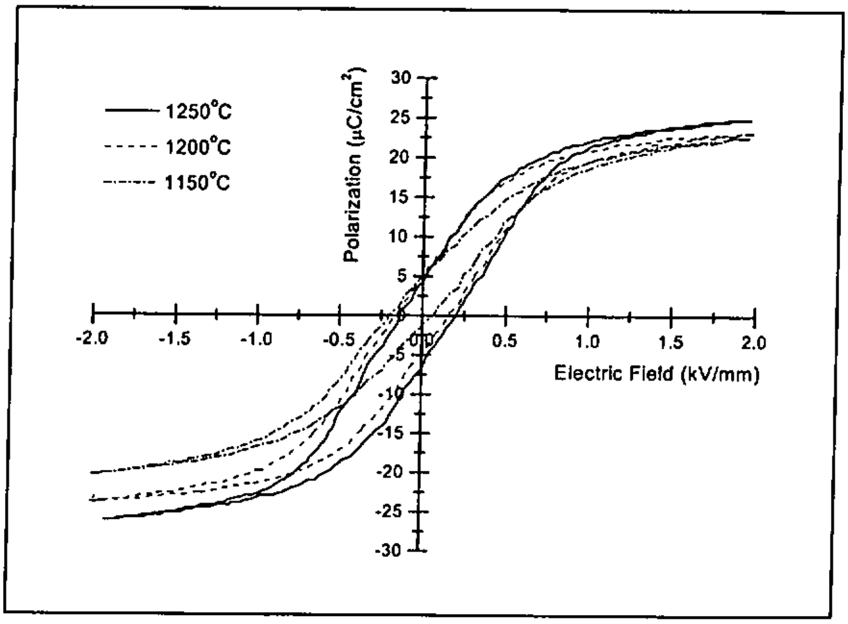

Figure 3.5 P-E loops of the 0.9PMN-0.1PT ceramic with 1 wt% excess of MgO and 2 wt% excess of PbO measured at (a) 1 kV/mm, (b) 2 kV/mm.

Coercive field of all the samples ranged from 0.08 to 0.12 kV/m as shown in Table 3.2. Saturated polarizations of the ceramics as listed in Table 3.2 are obtained from the maximum value of *P* under high field as shown in Figures 3.3 (b), 3.4 (b) and 3.5 (b). For all samples, the saturated polarization increases with the sintering temperature, but the value of the saturated polarization is roughly the same for the samples sintered at 1200 °C and 1250 °C. When comparing the saturated polarization P_s of the ceramics with different excess amount of lead oxide, it is found that P_s is maximum when 1 wt% excess of lead oxide was added. Ceramics of 2 wt% excess of lead oxide has the smallest value of saturated polarization, showing that the sample has poorer quality.

Table 3.2 Summary of the values of remanent polarization (P_r), saturated polarization (P_s) and coercive field (E_c) of the 0.9PMN-0.1PT ceramics with different fabricating conditions.

	Sintering temperature °C	P_r **($\mu C/cm^2$)**	P_s **($\mu C/cm^2$)**	E_c **(kV/mm)**
1 wt% excess MgO, 0 wt% excess PbO	*1150*	2.21	22.38	0.08
	1200	2.88	26.33	0.08
	1250	2.88	26.33	0.08
1 wt% excess MgO, 1 wt% excess PbO	*1150*	2.37	20.83	0.10
	1200	2.78	26.33	0.089
	1250	2.78	27.50	0.089
1 wt% excess MgO, 2 wt% excess PbO	*1150*	2.55	21.45	0.10
	1200	3.83	23.59	0.12
	1250	3.83	25.47	0.11

3.4 Elastic Properties Measurements

In a free isotropic material, both the longitudinal wave and transverse wave can be excited. In a longitudinal wave, the particles are vibrating along the wave propagation direction, while in a transverse wave; the particles are vibrating in a direction perpendicular to the wave propagation direction. Since wave velocities v in solid are related to the density ρ and elastic modulus C ($C = \rho v^2$), hence the elastic properties of the material can be found by measuring the wave velocities. The ultrasonic immersion method is used in this work [Or 2001].

Sample to be measured was placed in between two 10 MHz ultrasonic transducers (Figure 3.6). The sample was held by a stainless steel holder which can be adjusted at different height and set at different angles. Transducers and the sample were immersed in a bath of silicone oil. Waves propagates from one of the transducer would pass through the sample and received by another transducer. The Panametrics 5052 UA ultrasonic analyzer analyzed the time of wave propagation and the waveform was displayed in a HP 54645A digitizing oscilloscope. Figure 3.6 shows the schematic setup of the ultrasonic immersion method.

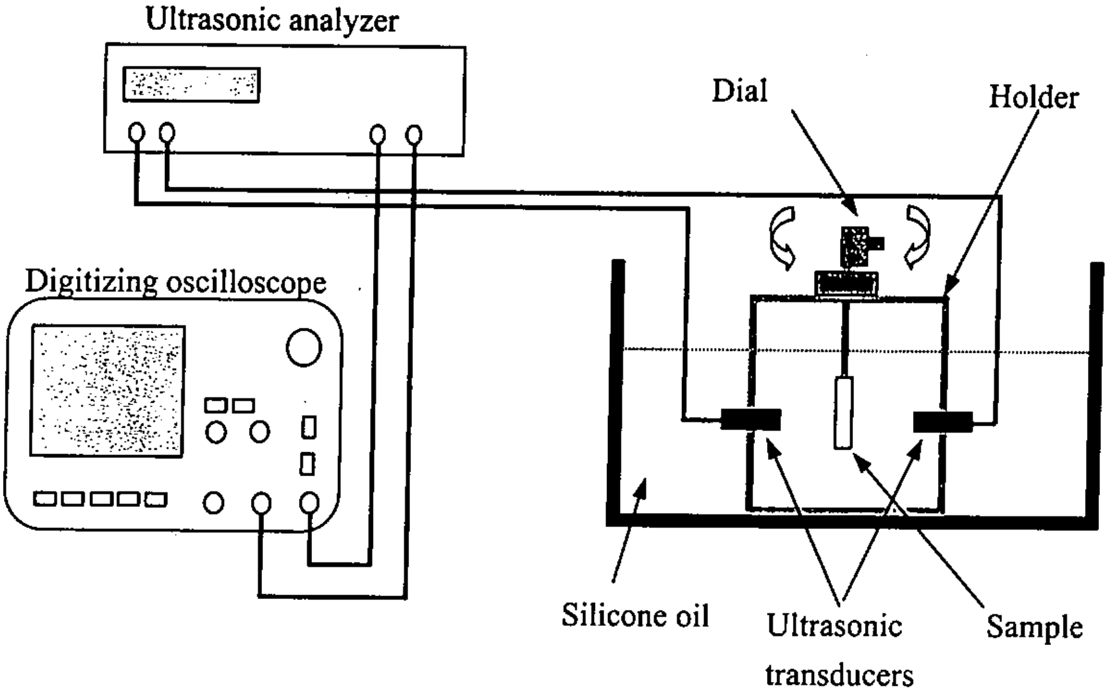

Figure 3.6 Schematic diagram of the ultrasonic immersion method.

3.4.1 Longitudinal Wave Velocity

The time required for the ultrasonic wave to travel from one transducer to another through oil is different before and after the sample has been inserted. This is because the sample replaces part of the oil and the wave velocities in oil and in the sample are different. If the sample is placed in a direction normal to the wave propagation, the longitudinal wave velocity v_l of sample can be calculated by [Choy 1998]:

$$\Delta T = t(\frac{1}{v_{oil}} - \frac{1}{v_l}) \qquad (3.4)$$

where ΔT is the time shift between wave propagation through oil before and after inserting the sample, v_{oil} is the acoustic wave velocity of oil and t is the thickness of the sample.

3.4.2 Shear Wave Velocity

As the acoustic wave velocity of oil is smaller than that of the sample, total internal reflection of the longitudinal wave in the sample occurs when it is rotated up to a critical angle θ_c, and for $\theta \geq \theta_c$, only shear waves can pass through the sample. According to this principle, the shear wave velocity of the sample can then be measured. By rotating the sample w. r. t. the direction normal to the wave propagation, the longitudinal wave in the sample becomes weaker as θ approaching θ_c and the shear wave becomes stronger and attaining a maximum when the longitudinal wave completely disappears. This shear wave signal travels slower than the longitudinal wave and takes longer time to reach the receiving transducers.

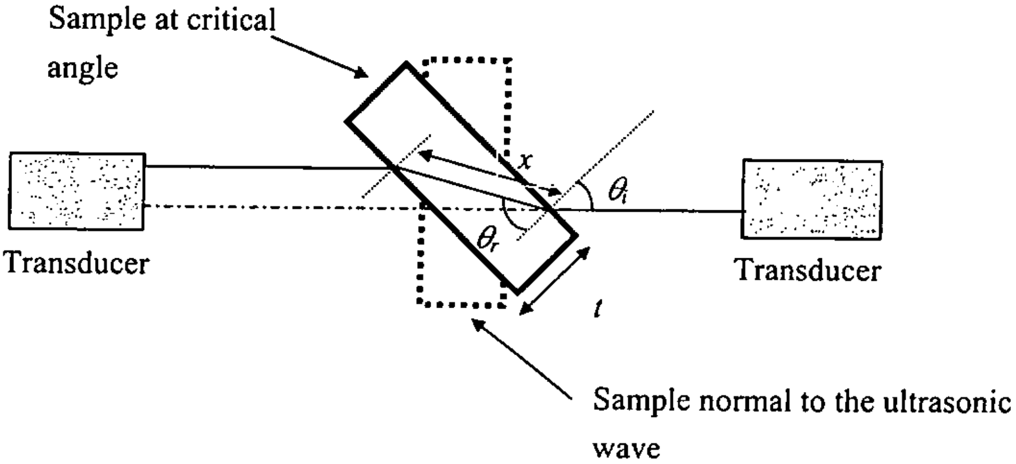

Figure 3.7 Schematic diagram of the shear wave propagation.

According to Snell's law, ratio of the acoustic velocity of oil and that of a material is related to the incident angle θ_i and to the refraction angle θ_r. It can be expressed as:

$$\frac{\sin\theta_i}{\sin\theta_r}=\frac{v_{oil}}{v_s} \tag{3.5}$$

θ_i is the angle between the directions of the longitudinal wave and the normal which can be found from the dial on the sample holder. The path length x through the sample can be expressed as [Choy 1998]:

$$x=\frac{t}{\sqrt{1-(\sin\theta_i\frac{v_s}{v_i})^2}} \tag{3.6}$$

Time shift ΔT_s between the wave propagation in oil and in solid measured from the oscilloscope can be expressed as:

$$\Delta T_s = x[\frac{1}{v_s}-\frac{\cos(\theta_r-\theta_i)}{v_{oil}}] \tag{3.7}$$

Shear wave velocity can be obtained by solving equation 3.7 together with equations 3.5 and 3.6. It can be expressed as:

$$v_s=\frac{v_{oil}}{\sin\theta_i}\sin[\arctan(\frac{t\sin\theta_i}{t\cos\theta_i+\Delta T_s v_{oil}})] \tag{3.8}$$

3.4.3 Elastic Stiffness Coefficients

By Hooke's law, stiffness coefficients c_{ij} is equal to ratio of the stress T_{ij} to strain S_{ij}. Where i and j denotes the direction 1, 2, 3, 4, 5 and 6.

$$c_{ij} = \frac{T_{ij}}{S_{ij}} \tag{3.9}$$

For an isotropic material, the stiffness matrix only contains nine coefficients, the matrix can be expressed as:

$$c_{ij} = \begin{pmatrix} c_{11} & c_{12} & c_{13} & 0 & 0 & 0 \\ c_{21} & c_{22} & c_{23} & 0 & 0 & 0 \\ c_{31} & c_{32} & c_{33} & 0 & 0 & 0 \\ 0 & 0 & 0 & c_{44} & 0 & 0 \\ 0 & 0 & 0 & 0 & c_{55} & 0 \\ 0 & 0 & 0 & 0 & 0 & c_{66} \end{pmatrix} \tag{3.10}$$

For a circular disc sample, $c_{11} = c_{22}$, $c_{44} = c_{55}$, $c_{13} = c_{23}$ and $c_{12} = c_{11} - 2c_{66}$. The longitudinal stiffness and shear stiffness can be expressed as [Hartmann 1980]:

Longitudinal stiffness: $$c_{11} = c_{22} = c_{33} = \rho v_l^2 \tag{3.11}$$

Shear stiffness: $$c_{44} = c_{55} = c_{66} = \rho v_s^2 \tag{3.12}$$

Cross-plane stiffness:

$$c_{12} = c_{21} = c_{13} = c_{31} = c_{23} = c_{32} = \rho(v_l^2 - 2v_s^2) = c_{11} - 2c_{44} \tag{3.13}$$

The whole elastic compliance matrix can be constructed by inverting the stiffness matrix [Hartmann 1980].

Longitudinal compliance: $$s_{11} = s_{22} = s_{33} = \frac{c_{11} + c_{12}}{(c_{11} - c_{12})(c_{11} + 2c_{12})} \tag{3.14}$$

Shear compliance: $$s_{44} = s_{55} = s_{66} = \frac{1}{c_{44}} \tag{3.15}$$

Cross-plane compliance:

$$s_{12} = s_{21} = s_{13} = s_{31} = s_{23} = s_{32} = \frac{-c_{12}}{(c_{11} - c_{12})(c_{11} + 2c_{12})} \tag{3.16}$$

The Poisson's ratio σ can be calculated as:

$$\sigma = -\frac{s_{12}}{s_{11}} \tag{3.17}$$

Table 3.3 summarizes the elastic properties measured at room temperature for unpoled PZT and 0.9PMN-0.1PT ceramics of different fabricating conditions. Results of the PZT are comparable to the short-circuit values (e.g. c^E_{33}, c^E_{11}, c^E_{31}, etc) given in the specifications from PKI.

For 0.9PMN-0.1PT, the elastic properties are dependent on the fabrication conditions. From Table 3.3, it is seen that properties of the 0.9PMN-0.1PT ceramics sintered at 1150 °C are quite different from that of the 0.9PMN-0.1PT ceramics sintered at 1200 °C and 1250 °C, it is presumably due to the lower density. When comparing the values of the shear modulus, longitudinal stiffness and shear stiffness of the 0.9PMN-0.1PT ceramics sintered at 1200 °C and 1250 °C with Leary's results [Leary 1999], similar values are observed. Leary's values of shear modulus; longitudinal stiffness and shear stiffness of the 0.9PMN-0.1PT ceramics are 37 GPa, 144 GPa and 27 GPa, respectively.

Table 3.3 Summary of the room temperature elastic properties of the PZT ceramic and 0.9PMN-0.1PT ceramics with different fabricating conditions.

	PZT	*(1 wt% MgO, 0 wt% PbO)*			*(1 wt% MgO, 1 wt% PbO)*			*(1 wt% MgO, 2 wt% PbO)*		
Elastic Properties	*1285°C*	*1150°C*	*1200°C*	*1250°C*	*1150°C*	*1200°C*	*1250°C*	*1150°C*	*1200°C*	*1250°C*
Density ρ *(kg/m^3)*	7500	7050	7756	7872	7150	7850	7934	7343	7731	7650
Longitudinal velocity v_l *(m/s)*	3400	3260	3800	3640	3160	3650	3750	3400	3750	3900
Shear velocity v_s *(m/s)*	1720	1860	2034	2050	1956	2065	2065	1987	2076	2250
$c_{11} = c_{22} = c_{33}$ *(GPa)*	86.6	74.8	112.0	102.0	80.7	105.0	112.0	84.9	109.0	116
$c_{44} = c_{55} = c_{66}$*(GPa)*	22.3	24.5	32.1	32.2	27.4	33.5	33.8	29	33.3	33.2
$c_{12} = c_{21} = c_{13} = c_{31} = c_{23} = c_{32}$ *(GPa)*	42.0	25.8	47.8	37.7	26	37.6	43.9	26.9	42.1	38.5
$s_{11} = s_{22} = s_{33}$ *(10^{-11}m^2/N)*	1.69	1.62	1.20	1.22	1.47	1.18	1.15	1.39	1.17	1.04
$s_{44} = s_{55} = s_{66}$ *(10^{-11}m^2/N)*	4.49	4.08	3.12	3.10	3.66	2.99	2.96	3.45	3.00	2.59
$s_{12} = s_{21} = s_{13} = s_{31} = s_{23} = s_{32}$ *(10^{-11}m^2/N)*	-0.55	-0.42	-0.36	-0.33	-0.36	-0.31	-0.33	-0.34	-0.33	-0.26
Poisson's ratio σ	0.32	0.26	0.3	0.27	0.25	0.27	0.28	0.24	0.28	0.25

3.5 Impedance Measurements and Piezoelectric Coefficients of PZT Ceramic

3.5.1 Impedance Measurements

It is important to know the impedance of a piezoelectric material in order to match the impedance between the driving circuit and the actuator [Stutts 1995]. Also, the impedance response with respect to the frequency of the ceramic disc can be used to estimate the electromechanical coupling coefficients, which shows how efficient the material can transform mechanical energy into electrical energy and vice versa. Dielectric permittivity can be calculated by measuring the capacitance of the disc at 1 kHz. The impedance/ phase vs. frequency curve was obtained by a computer controlled HP 4194A impedance/ gain phase analyzer.

The dielectric permittivity $K^T{}_{33}$ of a disc can be estimated by measuring the capacitance of a disc of known dimensions at 1 kHz,

$$K^T{}_{33} = \frac{Ct}{\varepsilon_0 \pi r^2} \tag{3.18}$$

where C is capacitance of the ceramic, t is thickness of the ceramic disc, r is its radius and ε_0 is the permittivity of free space.

When the poled PZT ceramic was subjected to an ac signal, vibrational modes would be excited. For a low loss ceramic, the frequency of minimum impedance is approximately equal to the resonant frequency f_r, while the anti-resonant frequency f_a is approximately equal to the frequency of maximum impedance. For a circular disc, two main vibrational modes are excited, the thickness mode (f_{rt}) and the radial mode (f_{rr}):

Thickness mode:

$$f_{rt} = \frac{1}{2t}\sqrt{\frac{1}{\rho s_{33}^E}} \tag{3.19}$$

Radial mode:

$$f_{rr} = \frac{1}{2d}\sqrt{\frac{1}{\rho s_{11}^E}} \tag{3.20}$$

where t and d are the thickness and diameter of the disc, respectively, ρ is the density of the ceramic, $s^E{}_{33}$ and $s^E{}_{11}$ are the elastic compliances of the ceramic material measured under a short circuit condition.

Electromechanical coupling factor is the square root of the ratio of the mechanical energy generated in response to electrical energy input or vice versa. The electromechanical coupling factors in the thickness and radial directions are denoted as k_t and k_p, respectively. They can be estimated by the following two equations [ANSI / IEEE Std. 1988], where t and r in the subscripts denote the thickness and radial modes, respectively.

$$k_t^2 = \frac{\pi f_r}{2f_a}\tan[\frac{\pi(f_a - f_r)}{2f_a}] \tag{3.21}$$

$$k_p^2 \approx \frac{(f_a^2 - f_r^2)}{f_r^2} \tag{3.22}$$

Mechanical Q (quality) factor is the ratio of the reactance to the resistance in the series equivalent circuit representing the piezoelectric actuator. Therefore, it can be determined by the equivalent circuit analysis function built in to the HP 4194A impedance/ gain phase analyzer. Moreover, it is also related to the sharpness of the resonance peak and the mechanical damping. Equivalent circuit of a piezoelectric device is a circuit combining *L*, *C* and *R* [ANSI / IEEE Std. 1988].

Figure 3.8 shows the equivalent circuit of a piezoelectric device. *L* is the inductance that corresponds to the stiffness of the device, the *C* in series with *L* and *R* is the capacitance that corresponds to the compliance, C_o in the parallel arm corresponds to the dielectric loss and R, the resistance, corresponds to the mechanical loss of the device.

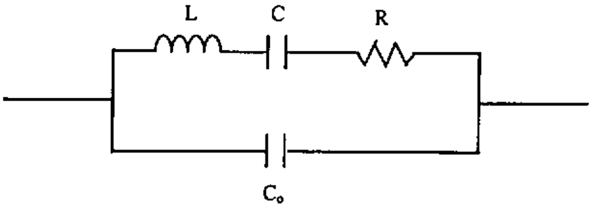

Figure 3.8 Equivalent circuit of a piezoelectric device.

Mechanical Q factor (Q_m) can be calculated by:

$$Q_m = \frac{\omega L}{R} \tag{3.23}$$

where ω is equal to the angular frequency, *L* and *R* were deduced from the equivalent circuit analysis.

Electrical Q factor (Q_E) is the inverse of the dissipation factor $D = \tan\delta$, where $\tan\delta$ can be measured at 1 kHz by the impedance analyzer.

$$Q_E = \frac{1}{\tan\delta} \tag{3.24}$$

3.5.2 Piezoelectric Coefficients

To determine the piezoelectric charge coefficients d_{33} and d_{31}, and the hydrostatic charge coefficient d_h, two experiments were conducted. The first one is to measure d_{33} directly by the d_{33} meter. The second one is to measure d_h by applying a hydrostatic force to the sample. Finally, d_{31} can be deduced from the measured d_{33} and d_h.

A ZJ-3D d_{33} meter by the Beijing Institute of Acoustics was used to measure the piezoelectric charge coefficient d_{33}. The ceramic sample was placed in between the two measuring probes in the meter, magnitude of d_{33} can be observed from the meter directly. The unit shown on the meter is pC/N. Figure 3.9 shows the schematic diagram of the d_{33} meter.

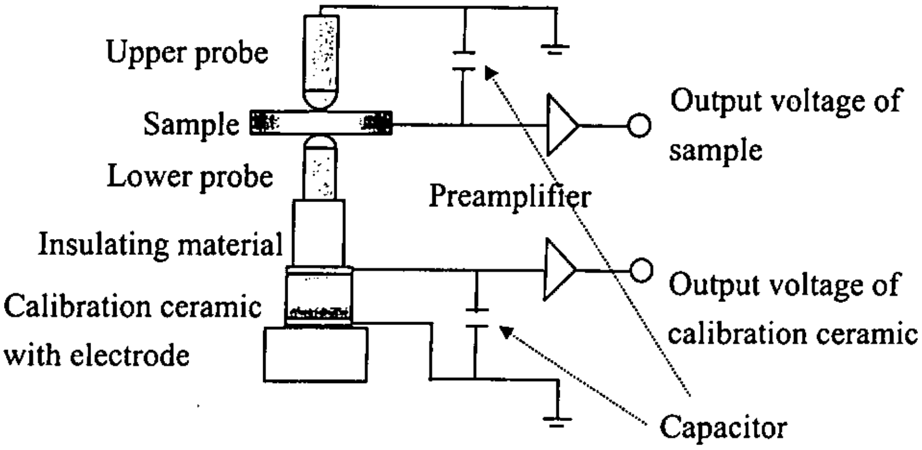

Figure 3.9 Schematic diagram of the d_{33} meter.

"d_h" is the hydrostatic charge coefficient which measures the charge generated when the sample is under stress equally applied in the 1, 2 and 3 directions. The sample electrode is perpendicular to the 3 axis. It can be measured through the use of the hydrostatic chamber made from PMMA [Ng 2001], and the acoustic pressure was applied to the PZT sample by two loudspeakers. Brass gauze was used to shield the sample in order to minimize the probability of electromagnetic coupling from the loudspeakers. Frequency of the driving source is about 25 Hz such that the loudspeakers can generate a hydrostatic force. Figure 3.10 shows the setup of the hydrostatic chamber for d_h measurement.

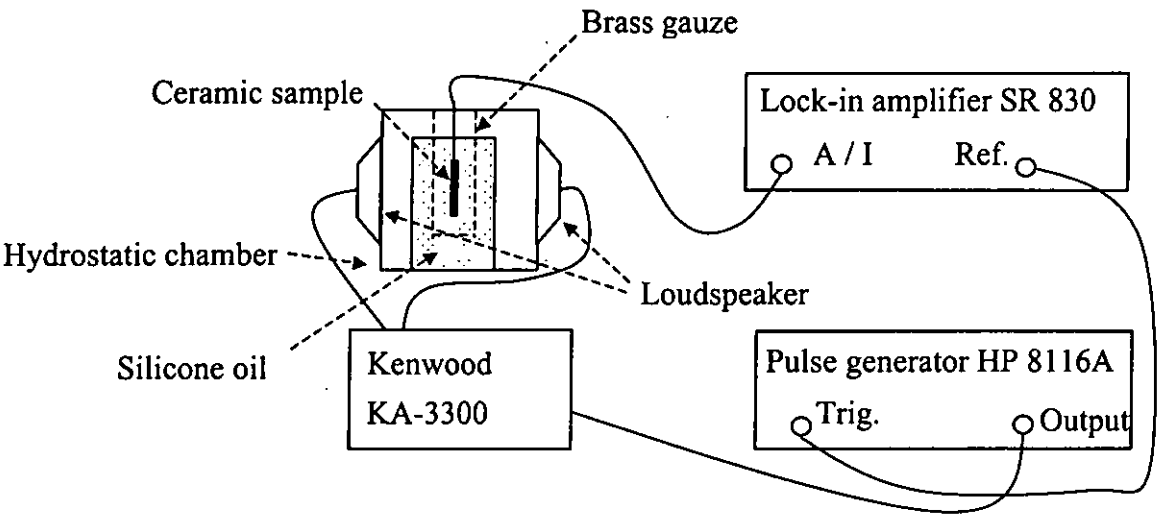

Figure 3.10 Setup of the d_h measurement.

Current output I_{rms} from the Stanford Research SR830 lock-in amplifier is related to d_h times the force applied F and the angular frequency ω. Where the applied force is equal to the pressure P generated by the speakers times the electroded area of the sample A. So, d_h can be expressed as:

$$d_h = \frac{\sqrt{2} I_{rms}}{A \omega P} \tag{3.25}$$

P can be measured by a calibrated hydrophone when the sample is placed in oil. Then d_{31} can be calculated from the equation,

$$d_h = d_{33} + d_{31} + d_{32} \tag{3.26}$$

For a circular disc, effects of piezoelectricity is the same in the 2 axis and 3 axis, so the equation for calculating d_{31} becomes:

$$d_h = d_{33} + 2d_{31} \tag{3.27}$$

where d_{31} is a negative value for PZT.

3.5.3 Results

Table 3.4 Summary of the experimental results for PZT material parameters and its piezoelectric charge coefficients.

	PZT	**Value from PKI-552 [Piezo Kinetics Inc. 2001]**
Dielectric Permittivity at 1kHz	3423	3400
Dissipation factor at 1kHz	0.018	0.022
Longitudinal Compliance, s^E_{33} $(10^{-12}m^2/N)$	19.8	20.2
Transverse Compliance, s^E_{11} $(10^{-12}m^2/N)$	14	15.9
Thickness coupling coefficient, k_t	0.55	0.75
Planer coupling coefficient, k_p	0.64	0.63
Mechanical Q factor (Q_m)	70	75
Electrical Q factor (Q_E)	55.56	45.45
Piezoelectric charge coefficient, d_{33} *(pC/N)*	590	593
Piezoelectric charge coefficient, d_{31} *(pC/N)*	-272.5	-274
Hydrostatic charge coefficient, d_h *(pC/N)*	45	45

3.6 X-ray Diffraction Patterns of 0.9PMN-0.1PT Ceramics

In preparing 0.9PMN-0.1PT ceramics, the most difficult problem is to fabricate powder with pure perovskite phase. It is because the presence of free niobium contributing to the formation of the parasitic pyrochlore phase. So, Swartz et. al. [Swartz 1982] improved the fabrication process by firstly prepare the columbite precursor. Some previous reports [Kang 1988, Swartz 1984] claimed that proper addition of excess magnesium oxide and lead oxide would contribute to the formation of perovskite phases. However, the purity of ceramics would also depend on the fabrication process. The aim of this section is to use X-ray diffraction (XRD) to determine the purity of the perovskite phase in ceramic powders under different fabrication conditions discussed in Section 2.3.2. X-Ray diffraction analysis was conducted with a Philips Analytical X-Ray Diffractometer and the PC-APD Diffraction software which is a line type scanning program. The sample was scanned from 20° to 70° in a step size of 0.02° with the X-ray (alpha1) wavelength of 1.54060Å. The crystal planes can be calculated by using the following equations:

$$2d\sin\theta = n\lambda \tag{3.28}$$

$$d = \frac{a}{\sqrt{(h^2+k^2+l^2)}} \tag{3.29}$$

where λ is the wavelength of the X-ray; d is the distance between each crystal planes; θ is the angle of reflection; h, k, l are the Miller Indices and a is crystal lattice constant. For a pure 0.9PMN-0.1PT polycrystalline ceramic, it is a simple cubic structure with a = b = c = 4.02 Å and the angle between the planes are all equal to 90°. The crystal planes that can be observed from 20° to 70° are listed in Table 3.5.

Table 3.5 The seven planes calculated for the perovskite phase of 0.9PMN-0.1PT ceramics.

h	k	l	$d(Å)$	2θ
1	0	0	4.01450	22.125
1	1	0	2.84350	31.435
1	1	1	2.32400	38.715
2	0	0	2.01480	44.955
2	1	0	1.80060	50.655
2	1	1	1.64540	55.830
2	2	0	1.42590	65.395

If pyrochlore phase exists, some peaks will be observed in the XRD pattern within 20° to 70° other than the 7 planes described in the Table 3.5 and it may reduce the purity of ceramic. Purity of the 0.9PMN-0.1PT ceramics can be expressed as the percentage of the relative amount of perovskite phase. It can be determined by measuring the main X-ray peak intensities for the perovskite (110) and the pyrochlore (222) phases, respectively. Equation 3.30 can be used to estimate the percentage of perovskite phase in the ceramics:

$$\textit{Percentage of perovskite phase} = \frac{I_{(110)}}{I_{(110)} + I_{(222)}} \times 100 \qquad (3.30)$$

where $I_{(110)}$ and $I_{(222)}$ are the peak intensities for the perovskite phase (110) and pyrochlore phase (222), respectively.

There are three compositions of the calcined 0.9PMN-0.1PT ceramic powder: (a) 1 wt% excess of MgO, (b) 1 wt% excess of MgO and 1 wt% excess of PbO and (c) 1 wt% excess of MgO and 2 wt% excess of PbO. Figure 3.11 shows the XRD patterns of the calcined powders of different compositions. It is seen that the purity of the 0.9PMN-0.1PT ceramic powder increases with the amount of PbO excess. Percentage of perovskite phase of the ceramic powder without any excess of PbO is about 92 %. For powders of 1 wt% excess PbO and 2 wt% excess of PbO, the percentage increases to 97 % and 100 %, respectively. It can be explained as the excess lead oxide lowering the calcination temperature and the excess MgO is responsible for suppressing the formation of the pyrochlore phase.

As discussed by Villegas [Villegas (B) 1999] and Wang [Wang 1990], an inhomogeneous phase distribution was observed near the surface. For an as-fired ceramic, most of the pyrochlore phases grown near the surface. It is enhanced by the PbO evaporation during sintering. Hence, a dense pyrochlore phase layer was formed on the ceramic surface, which would deteriorate its performance. For multilayer actuator fabrications, we cannot remove the pyrochlore phase layer by grinding or by other method. That is why it is important to control the purity of the ceramics. Ceramics of the three compositions described before were sintered at three temperatures: 1150 °C, 1200 °C and 1250 °C. So nine ceramic samples were prepared for XRD measurements.

Figure 3.12 shows the XRD pattern of the nine ceramics. When ceramics of no lead oxide excess were sintered at 1150 °C and 1200 °C, the perovskite phase ratios are 96 % and 97 %, respectively. When it was sintered at 1250 °C, the percentage of perovskite phase increases up to 100 %. Hence, there is no evidence to show that the pyrochlore phase formations at 1150 °C and 1200 °C are due to lead loss, and it may probably be due to the incomplete reaction at those temperatures.

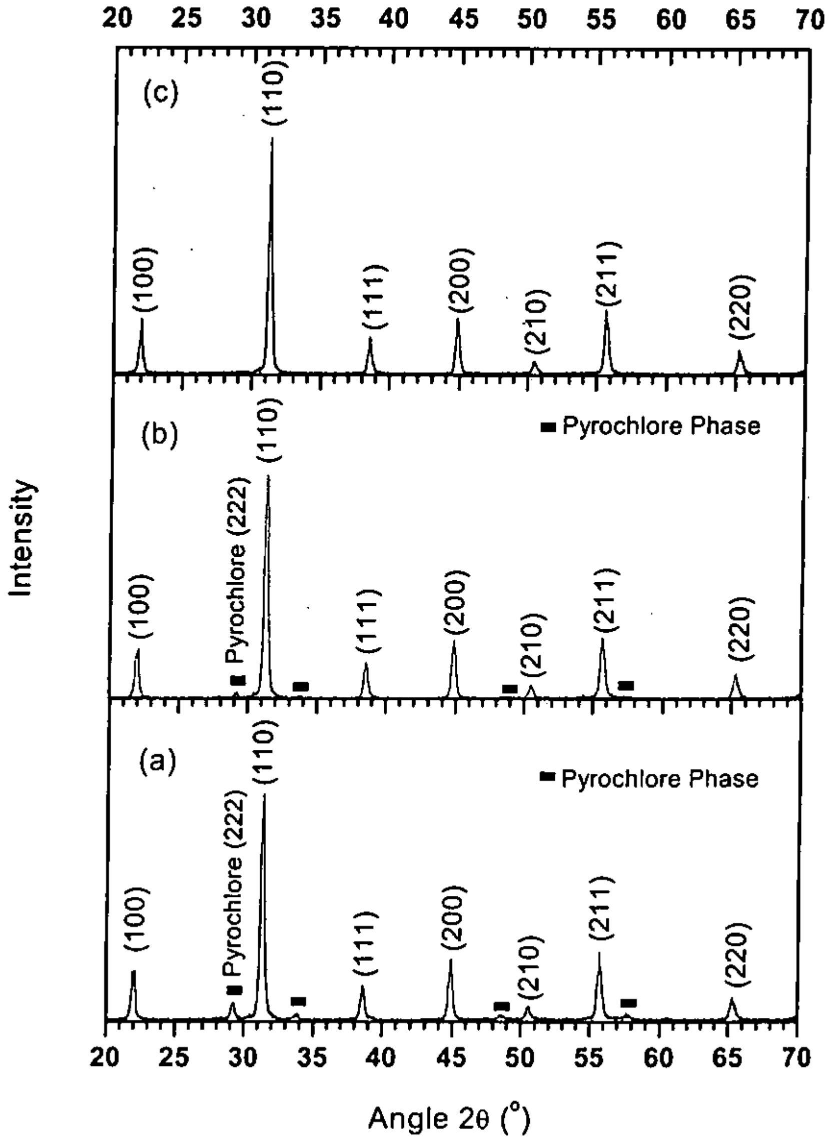

Figure 3.11 XRD pattern of the calcined 0.9PMN-0.1PT powder with 1 wt% excess of MgO and (a) no excess of PbO, (b) 1 wt% excess of PbO and (c) 2 wt% excess of PbO.

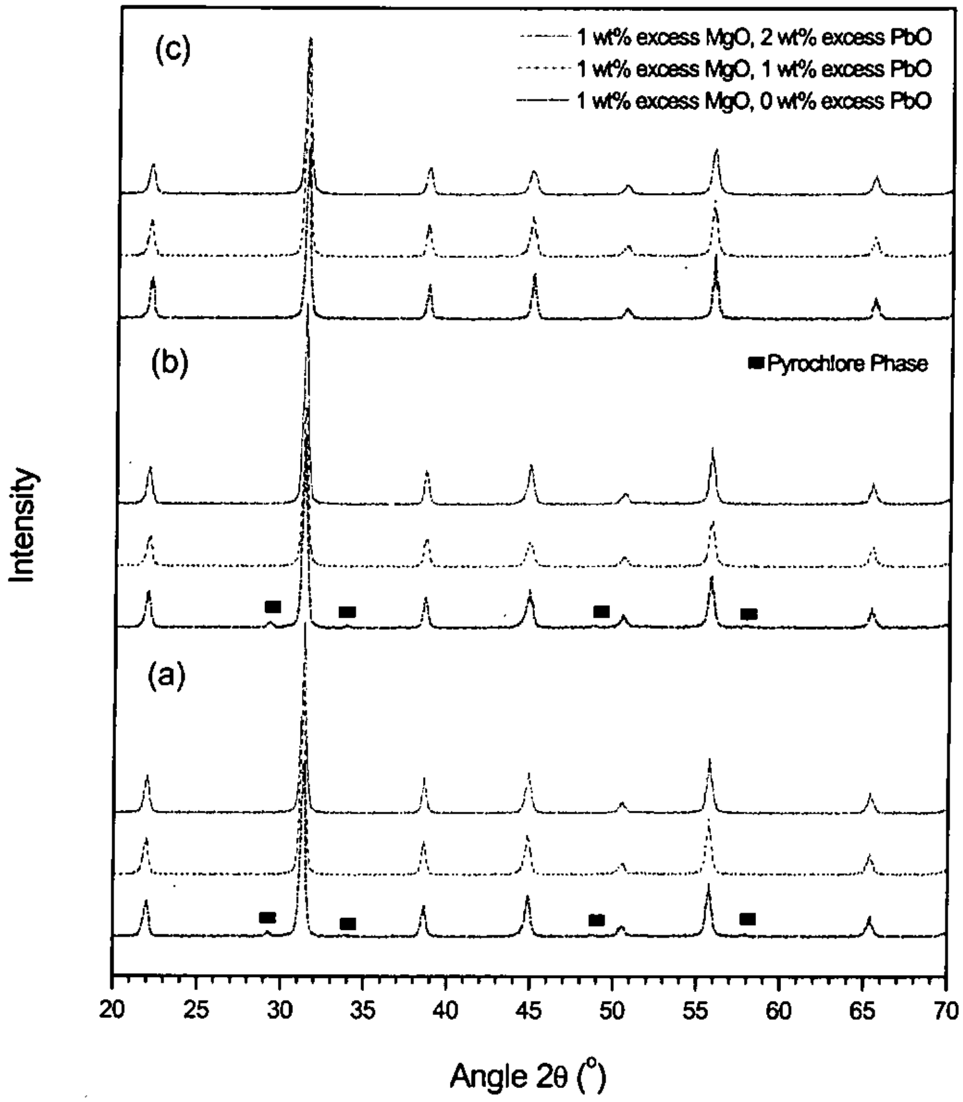

Figure 3.12 XRD patterns of the 0.9PMN-0.1PT ceramics with 1 wt% excess of MgO and three different excessive amounts of PbO sintered at (a) 1150 °C, (b) 1200 °C and (c) 1250 °C.

3.7 Scanning Electron Micrographs of 0.9PMN-0.1PT Ceramics

Scanning electron micrographs (SEM) of the 0.9PMN-0.1PT ceramics was obtained by a Leica Stereoscan 440 SEM. The fracture surfaces of the ceramics were observed with a layer of gold coating.

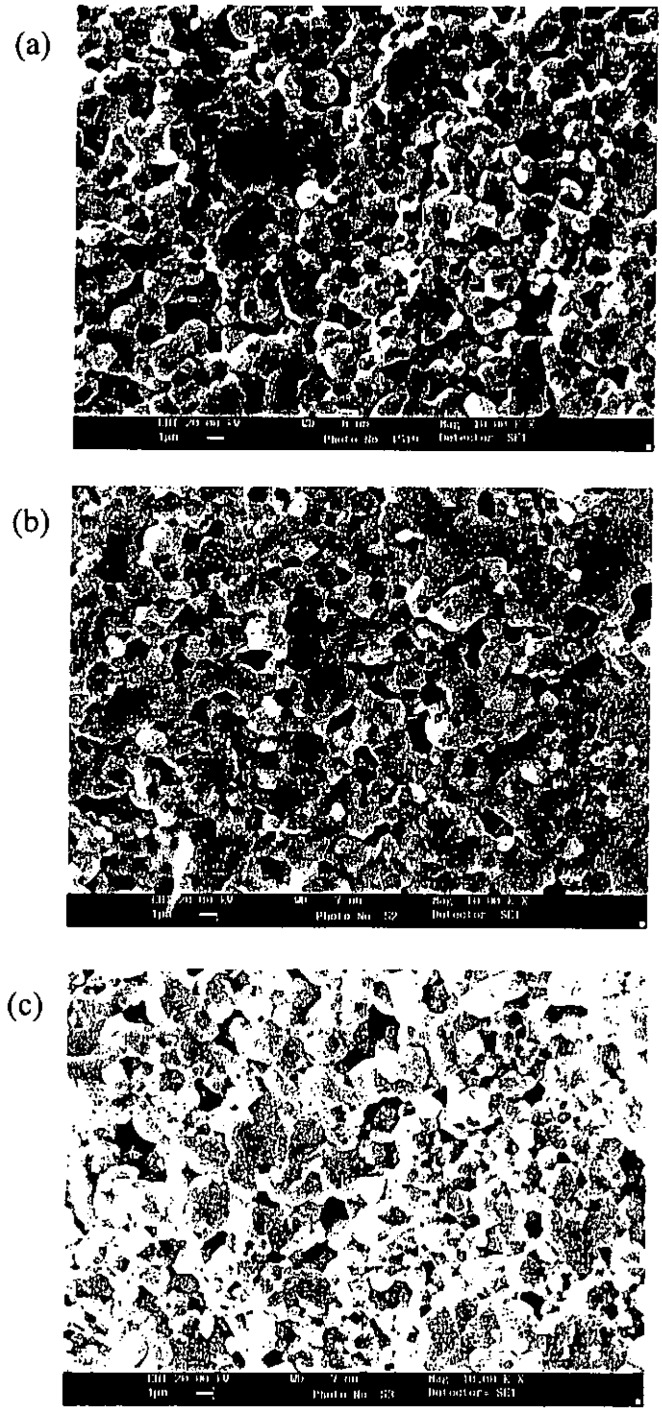

Figure 3.13 SEM micrographs of 0.9PMN-0.1PT ceramics (freshly fractured surfaces) sintered at 1150°C with 1 wt% excess of MgO and (a) no excess of PbO, (b) 1 wt% excess of PbO and (c) 2 wt% excess of PbO.

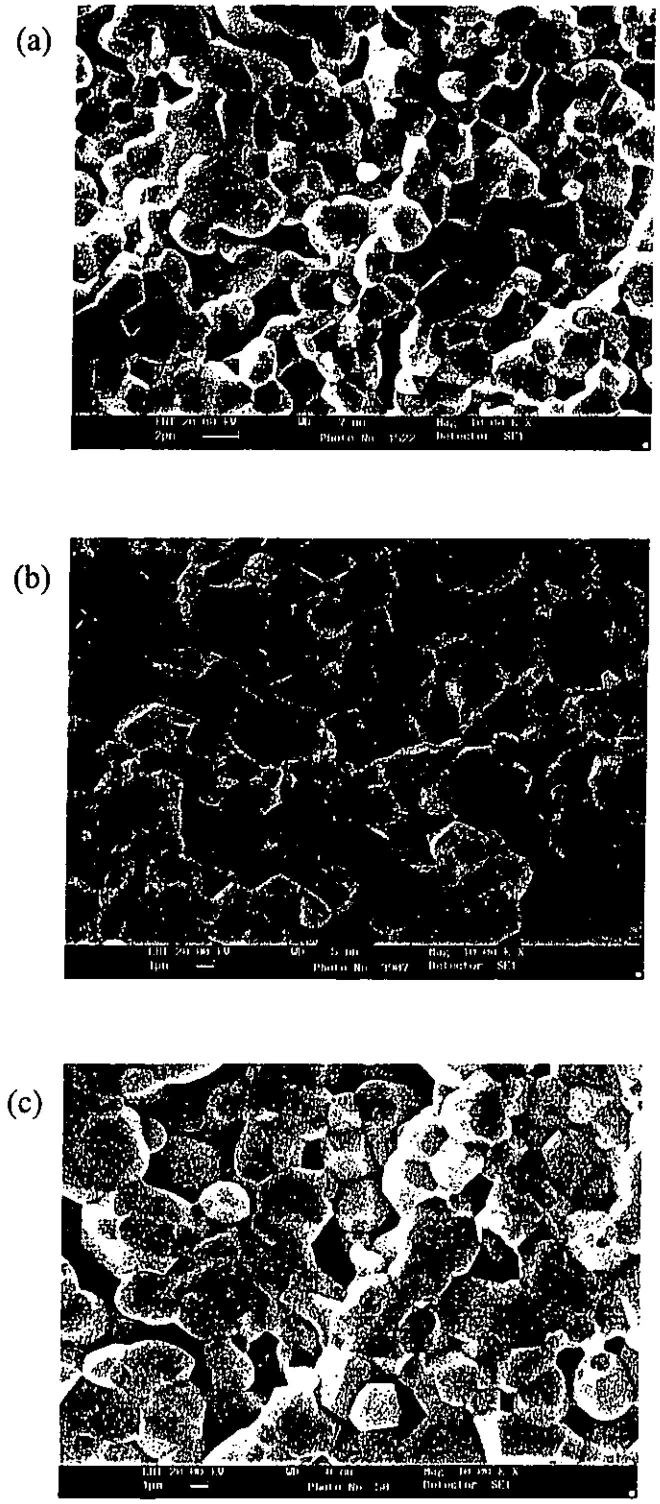

Figure 3.14 SEM micrographs of 0.9PMN-0.1PT ceramics (freshly fractured surfaces) sintered at 1200°C with 1 wt% excess of MgO and (a) no excess of PbO, (b) 1 wt% excess of PbO and (c) 2 wt% excess of PbO.

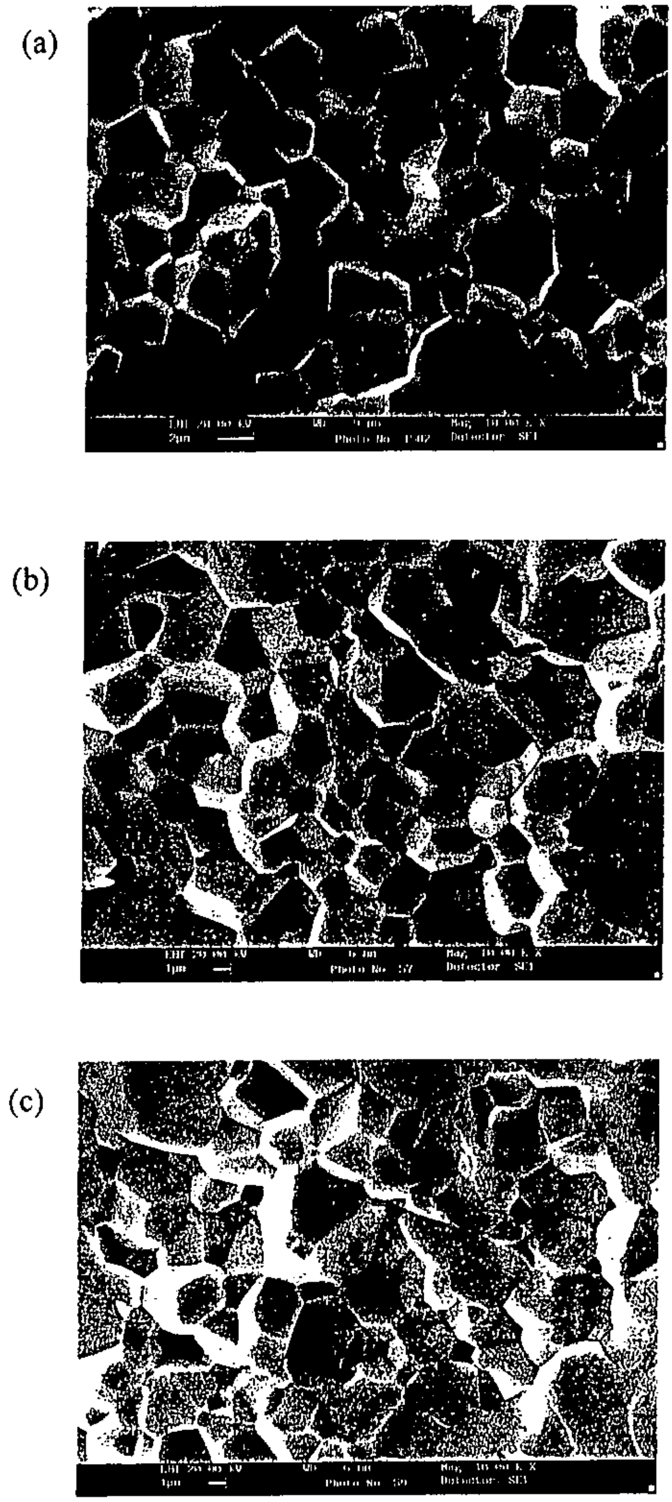

Figure 3.15 SEM micrographs of 0.9PMN-0.1PT ceramics (freshly fractured surfaces) sintered at 1250°C with 1 wt% excess of MgO and (a) no excess of PbO, (b) 1 wt% excess of PbO and (c) 2 wt% excess of PbO.

As shown in Figures 3.13-3.15, it is obvious that the grain size increases with sintering temperatures. For the ceramics sintered at 1150 °C, pores can be seen in the SEM micrographs in Figure 3.13, hence, low densities of ceramics are expected. The average grain sizes of the 3 different ceramics sintered at 1150 °C are 1.3 μm, 1.4 μm and 1.4 μm, respectively. The average grain sizes of the ceramics sintered at 1250 °C increased to 4.3 μm - 5.2 μm for the three compositions and less pores are observed.

3.8 Dielectric Measurements of 0.9PMN-0.1PT Ceramics

Consider the 0.9PMN-0.1PT ceramic disc as a parallel-plate capacitor of thickness t, its capacitance C can be expressed as its permittivity times the electrode area A divided by its thickness.

$$C = \frac{\varepsilon_o \varepsilon_r A}{t} \tag{3.31}$$

where ε_o is the permittivity of free space, ε_r is the dielectric permittivity. Since dielectric materials would absorb electrical energy if it is subjected to an alternating electric field, so dielectric loss exists and the dielectric permittivity would be in complex form,

$$\varepsilon_r = \varepsilon_r' - \varepsilon_r'' \tag{3.32}$$

where ε_r' is the real part of permittivity and ε_r'' is the imaginary part of the permittivity which is also called dielectric loss. The loss tangent (*tan* δ) can also represent the loss part as:

$$\tan\delta = \frac{\varepsilon_r''}{\varepsilon_r'} \qquad (3.33)$$

Dielectric permittivity of the 0.9PMN-0.1PT ceramics can be calculated by the sample capacitance through equation (3.31). A computer controlled HP 4194A impedance analyzer was used to measure the capacitance from 100 Hz to 1 MHz based on the principle of a Schering bridge [ASTM Std. 1999]. The sample was placed inside the ESPEC SU-240 oven such that its capacitance could be measured from –20 °C to 100 °C. Capacitance and loss tangent were saved to a computer file.

3.8.1 Results

Capacitance of the ceramics at different temperatures and frequencies were measured and the dielectric permittivities of the ceramics were calculated from equation (3.31). The calculated dielectric permittivities together with the loss tangents are plotted in Figures 3.16-3.18 as a function of temperature at different frequencies: 100 Hz, 1 kHz, 10 kHz, 100 kHz and 1 MHz.

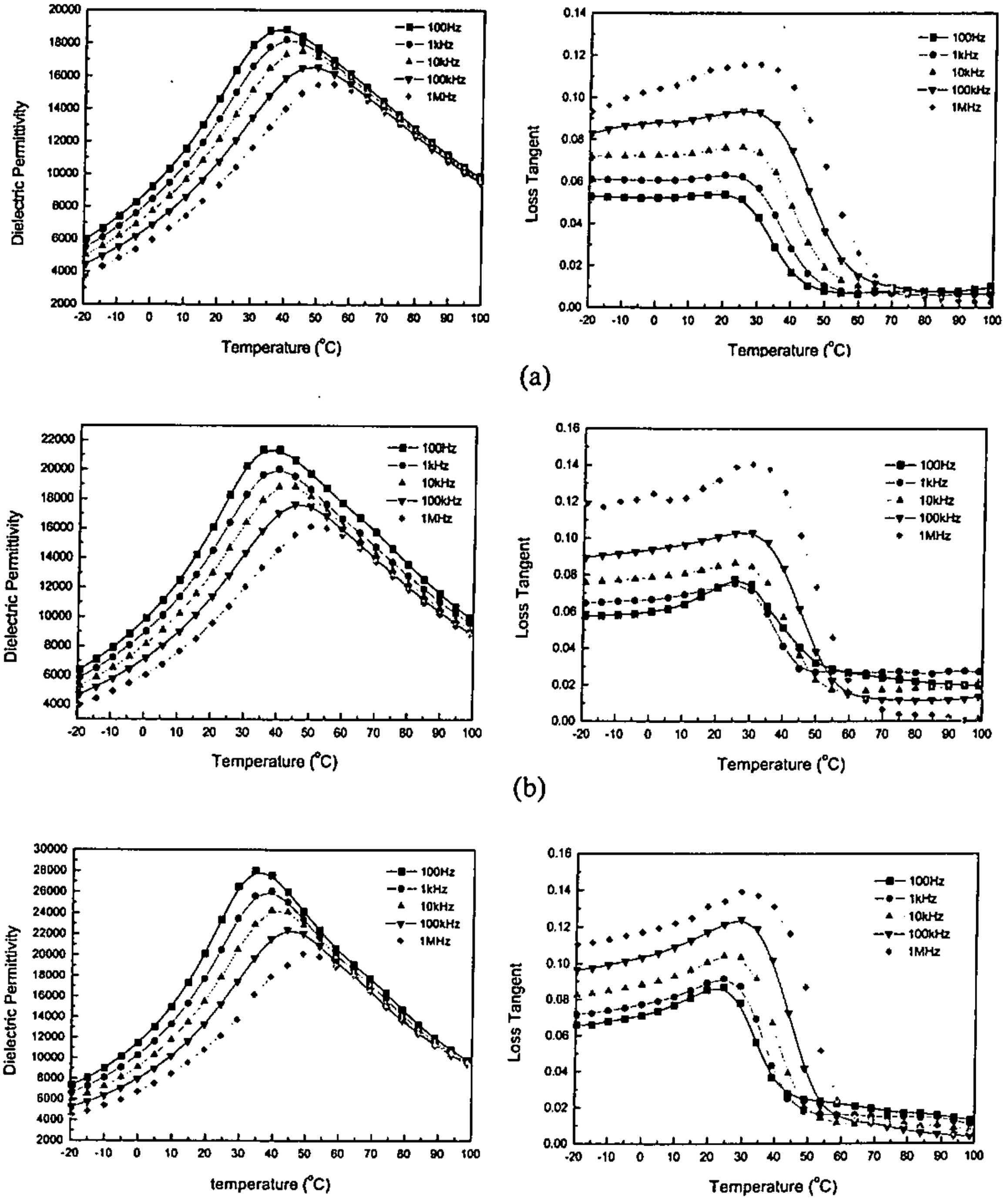
(a)

(b)

(c)

Figure 3.16 Dielectric permittivity and loss tangent versus temperature curves from 100 Hz to 1 MHz for the ceramics with 1 wt% excess of MgO but no excess of PbO sintered at (a) 1150 °C and (b) 1200 °C and (c) 1250 °C.

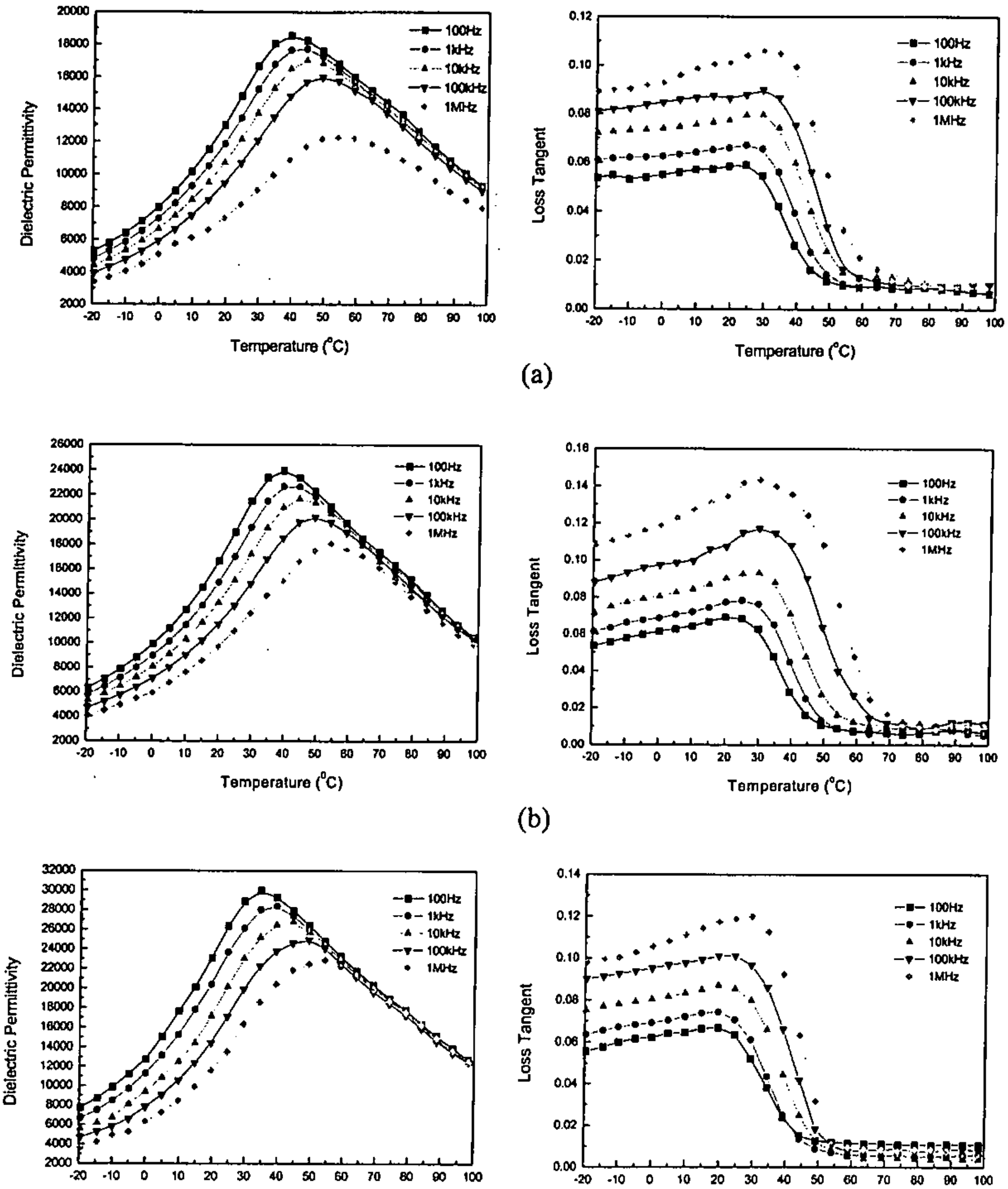

(a)

(b)

(c)

Figure 3.17 Dielectric permittivity and loss tangent versus temperature curves from 100 Hz to 1 MHz for the ceramics with 1 wt% excess of MgO and 1 wt% excess of PbO sintered at (a) 1150 °C and (b) 1200 °C and (c) 1250 °C.

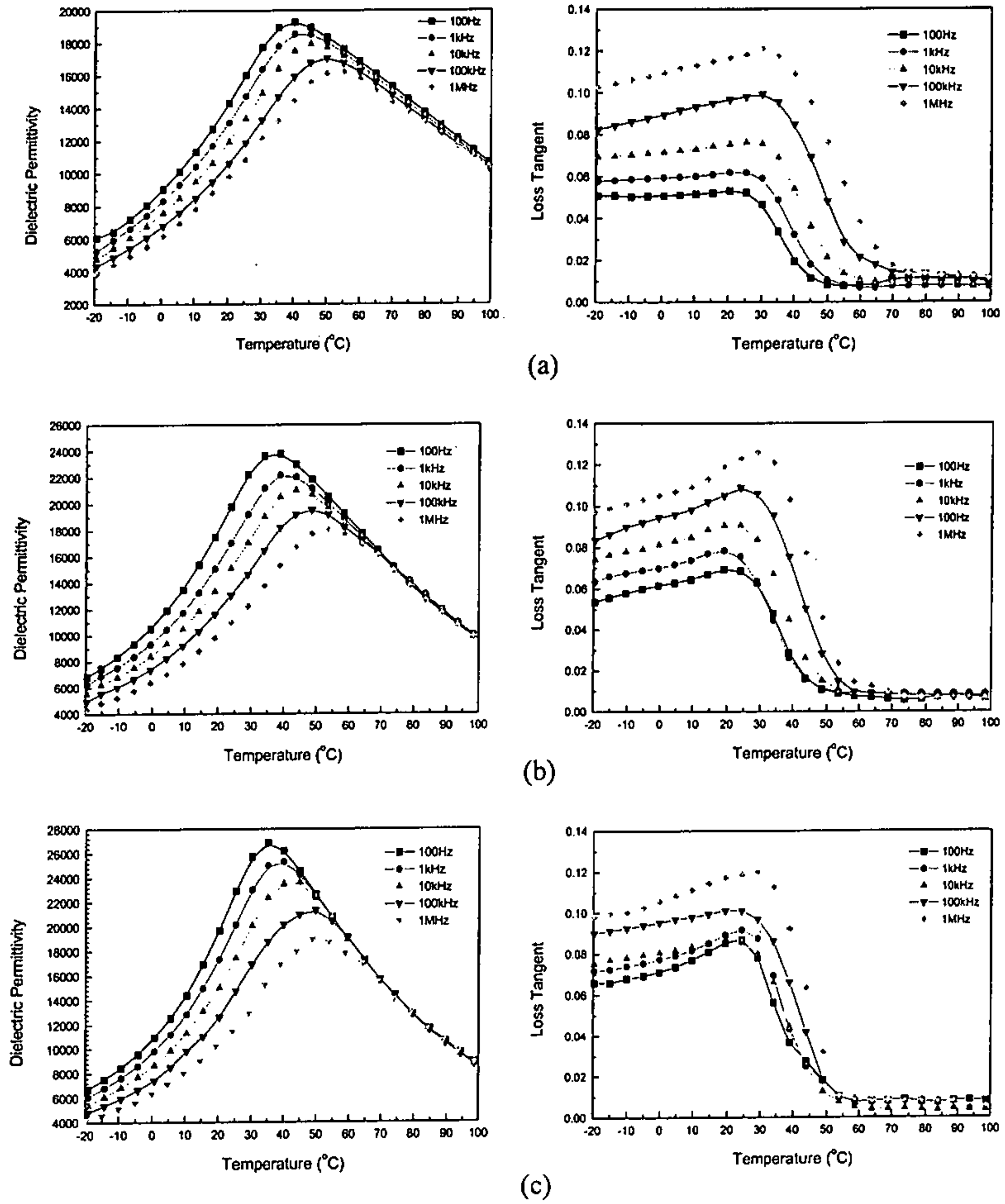

Figure 3.18 Dielectric permittivity and loss tangent versus temperature curves from 100 Hz to 1 MHz for the ceramics with 1 wt% excess of MgO and 2 wt% excess of PbO sintered at (a) 1150 °C and (b) 1200 °C and (c) 1250 °C.

3.8.2 Discussion

Results in Figures 3.16-3.18 show that 0.9PMN-0.1PT has very high maximum dielectric permittivity of up to 28500 at 1 kHz. The peak value of the dielectric maximum is at about 40 °C at 1 kHz. It is temperature dependent and had a broad-diffuse phase transition about the maximum dielectric permittivity (ε_m). Other than the temperature dependency, dielectric permittivity and loss tangent of the ceramics are also dependent on frequency. With increasing frequency, the maximum dielectric permittivity shifts toward higher temperature while the peak value of dielectric permittivity is decreased. However, for the ceramics of different weight percent excess PbO, the peak of dielectric permittivity is also at about 40 °C at 1 kHz, that means the excess PbO does not change the temperature of the maximum dielectric permittivity. Figure 3.19 shows the ε_m of the ceramics sintered at different temperatures as a function of the weight percent excess of PbO. It can be seen that ε_m increases with sintering temperature. This may be due to the fact that the ceramics sintered at lower temperature are more porous. When comparing ε_m of the ceramics sintered at 1250 °C of different weight percent excess PbO, the ceramic of 1 wt% excess MgO and 1 wt% excess PbO shows the highest value of ε_m (~28500). This means that further increase in the lead excess would not enhance the ceramic dielectric permittivity since excess PbO would be free in the sample and lowering the dielectric permittivity.

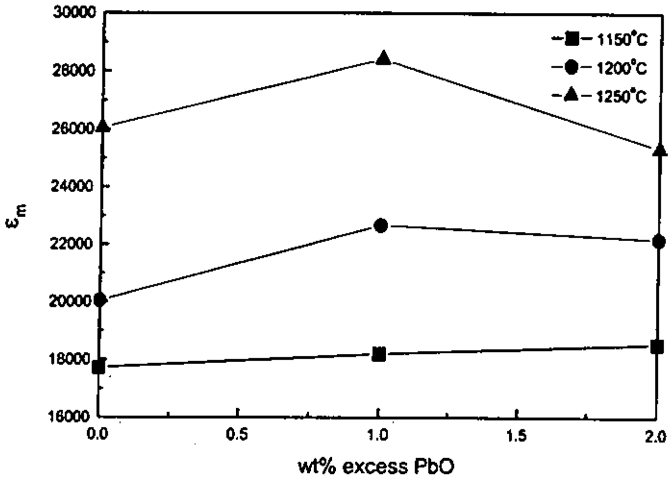

Figure 3.19 Maximum dielectric permittivity (at 1 kHz) of the ceramics sintered at 1150 °C (square), 1200 °C (circle) and 1250 °C (up triangle) as a function of weight percent excess of PbO.

Different level of excess PbO would not shift the maximum peak of the dielectric permittivity. For relaxor ferroelectrics, Smolenski and Rolov [Villegas (A) 1999] introduced the Gaussian distribution of the local Curie temperatures from which the diffusiveness of the transition, δ, for $T > T_m$ can be calculated from equation (3.34) [Villegas (A) 1999, Shrout 1987]:

$$\frac{\varepsilon_g}{\varepsilon_m} = \exp\frac{-(T-T_m)^2}{2\delta^2} \qquad (3.34)$$

where ε_m is the peak of the dielectric permittivity, T_m is the temperature of ε_m, ε_g is the intrinsic dielectric permittivity of PMN-PT perovskite grains at temperature T [Villegas (A) 1999], i.e.; ε. Since ε_g is temperature dependent, and this dependence can be calculated from the compositional fluctuation model of Kirillov and Isupov [Shrout 1987]:

$$\frac{1}{\varepsilon-\varepsilon_{high}} = \frac{1}{\varepsilon_m} + \frac{(T-T_m)^2}{2\varepsilon_m\delta^2} \qquad (3.35)$$

where ε_{high} is the high frequency dielectric permittivity. Assuming that $\varepsilon_g >> \varepsilon_{high}$, so that equation 3.35 becomes

$$\frac{1}{\varepsilon} = \frac{1}{\varepsilon_m} + \frac{(T - T_m)^2}{2\varepsilon_m \delta^2} \tag{3.36}$$

The plots of $1/\varepsilon$ versus $(T\text{-}T_m)^2$ in Figure 3.20 can be approximately assumed to be straight lines with similar slopes for the nine samples, where the slope of the curves represents the diffusiveness of the phase transition in the samples. Hence, very similar values of the diffusiveness parameter, δ, of the curves are resulted (23.9 K - 28.3 K). Therefore, the conclusion can be drawn that the PbO excess added to the 0.9PMN-0.1PT ceramics does not significantly modify the diffusiveness of the transition.

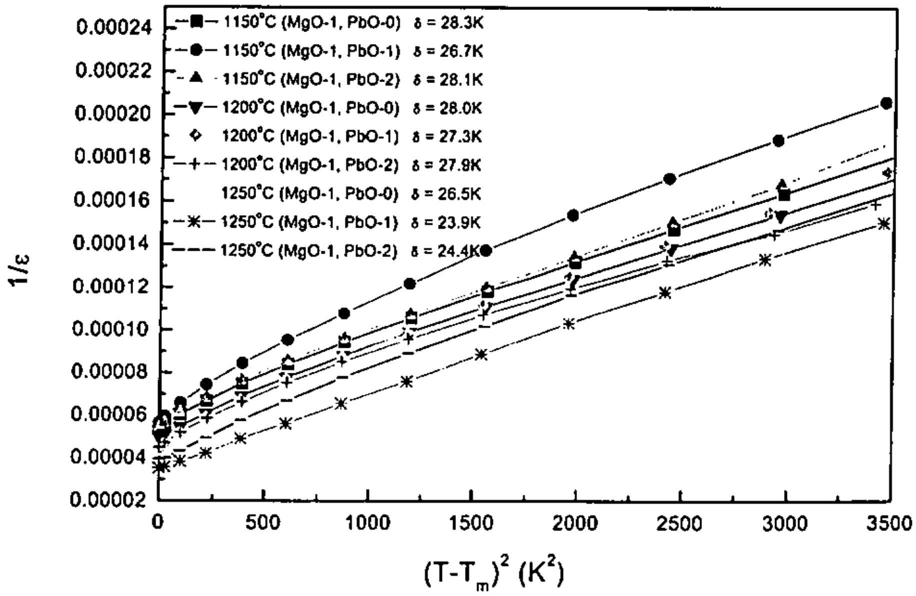

Figure 3.20 Reciprocal dielectric permittivity as a function of $(T\text{-}T_m)^2$ for the ceramics with different fabricating conditions.

3.9 Strain Measurements

The wireclamp application requires that the multilayer actuator can generate large displacement. Hence, the strain response of 0.9PMN-0.1PT ceramics is an essential criterion in selecting the most suitable fabricating conditions.

Strain responses of the 0.9PMN-0.1PT ceramics were measured by the DGS-6C1 inductance displacement sensor. This sensor is a linear voltage differential transformer (LVDT) which consists of three symmetrically spaced coils wound onto an insulated bobbin. A magnetic core, which moves through the bobbin without contact, provides a path for magnetic flux linkage between coils. When the sample displaced under a driving voltage, the core moved and induced an imbalance in mutual inductance between the primary and secondary coils and consequently developed an output voltage [Riley 1981]. A dc-biased electric field given by the HP 8116A function generator was amplified by the Trek 609D-6 high voltage amplifier and applied across the sample, while the sensor contacted the measured sample directly. Figure 3.21 shows the schematic diagram of the strain measurement.

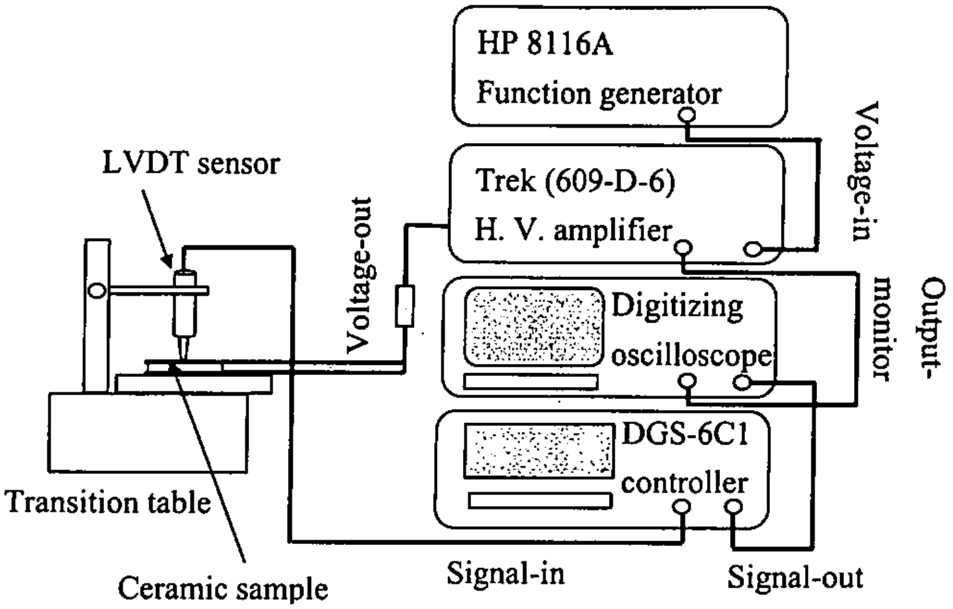

Figure 3.21 Schematic diagram of the strain measurement.

Due to the reason of measuring the strain of the ceramics in air, it is difficult to perform the experiment when applying high voltages to the ceramic samples. Hence, the maximum electric field applied on the sample is below 0.4 kV/mm. Although the applied field is not so high, it is enough to compare the strain responses of the nine samples.

Strain responses of the nine samples are compared in Figure 3.22, it is seen that the strain responses of the ceramics sintered at 1150 °C are the lowest irrespective of the composition, presumably due to high porosities. For the ceramics sintered at 1250 °C, the highest values of strain resulted except for the sample with 1 wt% excess of MgO and 2 wt% excess of PbO. Obviously, among all of the ceramic samples, the ceramic with 1 wt% excess of MgO and 1 wt% excess of PbO sintered at 1250 °C has the largest strain response of nearly 350×10^{-6} under 0.4 kV/mm.

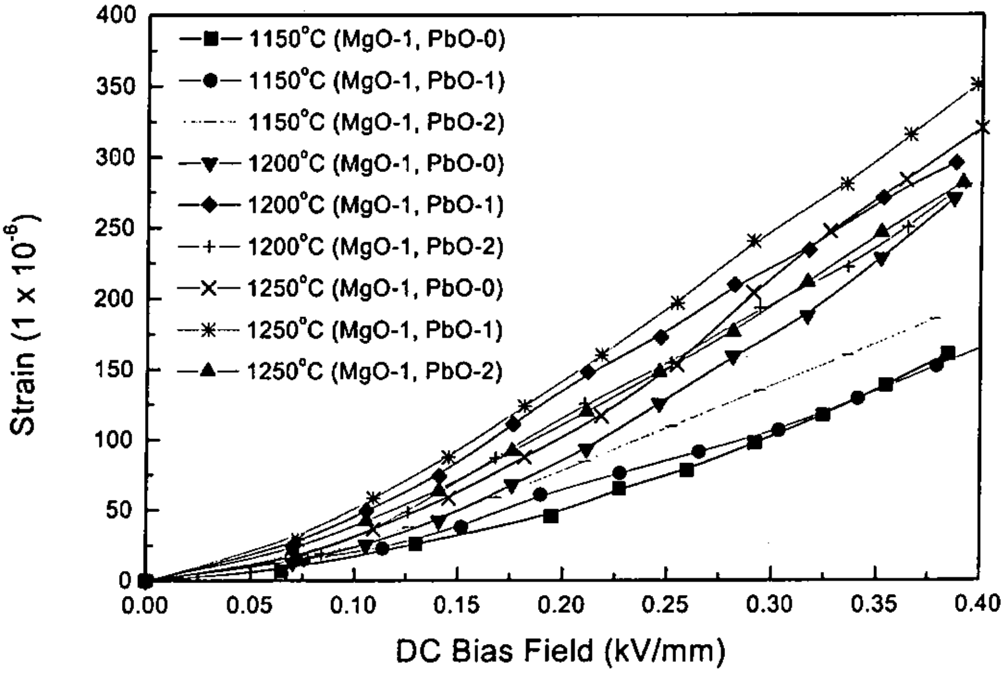

Figure 3.22 Strain responses of the 0.9PMN-0.1PT ceramics with different fabricating conditions.

3.10 Discussion

The experimentally determined material parameters of the PZT ceramics, including piezoelectric charge coefficient d_{33}; dielectric permittivity K^T_{33}, compliance coefficient s^E_{33} and electromechanical coupling factors etc, are all comparable to the values listed in the specifications provided by PKI. Hence, the fabrication condition discussed in Chapter 2 is suitable for the multilayer actuator fabrication process since it gives good properties.

For the 0.9PMN-0.1PT ceramics, the first criterion is to fabricate pure perovskite phase ceramics. As shown in the XRD pattern, this is successful for the ceramics with 1 wt% excess of MgO and 0-2 wt% excess of PbO with the sintering temperature above 1200 °C.

When comparing the results of the electrical polarization, maximum dielectric permittivity, and strain response of the 0.9PMN-0.1PT ceramics, it is obvious that the 0.9PMN-0.1PT ceramic with 1 wt% excess of MgO and 1 wt% excess of PbO, which was sintered at 1250 °C showed the best results. As a result, in the subsequent multilayer actuator fabrication, 0.9PMN-0.1PT ceramics with 1 wt% excess of MgO and 1 wt% excess of PbO is used with a sintering temperature of 1250 °C.

Chapter 4.

Fabrications of Multilayer Actuators

4.1 Introduction

Piezoelectric and electrostrictive multilayer actuators are widely used electronic devices because they have quick response time and high electromechanical coupling factors [Uchino 1997]. In this Chapter, the fabrication process of multilayer actuators is described. Two ceramic materials used for fabrications are PZT-552 (PKI Inc., USA) and 0.9PMN-0.1PT.

There are two methods for multilayer fabrication; one is by stacking up [Yao 2000] the fired ceramics and by connecting the layers electrically in parallel but mechanically in series. This method involves the use of glue or epoxy to affix the ceramics together and it is usually used for high power operations. Another method is by cofiring [Ritter 1992, Bridger 1996, Pilgrim 1994]. It is a technique developed from multilayer capacitor fabrications. [Takamizawa 1981] This technology has been applied on the fabrications of different devices like multilayer piezoelectric transformer [Tsuchiya 1985], piezoelectric transducer [Harrison 1986] and multilayer actuators [Moilanen 1993, 1994, Yao 1998]. The cofiring structure is composed of piezoelectric ceramic layers and internal electrode layers piled up alternately and the ceramic and electrodes are cofired at the same time. Since the thickness of each layer in the cofired ceramics is much smaller than that of a stacked ceramic so that the driving voltage can be reduced.

The fabrication process of multilayer actuators can be briefly described as slurry preparation, roll casting, electrode patterning, hot pressing, binder burnout sintering, external electrical connections and resin coating. For PZT multilayers, poling and short-circuit annealing is required before use. In order to fabricate a crack free actuator, extra precautions have to be taken in the binder burnout stage. Further discussions of this issue are given in Section 4.5. During sintering, the ceramic materials would shrink at such a high temperature, and delaminations may occur, so pressure has to be applied onto the ceramic multilayers in order to eliminate the delaminations.

4.2 Slurry Preparation and Roll Casting

Slurry refers to the mixture of the ceramic powder and the PVA binder solution. The first step is to prepare the material for roll casting. PZT and 0.9PMN-0.1PT ceramic powders were prepared as described in Chapter 2. The PVA binder solution was prepared by weighing PVA together with distilled water, ethanol and glycerin according to the ratio shown in Table 4.1. They were put into a covered beaker and placed into a MEMERT oven at 80 °C for one day. Then the cover of the beaker was removed and it was still kept at 80 °C until the weight of solution dropped to 85 % of its original.

Table 4.1 Weight percentage of the PVA solution when mixed.

	PVA	*Distilled Water*	*Ethanol*	*Glycerin*
Weight Percentage, wt%	18.52	74.07	1.85	5.56

Ceramic powder (PZT or 0.9PMN-0.1PT) and PVA solution were mixed in a weight ratio of 5:1 to form slurry. Trials have been carried out using weight ratios of 4:1 or 6:1. But the ratio 4:1 would cause cracks on the actuator during the binder burnout, since a high PVA ratio would produce large amount of carbon dioxide which evolves during chemical decomposition. For the ratio of 6:1, ceramic powder and PVA solution would not be mixed homogeneously because of insufficient binder. Furthermore, it is difficult to cut the green ceramic sheets after roll casting. As a result, 5:1 is the most suitable ratio.

Roll casting was carried out following slurry mixing. Roll casting and tape casting method can both be used to produce ceramic thick films. But for tape casting, slurry prepared must be uniform before casting, so a large amount of PVA solution will be needed. Under this circumstance, it is difficult to burn out the binder without creating cracks. Moreover, it is necessary to remove air bubbles before casting. These two requirements would make tape casting a much more complicated and difficult process for producing ceramic films. In roll casting, the slurry was put into the spaces between two rolls and a compressive force was applied. The rolling process can be repeated several times to enhance mixing and to eliminate air bubbles in the slurry.

As shown in Figure 4.1a, the slurry was put into the space between two rolls. When the distance between the two rolls decreased, the slurry would be compressed and stuck onto the two rolls (Figure 4.1b). This helped to enhance the mixing of the slurry. When the slurry became dry, a ceramic green sheet could be produced as shown in Figure 4.1c. Adjusting the distance between the two rolls could vary the thickness of ceramic sheets. Finally, several sheets of about 170 μm thick were fabricated.

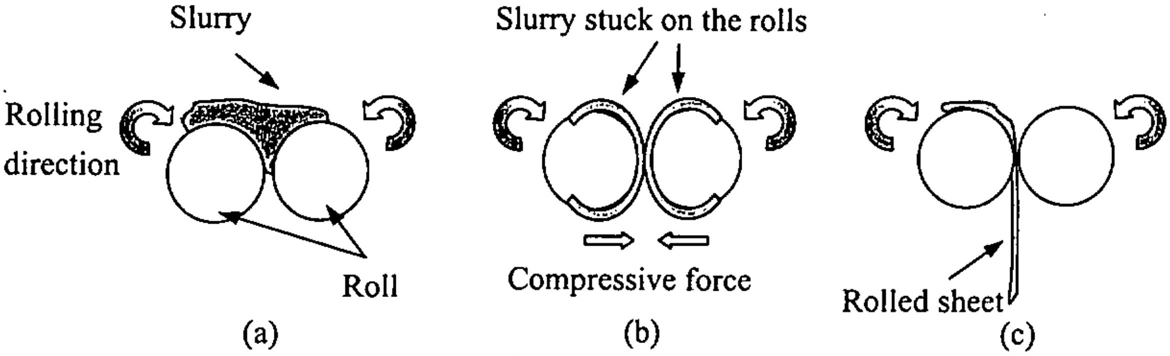

Figure 4.1 Roll-casting procedures. (a) Slurry was put in between the gap of two rolls. (b) Reducing the size of the gap, slurry would stick on the rolls so that binder and ceramic powders can be re-mixed again. (c) Ceramic sheet of desired thickness was formed by adjusting the separation between the rolls.

4.3 Cutting and Electrode Patterning

The ceramic green sheets were cut into a rectangular shape of 10 mm x 10 mm. Platinum (Pt) ink was used as the internal cofiring electrode since its melting point is over 1300 °C, which enable the ceramic to be fully sintered (1285 °C for PZT, 1250 °C for 0.9PMN-0.1PT). The Pt ink is a fine metal oxide powder mixed together with a temporary organic solvent. Figure 4.2 shows three possible different electrode patterns of a multilayer actuator. Figure 4.2 (a) shows the electrode pattern which is favorable for mass production. However, this kind of electrode would cause internal stress at the end of the internal electrode. As a result, displacement of the actuator would be reduced [Watanabe 1999]. Furthermore, cracks would be induced when subjecting to a high driving power [Aburatani 1995]. Figure 4.2 (b) shows the full electrode pattern which causes no internal stress in-between each layer, but it is difficult to connect the external electrodes. Pattern in Figure 4.2 (c) was used because the inactive part (no electrodes overlap) of each layer was minimized so that it can reduce the internal stress and it is easy to connect to external electrodes. In order to increase the viscous flow of the organic content of the ink, the painted film should be heated at 60 °C for an hour such that Pt powder can distribute evenly on the sheets. The green sheets were further heated to 90 °C for an hour so as to reduce the fluid content of the ink.

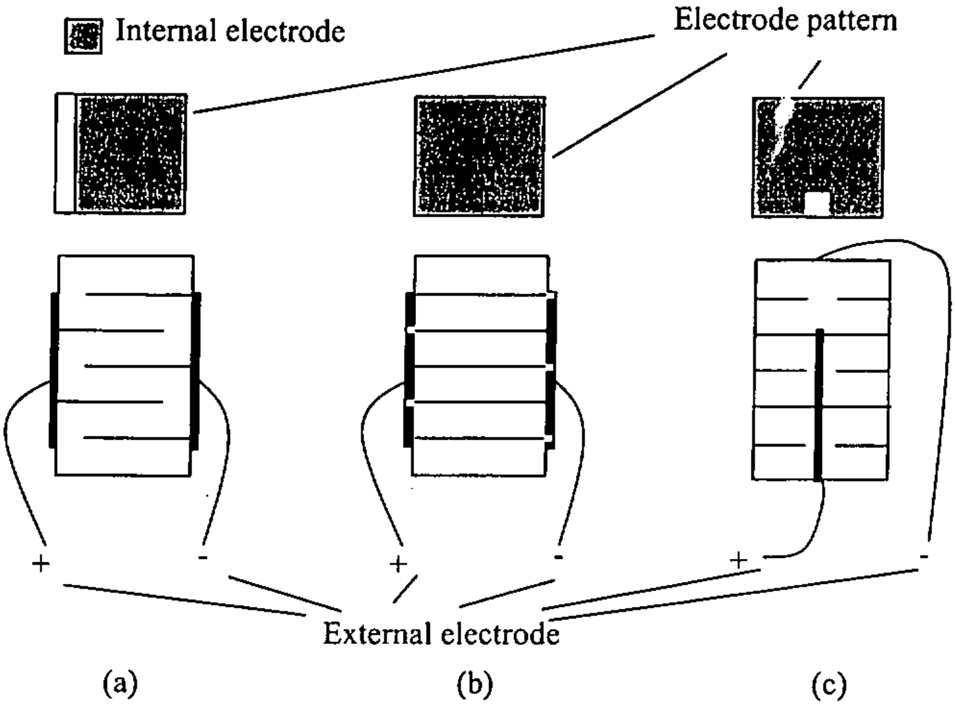

Figure 4.2 Multilayer actuators with (a) an interdigital pattern, (b) a full electrode pattern and (c) a tab electrode pattern.

4.4 Top and Bottom Inactive Layers

Other than the internal active layers (ceramic sheets with electrode), there are two inactive layers covering the top and bottom surfaces of the multilayer actuators. These inactive layers are made of similar ceramic materials to that of the active layers. The main functions of the inactive layers are protecting the internal active layers and acting as an insulating layer such that the top and bottom surfaces of the actuator can be connected together without short-circuiting. Each inactive layer consists of two ceramic sheets which are of the same thickness as the active layers. They are placed on the top and bottom of the stack of the active layers before hot pressing.

4.5 Hot Pressing

In order to form a multilayer ceramic stack; it is necessary to provide a mechanical force to bond all layers together. For using dry pressing method, water would remain inside the PVA and would cause cracks during binder burnout. Therefore, using a hot pressing method may be more suitable for multilayer processing. After painting the electrode with the desired pattern, the ceramic sheets were stacked alternately and placed inside a mould. It was subjected to a uniaxial stress of 200 MPa at room temperature. Temperatures of the hot platens were raised to 150 °C to reduce the water content of the ceramic sample. The sample was pressed for 2 hours under the same pressure and temperature. Under such a high pressure, porosity of the sheets would decrease and the metallic electrode can diffuse into the sheets through the pinholes which will enhance bonding of each ceramic sheet. Figure 4.3 shows the schematic diagram of the pressing mould, the screws were used for locking the two parts of the mould.

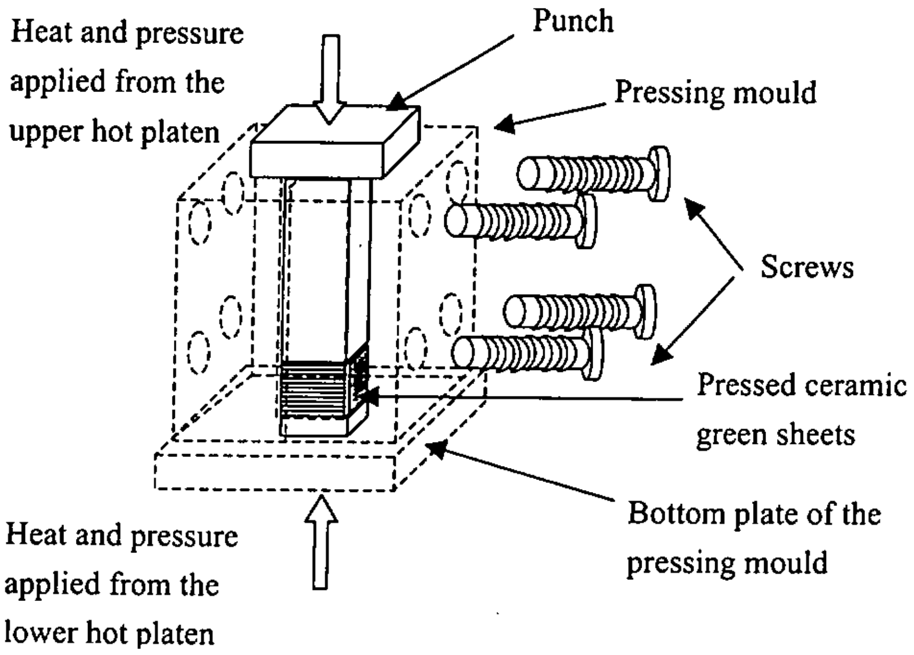

Figure 4.3 Schematic diagram of the hot-pressing mould.

4.6 The Binder Burnout Process

Before sintering, organics from the binder or from the Pt ink must be burnt out from the multilayer actuators. During the binder burnout process, binder decomposed and expelled from the sample. If the temperature rises rapidly, the organics would leave the sample in a very rapid rate and this would ruin the sample. Figure 4.4 shows three common observable defects in the sample when organic vapour was generated rapidly during the burnout process.

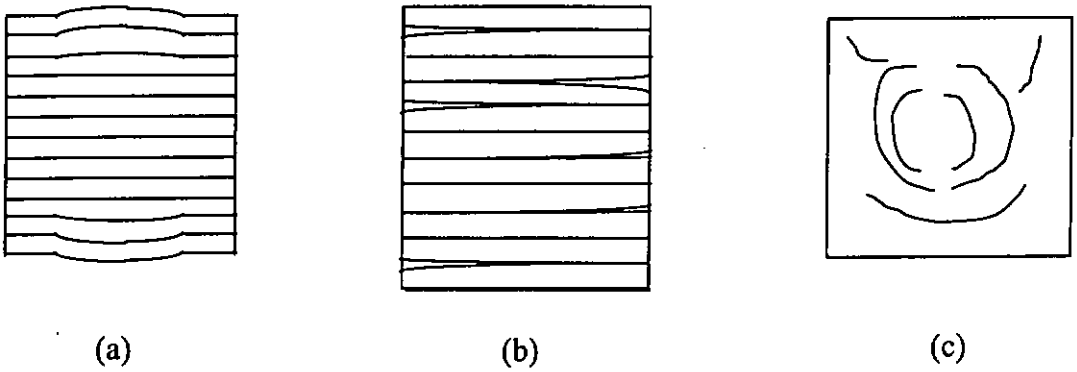

Figure 4.4 Three common defects in actuator fabrication caused by the rapid generation of organic vapour: (a) swollen shape top and bottom layers, (b) delaminations in between layers, (c) circular and line surface cracks on the top and bottom surfaces.

Thus, actions have to be taken to prevent the rapid vapour generation by modifying the binder burnout procedure. First, the binder decomposition profile was measured by thermogravimetric analysis (TGA). Thermogravimetry (TG) is a technique in which the mass of the sample is monitored against time or temperature during a programmed temperature increase in the sample in a specified atmosphere [Haines 1995]. 0.9PMN-0.1PT and PZT ceramic green sheets with platinum electrodes were tested. The samples were heated up to 630 °C at a heating rate of 20 °C/min. However, it is better to choose a lower heating rate to get a more accurate result. The weight change in the sample was recorded during heating and was displayed as a function of temperature. Since both ceramic green sheets with platinum electrodes are using the same PVA solution and platinum electrode material, their TGA results are very similar. Therefore, only the TGA result of a 0.9PMN-0.1PT ceramic green sheets with platinum electrodes is shown in Figure 4.5.

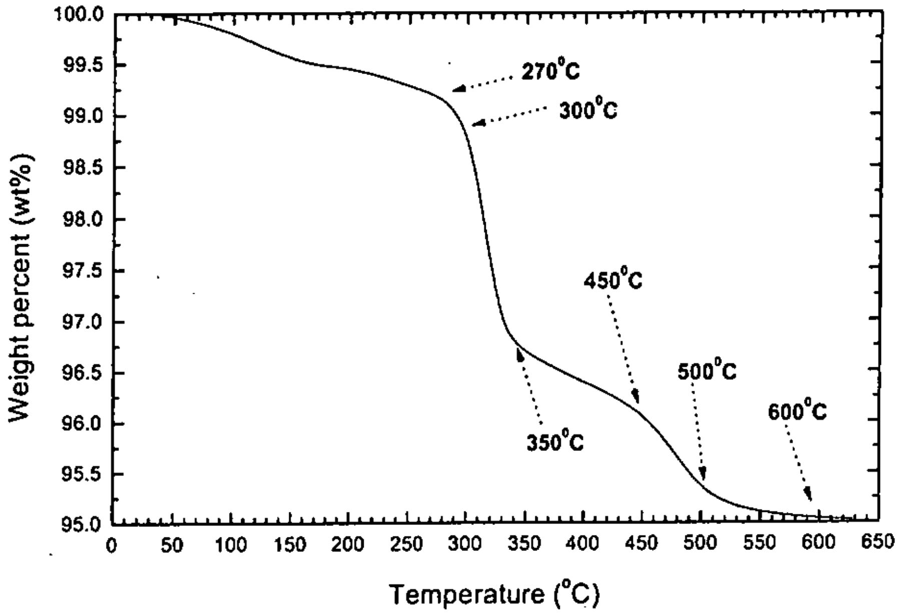

Figure 4.5 Weight percent of an electroded 0.9PMN-0.1PT ceramic green sheet as a function of temperature.

From Figure 4.5, there are several temperatures showing obvious weight changes. Reaction under 150 °C can be ignored because hot pressing will carry out before binder burnout. After that temperature, there are 5 points of rapid gas evolution, and the organics are completely decomposed at 600 °C. Based on this result, a burnout procedure can be established such that those temperatures are taken as "hold points".

The burnout procedure was performed by sandwiching the sample in-between two brass plates; due to the good thermal conductivity of the metal, it can help to release heat from the sample. Moreover, the plates would act as a heavy mass to suppress the force generated by gas evolution. The total burnout time is about 33 hours, which is much shorter than the time claimed in some former reports [Bridger 1996, Chen 1996, Im 2000, Pilgrim 1994] and no cracks and delaminations were found. It is noted that the whole setup should be soaked in alumina powders in order to control the temperature difference. Figure 4.6 shows the burnout temperature profile. Figure 4.7 shows the SEM micrographs of two samples: (a) without following the burnout profile of Figure 4.6 and was not sandwiched between two brass plates, (b) following the burnout profile and was sandwiched between two brass plates. It is obvious that the sample without following the suggested procedures contains cracks and delaminations but the other one does not.

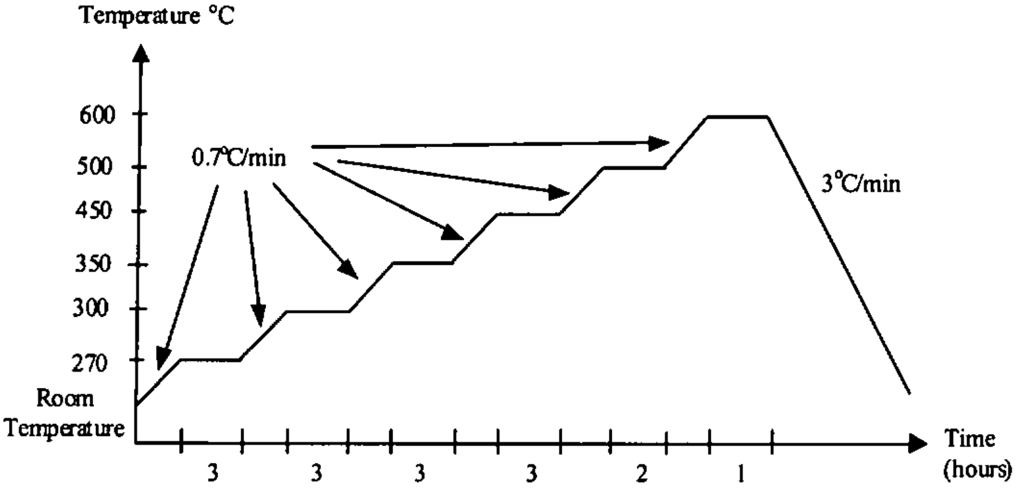

Figure 4.6 Binder burnout temperature profile of the multilayer actuator.

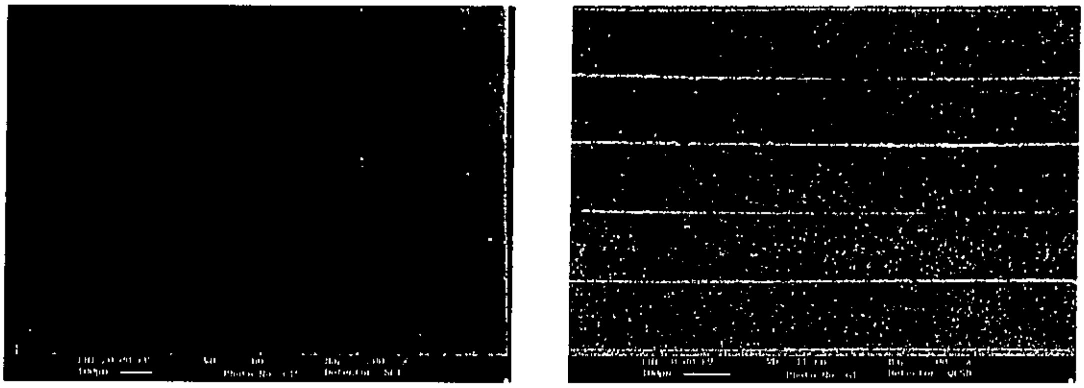

Figure 4.7 SEM micrographs of two samples: (a) without following the burnout profile of Figure 4.6 and was not sandwiched between two brass plates, (b) following the burnout profile and was sandwiched between two brass plates.

4.7 Sintering

A multilayer actuator was formed after the sintering process. This process is to densify the ceramic which results in overall shrinkage of the ceramic and metallic metal electrode. However, the physical parameters of ceramic and metallic electrode are different, which would result in shrinkage mismatch and it would cause lack of adhesion of the multilayer actuator, consequently, flaws would result. In order to avoid the existence of flaws, mass has to be added onto the sample during sintering. Clean alumina crucible covers were used as the mass since its melting point is high and would not cause any contamination during sintering at high temperatures.

Sintering temperatures for PZT and 0.9PMN-0.1PT multilayers are 1285 °C and 1250 °C respectively, which are the same as the sintering temperatures of bulk samples. At the start of sintering, a slow temperature rise is still necessary. The reason is that cracks would occur during rapid shrinkage of the actuator. The temperature was increased from room temperature to 600 °C and then increased to 850 °C for presintering. The temperature was finally increased to the required sintering temperature for the two materials. During sintering, mass added onto the sample was about 250 g and the sintered sample was buffered by ceramic powders of the same material in order to prevent loss of the lead content. Thickness of each layer after sintering is ~145 μm. The PZT and 0.9PMN-0.1PT actuators have 70 and 60 layers, respectively. The total thickness shrinkage of the actuator was about 20 % and its width had decreased by 14 % to about 8.6 mm. Figure 4.8 shows the schematic diagram of preparing the multilayer sample for sintering and Figure 4.9 shows the multilayer sintering temperature profile.

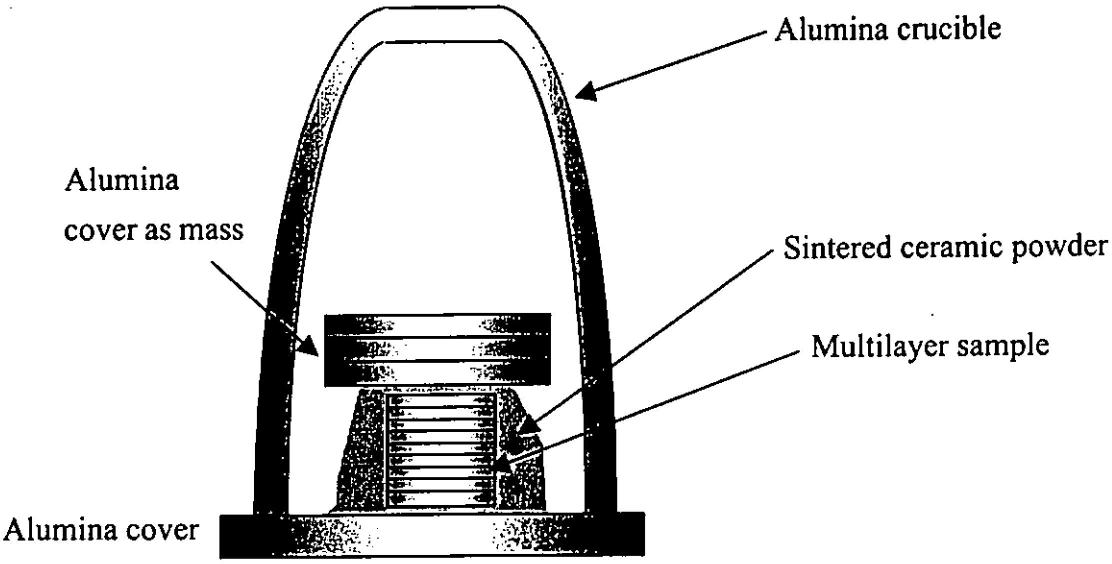

Figure 4.8 Schematic diagram of preparing a multilayer sample for sintering.

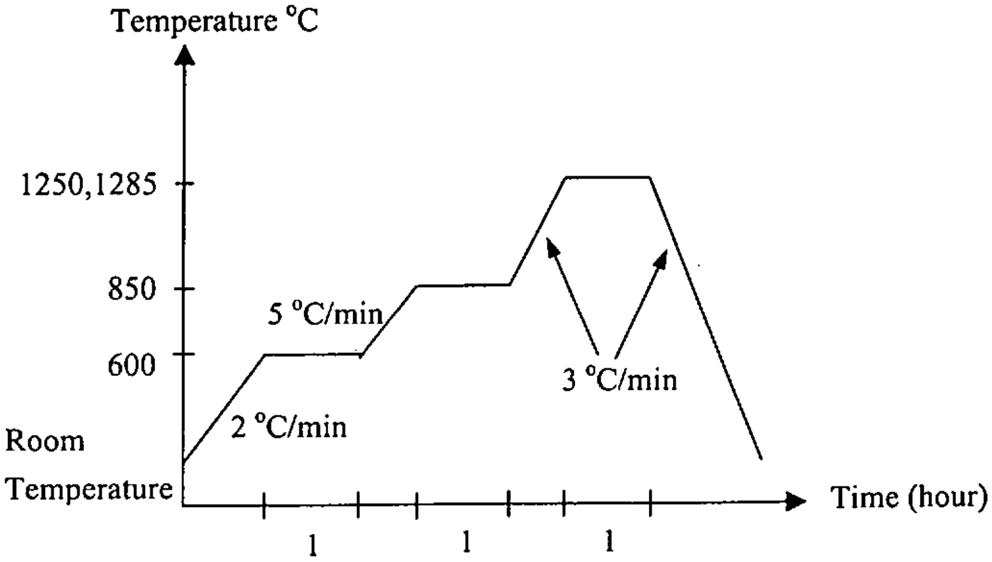

Figure 4.9 Sintering schedule of multilayer actuator.

4.8 External Electrical Connections

The sintered multilayer actuator can be used after connecting external wires to each internal layer. In order to get good connections between external connections and internal electrodes, the actuator should be polished prior to connect external electrodes. Wet and dry sandpapers (400, 800, 1200) were used to grind and polish both the edge and surfaces of the actuator. For displacement measurements described in Chapter 5, a shiny surface of the actuator is required for light reflections, so its surfaces should be polished as flat as possible.

Fired-on silver was used to connect all the alternate layers by fusing with the Pt internal electrodes. Silver ink was painted at the edge of each side. Care must be taken not to short-circuit the two external electrodes. Then the actuator was fired at 600 °C and held for 20 minutes. After all, external wires were soldered on each silver electrode. Figure 4.10 shows the schematic diagram of the structure of a multilayer actuator and Figure 4.11 shows the photo of the PZT and the 0.9PMN-0.1PT actuators.

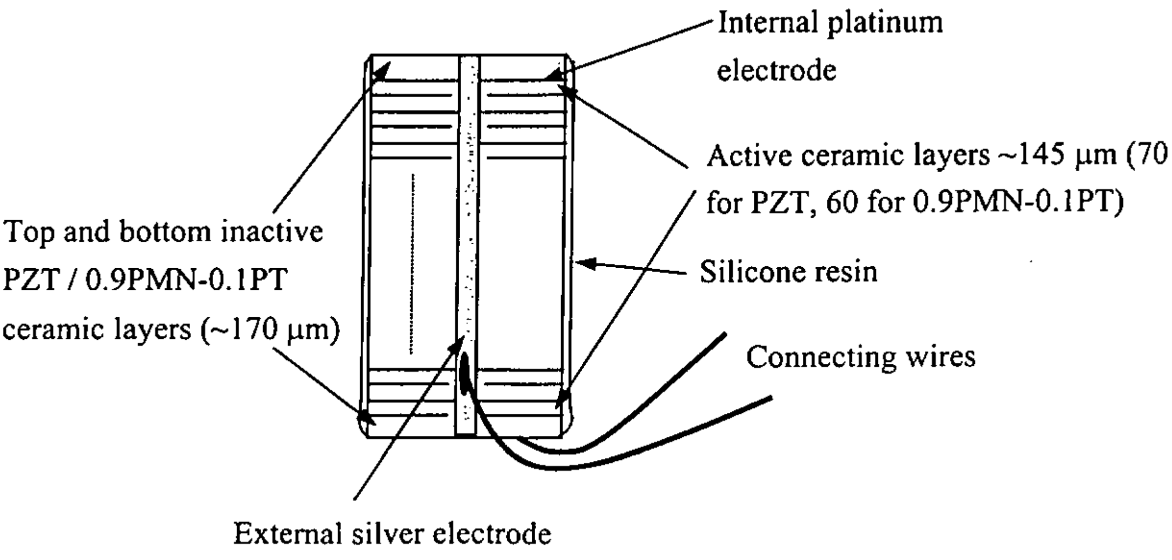

Figure 4.10 Schematic diagram of the structure of a multilayer actuator.

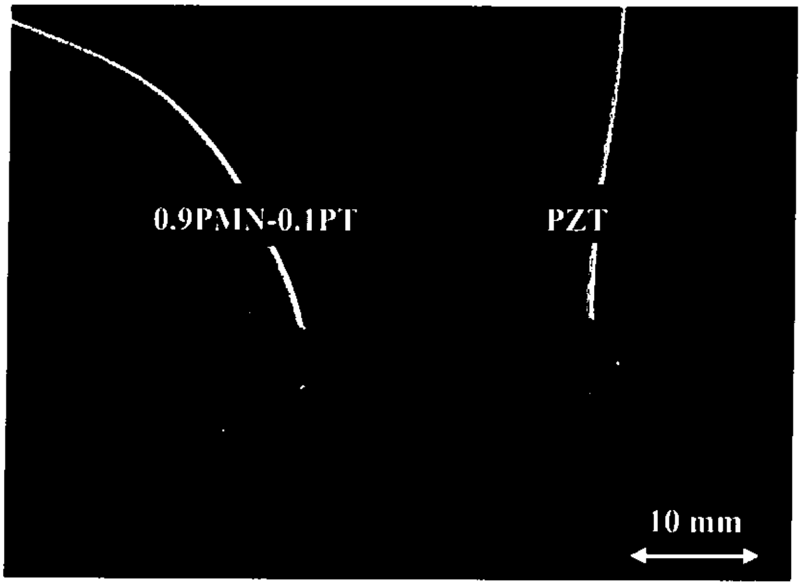

Figure 4.11 Photograph of the PZT and the 0.9PMN-0.1PT actuators.

4.9 Resin Coating

Referring to the configuration of a multilayer actuator, its internal electrode would expose externally to air at the edge of an actuator, which would cause electric sparking easily when it was driven with a high electric field. Therefore, it is necessary to coat a protective layer onto the edge of an actuator. The material used for shielding the actuator was a transparent silicone resin supplied by Dow Corning. Its model number is 1-2577 conformal coating [Dow Corning Corporation 1987]. This type of coating is usually used as a protective coating for rigid and flexible circuit boards, thick film circuitry, and for filling some porous substances to improve moisture resistance. It offers good dielectric properties at both high and low frequencies and good thermal-shock resistance. It also has high resistance to moisture. When the resin cures, it becomes elastoplastic with good weatherability.

Other than the above advantages, it also shows good electrical and physical properties when cured. Some typical properties can be referenced from Table 4.2. It is easy to brush on and it is flexible over a wide temperature range from –65 °C to 200 °C. Furthermore, it is easy to repair.

Table 4.2 Typical physical and electrical properties of the cured silicone resin 1-2577 from Dow Corning. [Dow Corning Corporation 1987]

Physical Properties			
CTM 0001A[1]	*Specific Gravity at 25 °C*	1.11	
CTM 0137A	*Tensile Strength, MPa at 25 °C*	3.45	
CTM 0137A	*Elongation, % at 25 °C*	30	
CTM 0420	*Coefficient of thermal Expansion, m/m/°C*	2.1×10^{-4}	
CTM 0224	*Thermal Conductivity, cal/sec/ cm^2/cm/°C*	2.9×10^{-4}	
CTM 0248	*Water Absorption, 100 hrs at 25 °C, %*	0.11	
ASTM D 1653	*Water Vapor Transmission, gms/cm^2/cm*	0.013	
Electrical Properties[2]		*Dry*	*Wet*[3]
CTM 0114	*Dielectric Strength, 10-mil film, volts/mil*	1100	976
CTM 0112	*Dielectric Constant, at 10^2 Hz (10^5 Hz)*	2.54 (2.51)	2.59 (2.56)
CTM 0112	*Dissipation Factor, at 10^2 Hz (10^5 Hz)*	0.00220 (0.00097)	0.00346 (0.00128)
CTM 0249	*Volume Resistivity, Ω/cm*	1.0×10^{14}	0.9×10^{14}

[1] In most cases, CTMs (Corporate Test Methods) correspond to ASTM standards tests.

[2] These properties indicate 5-day room temperature cure of 75-mil slab, unless otherwise indicated.

[3] Soaked in water for 24 hours.

The resin was coated onto the actuator by brushing. For ease of brushing, acetone was used to dilute the resin. Resin mixed with acetone was brushed onto the actuator slowly to reduce generation of bubbles. Normally, it takes less than 1 hour for the resin to cure to a tack-free state. Actuators can be handled at that time although curing has not been completed. The curing time can be reduced by heating the painted sample at 80 °C for 10 minutes after 10 minutes curing at room temperature. Then other faces were painted afterwards. It needs 5 days for total curing at room temperature. The thicker the coating, the longer the curing time required. Before adequate curing has developed, it should not be exposed to cold temperatures, otherwise, crack would be initiated.

4.10 Poling and Short-Circuit Annealing

For the PZT multilayer actuator, it is required to align all domains so as to elicit the piezoelectric properties. It can be achieved by applying a poling field of 2 kV/mm at 130 °C to the sample. Procedure and setup for poling a multilayer are the same as that for poling a bulk ceramic which was described in Section 2.2.3.

Since the layers in the multilayer device is connected electrically in parallel, so that the field is applied in the thickness direction of each active layer. The poling voltage required can be expressed as:

$$\begin{aligned} \textit{Poling voltage} &= \textit{Poling field} * \textit{Thickness of each active layer} \\ &= 2\ kV/mm * 145\mu m \\ &= 290\ V \end{aligned}$$

The poling field was kept for 20 minutes at 130 °C and then the temperature was decreased with the field kept on. Electric field should be cut-off when the temperature has been dropped to 70 °C.

To speed up the aging after poling, the poled PZT multilayer sample should be short-circuit annealed. It can be done by connecting the terminal wires together and placed the actuator inside a MEMMERT programmable oven at about 45 °C for 1 day. The moderate temperature enhances charge mobility. The stress cause by poling can be released after annealing. Consequently, piezoelectric property of the actuator is stabilized.

Chapter 5.

Characterizations of Multilayer Actuators

5.1 Introduction

Based on the fabrication process discussed in the previous Chapter, a piezoelectric PZT multilayer actuator and an electrostrictive 0.9PMN-0.1PT multilayer actuator were fabricated. Their physical, electromechanical, and mechanical properties were characterized and discussed in this Chapter.

For physical property characterizations, SEM micrographs of the devices were taken and their effective densities were measured. For the piezoelectric actuator, its electromechanical resonant modes can be observed by the use of the HP 4194A impedance / gain phase analyzer and these resonant modes can be used to determine several electrical parameters of the piezoelectric actuator, including the vibrational mode frequencies (f_r, f_a), capacitance and loss tangent ($tan\delta$), electromechanical coupling factor (k_{33}) and effective mechanical Q-factor (Q_m). For the electrostrictive actuator, its dielectric spectrum and polarization were measured.

Generally, mechanical characterization of the actuator includes the measurement of displacement and blocking force. Nevertheless, for the wireclamp application discussed in the next Chapter, the blocking force is not the main concern since blocking force of an actuator is much greater than the force required for the application. The displacement of these actuators under either ac or dc signal were measured by the Polytec vibrometer and the Fotonic fiber optic sensor, respectively. For the electrostrictive actuator, its displacement response due to the dc-biased effect would be examined.

5.2 Effective Density

According to the Archimedes' principle discussed in Chapter 3, density of sample can be measured by weighing its dry mass and mass in water. For multilayer actuator, it is composed of the electrode (platinum) and ceramic, therefore, the actuator density is the combination of both materials. Based on the series model of a multilayer actuator explained in [Wersing 1986], the effective density of an actuator can be expressed as:

$$\rho^{*} = \rho \cdot \frac{(1+\alpha\gamma)}{(1+\alpha)} \qquad (5.1)$$

where ρ^* is the effective density of the multilayer actuator, ρ is the density of the ceramic material, α is the ratio of the thicknesses (t_M) of all the metallic electrode (platinum) layers to the thicknesses (t_c) of all the ceramic layers: $\alpha = t_M / t_C$ and γ is the ratio of the metallic electrode density to the ceramic density.

Table 5.1 shows the physical properties of the PZT and 0.9PMN-0.1PT multilayer actuators including the dimensions, effective densities and the calculated ceramic materials densities. Density of the platinum electrode is about 21000 kg/m^3. The results of the calculated densities of the ceramics and actual densities of the ceramics are roughly the same for both materials which show the validity of the model.

Table 5.1 Physical properties of the PZT and 0.9PMN-0.1PT multilayer actuators.

	PZT	**0.9PMN-0.1PT**
Length x width	8.2 mm x 8.2 mm	8.36 mm x 8.5 mm
Thickness of active layers	145 μm	145 μm
Thickness of the top and bottom inactive layers	170 μm	170 μm
No. of active layers	70	60
Total Length	10.46 mm	9.34 mm
Dry mass	5.3168 g	5.2526 g
Effective Density of actuator	7780 kg/m^3	8361 kg/m^3
Densities of ceramics	7600 kg/m^3	7934 kg/m^3
Calculated densities of ceramics	7595 kg/m^3	7940 kg/m^3

5.3 Microstructure

Before estimating the electromechanical performance of the actuators, it should be ensured that there were no cracks or delaminations between each layer. Multilayer actuators required intimate contact between the ceramic layers and the metallic electrode layers. If pores or cracks exist, its performance would be degraded and it would break under high voltage operations. Figure 5.1 shows the SEM (Backscattering) micrographs of the polished cross-sectional views of (a) the PZT actuator and (b) the 0.9PMN-0.1PT actuator. No cracks or delaminations can be observed. As shown in Figure 5.2, the interfacial layers between the ceramic layers are completely filled with the metallic electrode and no gaps can be observed for the PZT and 0.9PMN-0.1PT multilayer actuators.

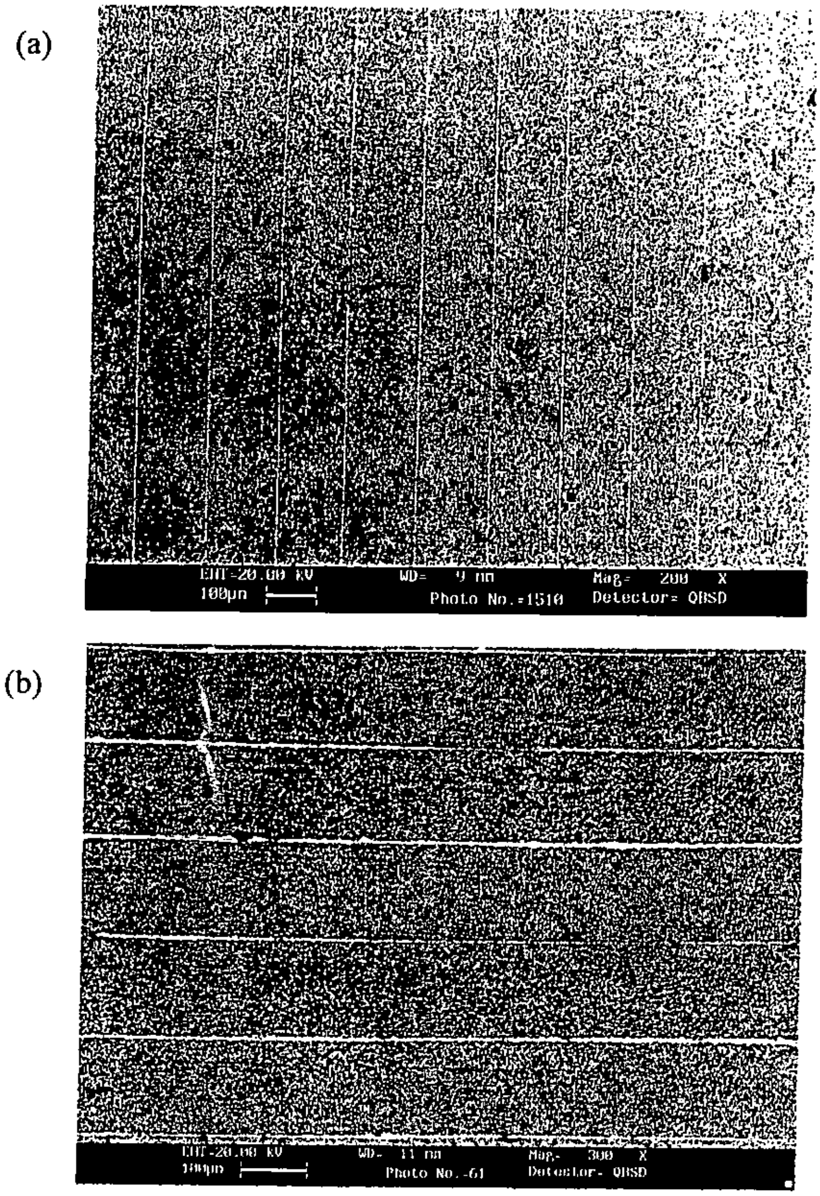

Figure 5.1 SEM micrograph (Backscattering) of the cross-sectional view of (a) the PZT multilayer actuator and (b) the 0.9PMN-0.1PT multilayer actuator.

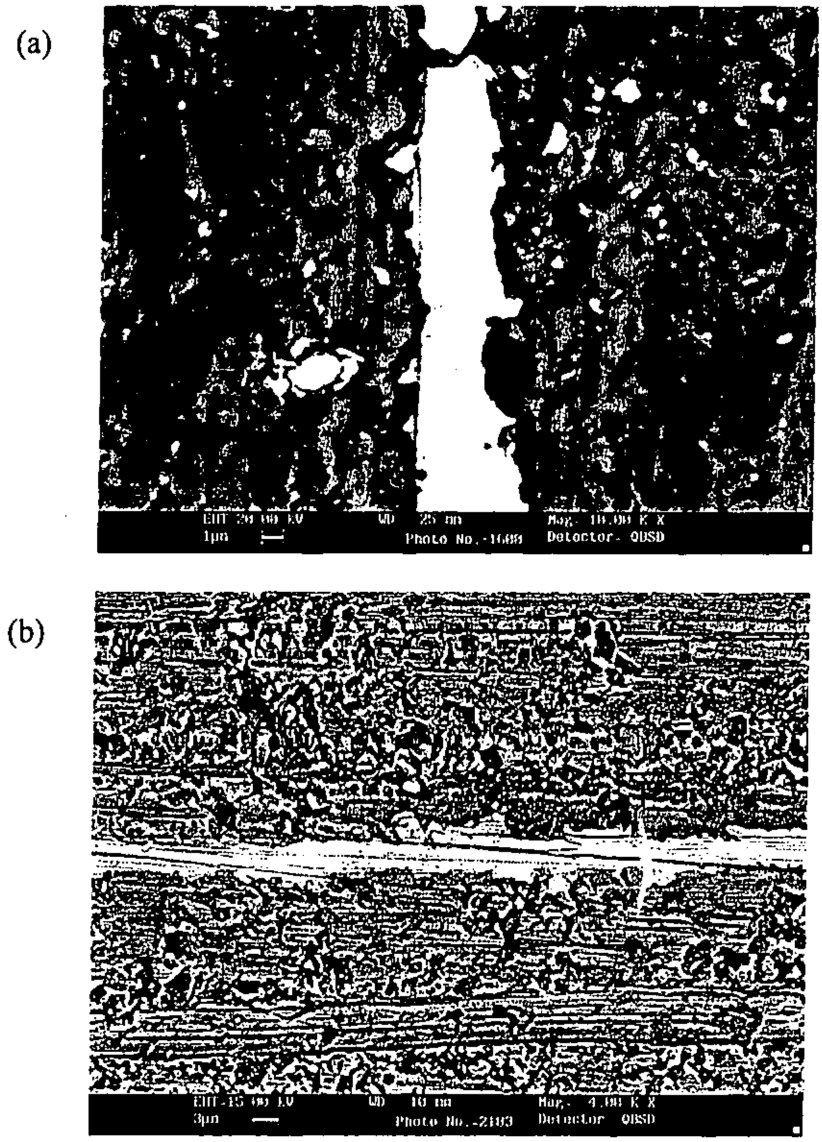

Figure 5.2 Magnified cross-sectional view of (a) the PZT multilayer actuator and (b) the 0.9PMN-0.1PT multilayer actuator.

5.4 Impedance Measurement of the PZT Multilayer Actuator

Piezoelectric actuator is an electromechanical device which can convert an applied electrical signal to mechanical vibrations. At certain frequencies, various vibrational modes are excited. These electromechanical resonance modes can be observed from the impedance / phase versus frequency spectrum.

5.4.1 Vibrational Modes

The PZT and 0.9PMN-0.1PT multilayer actuators are operated in the thickness direction and their geometries are in bar shapes. There are two modes of vibrations for this type of actuator. The first one is the vibrational mode in the polarization direction; it is the longitudinal length extensional mode *(Longitudinal mode).* The second one is the vibrational mode in the transverse direction which is called the transverse length extensional mode *(Transverse mode).* Figure 5.3 shows a schematic model of a vibrating piezoelectric multilayer actuator.

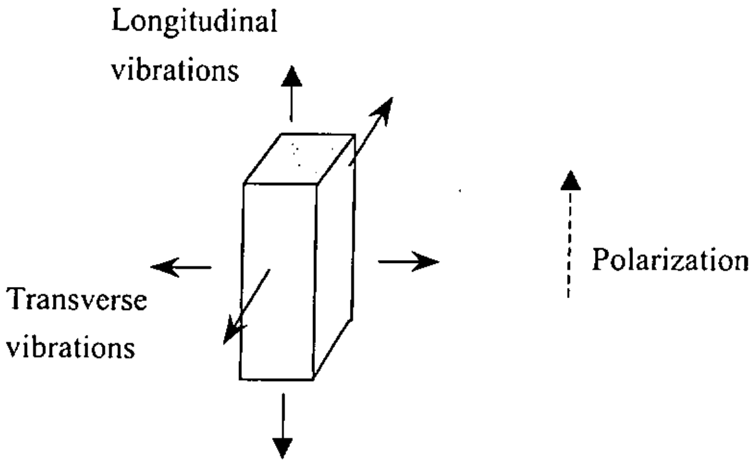

Figure 5.3 Vibrational modes of a piezoelectric multilayer actuator.

The following equations can be used to estimate the resonance frequency of the two modes mentioned above [ANSI / IEEE Std. 1988]:

Fundamental longitudinal mode:

$$f_r = \frac{1}{2L}\sqrt{\frac{1}{\rho s_{33}^{E}}} \tag{5.2}$$

Fundamental transverse mode:

$$f_r = \frac{1}{2W}\sqrt{\frac{1}{\rho s^E_{11}}} \tag{5.3}$$

where f_r is defined as the resonant frequency of the vibration mode (approximately equal to the frequency of minimum impedance), L and W are the length and width of the actuator, respectively. ρ is the effective density of the actuator; s^E_{33} and s^E_{11} are the elastic compliances of the ceramic material measured under a short circuit condition.

5.4.2 Flaw Detection by Impedance-Frequency Scans

A question would be raised is that about why there are only two modes and their harmonics? Would the thickness vibrational modes of each ceramic layer occur? The answer is no, since for a good actuator, its layers should be tightly bonded together without flaws, all ceramic layers are clamped or it can be said that no discrete layers exist. This explains why there are no other vibrational modes being observed. According to this reason, the impedance measurement can also be used to detect defects in a piezoelectric multilayer actuator [Kahn 1996]. The vibrational frequencies of the standing waves in an actuator depend on the actuator geometry and its acoustic velocity. Any internal defects would change the acoustic velocity of the structure and reflect the wave at different frequencies so that other vibration modes can be observed. As presented by Bechou et. al. [Bechou 1996], internal defects would cause attenuation in the electrical impedance of a natural mode. Moreover, other modes created by defects would occur and coupled with the natural modes such that multiple resonance or anti-resonance could be observed.

Other than the impedance-frequency scan technique, there are several kinds of non-destructive flaw detection method described previously in the literature, namely: X-ray radiography [Bray 1992], acoustic emission measured as a function of applied mechanical and electrical stress [Kahn 1983], scanning acoustic microscopy [Ousten 1990], methanol testing [Bechou 1996], partial discharge measurements [Bechou 1996] and impedance spectroscopy [Bechou 1996], etc. These are outside the scope of this thesis and will not be discussed in detail.

5.4.3 Capacitance and Loss Tangent

Capacitance of the multilayer actuator is the capacitance of all active layers. All layers of the actuator were connected mechanically in series, but they are electrically in parallel. Therefore, capacitance of the actuator is the sum of the capacitance of each independent layer. It was measured at 1 kHz and at room temperature by an ac signal of 0.5 V_{rms}. The total efficiency of an actuator not only depends on the mechanical loss, but also depends on the dielectric loss factor, and this loss factor is defined as the loss tangent of the angle (*tan δ*). It represents the ratio of the resistance to reactance in a parallel equivalent circuit of the ceramic element.

$$DF = \tan\delta = \frac{1}{Q_E} \qquad (5.4)$$

where Q_E is the electrical damping. For an actuator with low loss tangent, the heat generation would then be reduced.

5.4.4 Longitudinal Electromechanical Coupling Factor

The longitudinal electromechanical coupling factor k_{33} can be calculated by equation 5.5 when the driving frequency is far below the mechanical resonance frequency.

$$k^2{}_{33} = \frac{d^2{}_{33}}{s^E_{33}\varepsilon^T_{33}} \tag{5.5}$$

When the actuator is operated under dynamic conditions, the k_{33} can be estimated by the equivalent circuit analysis in terms of the resonance and anti-resonance frequencies of its longitudinal mode measured by the HP 4194A impedance analyzer. The equation for calculation is:

$$k^2{}_{33} = \frac{\pi}{2}\frac{f_a}{f_r}\tan\left(\frac{\pi}{2}\frac{f_a - f_r}{f_a}\right) \tag{5.6}$$

5.4.5 Mechanical Q_m Factor

As discussed before in Chapter 3, mechanical Q_m (quality) factor is the ratio of the reactance to the resistance in the series equivalent circuit representing the piezoelectric actuator. With the use of the equivalent circuit analysis built in to the HP 4194A impedance analyzer, the effective mechanical Q_m factor of the multilayer actuator can be estimated by analyzing the equivalent circuit of its thickness mode. This mechanical Q_m factor is also related to the sharpness of the resonance frequency [ANSI / IEEE Std. 1988].

$$Q_m = \frac{\omega L}{R} \tag{5.7}$$

Other than using the equivalent circuit analysis through the analyzer, it can also be calculated as in equation 5.8 [ANSI / IEEE Std. 1988].

$$Q_m = \frac{1}{2\pi f_r Z_m C_0}\left(\frac{f_a^{\,2}}{f_a^{\,2} - f_r^{\,2}}\right) \tag{5.8}$$

5.4.6 Results and Discussion

Figure 5.4 shows the impedance spectrum of the PZT multilayer actuator. As shown in Figure 5.4, the vibrational mode with the largest impedance variation occurred at the lowest frequency is the fundamental vibrational mode of the multilayer actuator in the longitudinal direction. This is followed by the fundamental vibrational mode of the actuator in the transverse direction. The vibration modes at higher frequencies are the harmonics of these two fundamental modes.

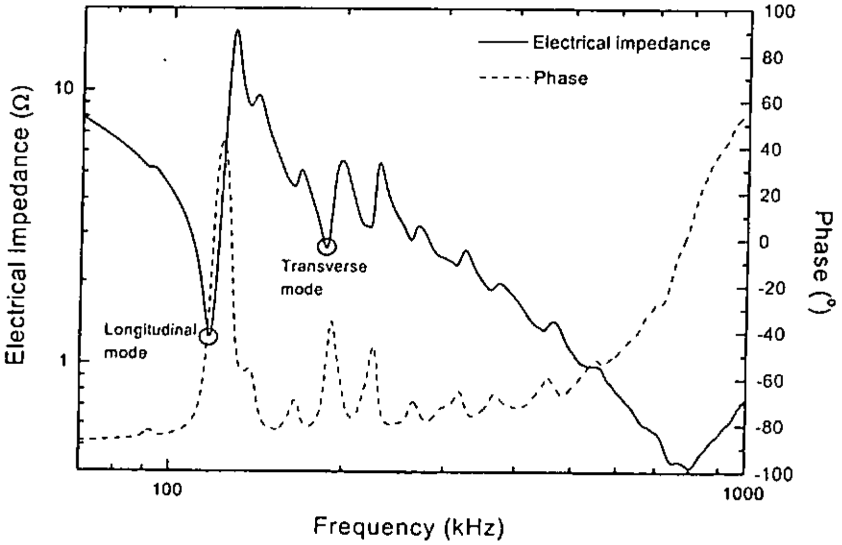

Figure 5.4 Impedance - frequency plot of the PZT multilayer actuator.

Figure 5.5a shows the longitudinal mode of the multilayer actuator. Its resonant frequency is at 118.6 kHz while Figure 5.5b shows its transverse mode. The resonant frequency of the transverse mode is at 188.7 kHz. A clear longitudinal mode and transverse mode of the actuator can be seen and show no multiple peaks near the resonant and anti-resonant frequencies. It can be concluded that there is little or no flaws exist in the actuator that adversely affect the thickness vibration of the actuator. Table 5.2 lists some important electrical properties of the PZT multilayer actuator. Since the aspect ratio (width to thickness) of the actuator is close to 1, value of the k_{33} measured under dynamic conditions may become smaller due to the mode coupling.

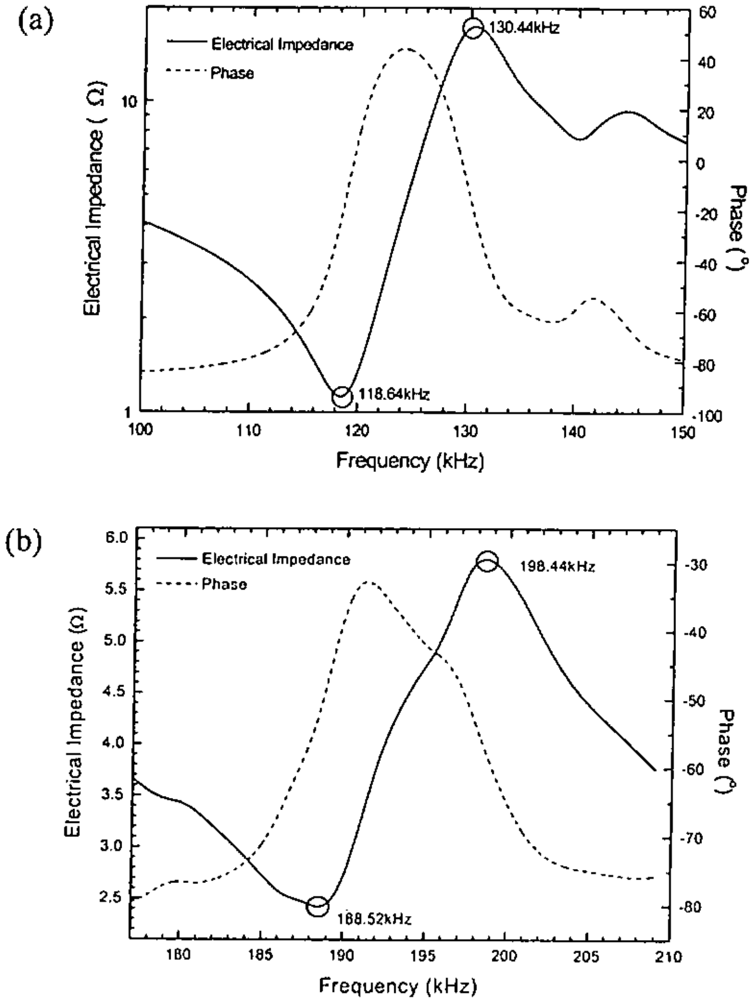

Figure 5.5 (a) Longitudinal mode and (b) transverse mode of the PZT multilayer actuator.

Table 5.2 Electrical properties of the PZT multilayer actuator

Electrical Properties	**Results**
Resonance frequency (Longitudinal mode) kHz	118.64
Anti-resonance frequency (Longitudinal mode), kHz	130.44
Resonance frequency (Transverse mode), kHz	188.68
Anti-resonance frequency (Transverse mode) kHz	198.44
Effective longitudinal elastic compliance s_{33}^E, $1x10^{-12}$ m^2/N	20.9
Effective transverse elastic compliance s_{11}^E, $1x10^{-12}$ m^2/N	13.4
Effective longitudinal electromechanical coupling factor, k_{33} *(dynamic condition)*	0.52
Effective longitudinal electromechanical coupling factor, k_{33} *(Static/ Quasi-static condition)*	0.72
Capacitance (1kHz), μF	0.28
Loss Tangent (%) (at 1kHz)	1.67
Effective Mechanical Q_m *factor*	25

5.5 Dielectric Behavior of the 0.9PMN-0.1PT Multilayer Actuator

Dielectric property is one of the important material properties of the 0.9PMN-0.1PT multilayer actuator. There are various reasons that would reduce the actuator dielectric permittivity. For example, existence of defects would cause air trapped inside the actuator, which would consequently reduce the dielectric permittivity of the whole structure. The other reason is the metallic electrode diffusion and the electroded area estimation.

The effective dielectric permittivity of the 0.9PMN-0.1PT multilayer actuator was estimated by its capacitance. The actuator was placed inside an ESPEC SU-240 oven and its weak field capacitance under different temperatures was measured by a computer-controlled HP 4194A impedance analyzer. The dielectric permittivity of the actuator can be calculated as:

$$C = \frac{\varepsilon_o \varepsilon_r n A}{t} \qquad (5.9)$$

where C is the capacitance of the actuator, ε_o is the permittivity of free space, ε_r is the effective dielectric permittivity of the actuator, n is the number of active layers, A is the electroded area and t is the thickness of each active layer.

Figure 5.6 shows the dielectric permittivity of the 0.9PMN-0.1PT actuator as a function of temperature measured at different frequencies: 10 Hz, 1 kHz, 10 kHz and 100 kHz. The effective dielectric permittivity of the multilayer actuator (line) was determined by equation 5.9. The symbols in Figure 5.6 represent the dielectric permittivity of the bulk ceramic.

Similar to other relaxor-based ferroelectric material, the maximum dielectric permittivity shifts to a higher temperature but with lower maximum values at higher measuring frequency. The maximum dielectric permittivity of the actuator measured at 1 kHz is at about 40 °C which is the same as that of the bulk 0.9PMN-0.1PT ceramic and it has a broad diffuse phase transition. It is obvious that the dielectric permittivity (line) of the actuator matches the values of that of a bulk sample (symbols). It can be assumed that all active layers were connected electrically in parallel such that the capacitance of an actuator is the summation of 60 active layers. This indicates that all ceramic active layers have good electrical contacts and little or no porosity or delaminations occur inside the actuator. The small difference between the bulk and actuator dielectric permittivities may be due to the inaccurate estimation of the internal electroded area of the actuator.

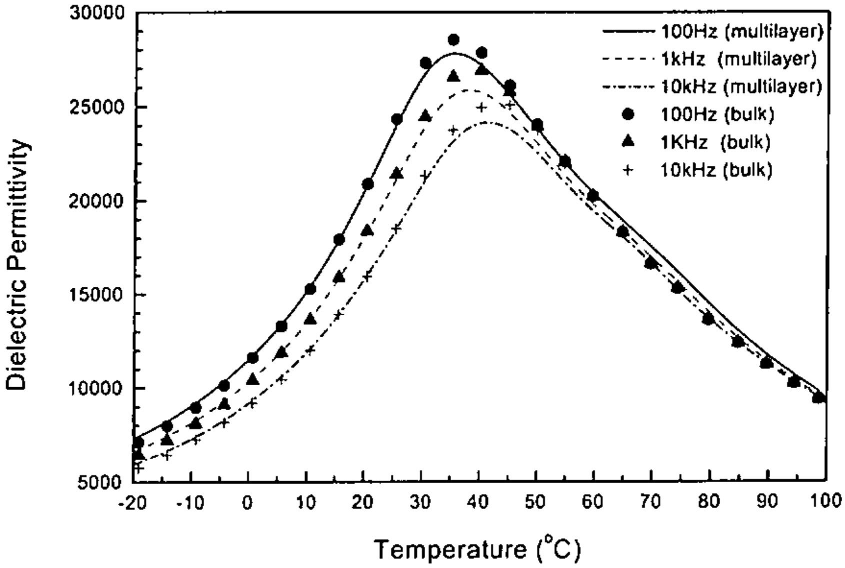

Figure 5.6 Dielectric permittivity as a function of temperature for the 0.9PMN-0.1PT multilayer actuator (line) and the bulk 0.9PMN-0.1PT ceramic (symbol).

5.6 Hysteresis-Loop Measurements of the 0.9PMN-0.1PT Multilayer Actuator

Polarization in the 0.9PMN-0.1PT multilayer actuator was measured as a function of electric field, such that a polarization-electric field curve (the P-E loop) is formed. PE-loop of the 0.9PMN-0.1PT multilayer actuator was measured by the aixACT TF Analyzer 2000 system. Within the TF Analyzer 2000 system, a FE-module was connected to the actuator to investigate its ferroelectric hysteresis loop. A H.V. amplifier was connected to the actuator such that a maximum voltage of 200 V could be applied to the actuator. Figure 5.7 shows the setup of this ferroelectric hysteresis measurement.

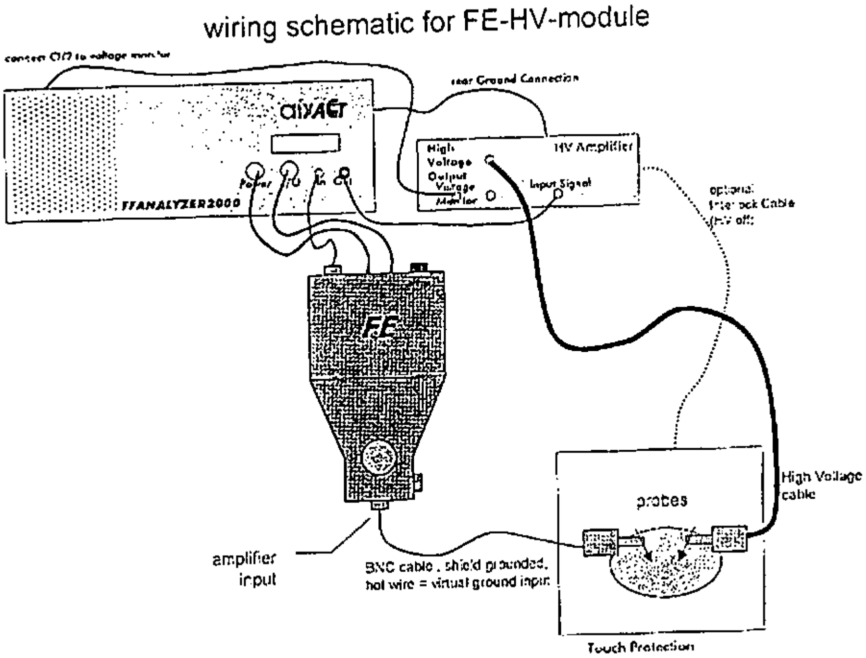

Figure 5.7 Setup of the ferroelectric hysteresis measurement of the 0.9PMN-0.1PT multilayer actuator by the TF Analyzer 2000 system with a high voltage module. [aix-ACCT 2000]

Figure 5.8 shows the ferroelectric hysteresis loops of the 0.9PMN-0.1PT multilayer actuator under different levels of electric field. From Figure 5.8a, a linear relationship between the polarization of the actuator and electric field is seen at low field and a small hysteresis of about 2 $\mu C/cm^2$ is observed. From Figure 5.8b, the P-E relationship becomes nonlinear when the electric field exceeds 0.4 kV/mm, but the polarization hysteresis is roughly the same as that in Figure 5.8a. From Figure 5.8c, polarization of the actuator becomes saturated when the electric field increases up to 1 kV/mm, a slim PE-loop is formed. The saturated polarization P_s of the actuator at 1 kV/mm is about 22 $\mu C/cm^2$. This value is roughly the same as that of a bulk 0.9PMN-0.1PT ceramic.

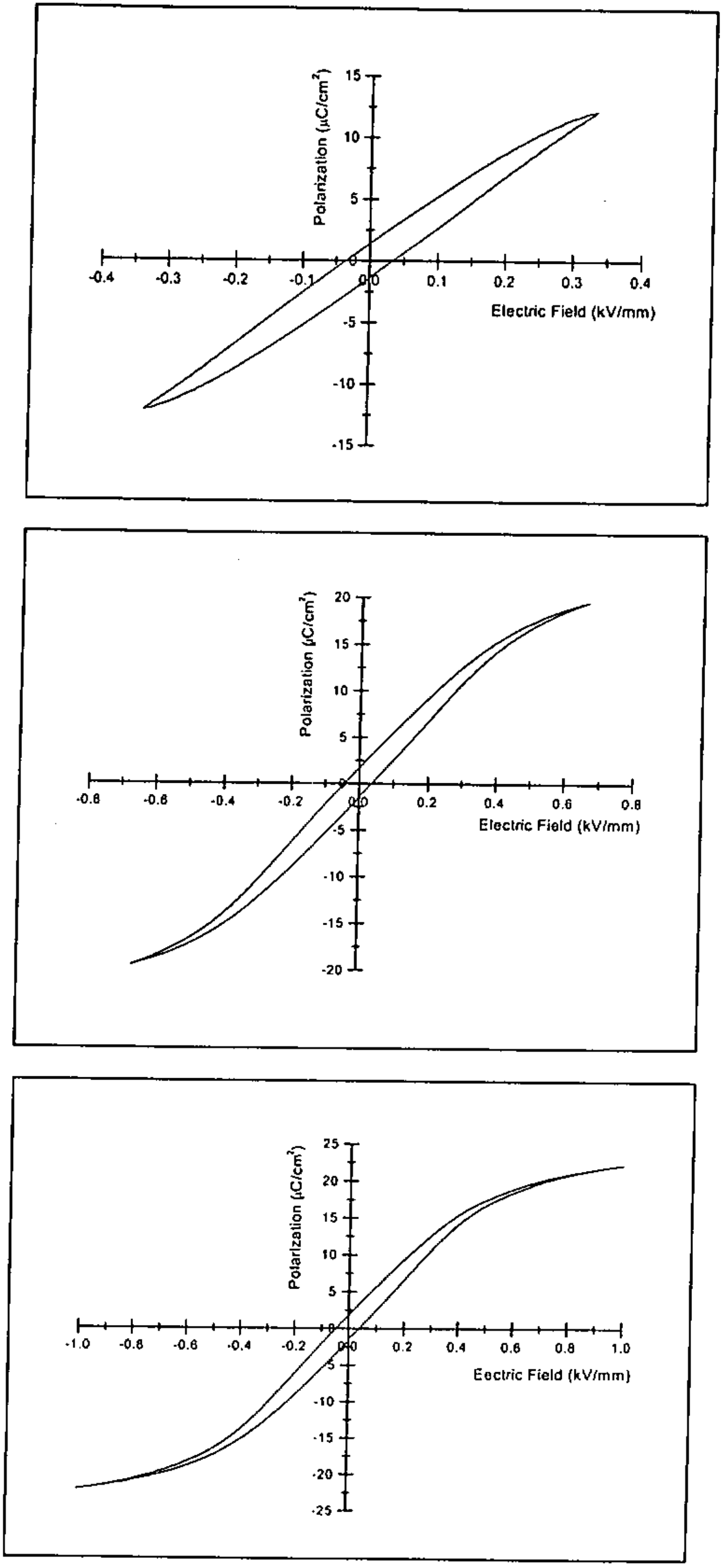

Figure 5.8 Ferroelectric hysteresis loops of the 0.9PMN-0.1PT multilayer actuator under (a) 50 V (0.34 kV/mm), (b) 100 V (0.69 kV/mm) and (c) 150 V (1.03 kV/mm).

5.7 Displacement Measurements

The main difference between a bulk ceramic actuator and a multilayer actuator of the same dimension is that the later can produce the same displacement but with a much smaller driving voltage. It explains why measuring the strain response of a multilayer actuator is so interesting. In this part, the strain responses of the PZT and 0.9PMN-0.1PT multilayer actuators measured under dc driving field and ac driving field by using the Fotonic sensor and the vibrometer are presented respectively.

5.7.1 Operation Mechanism of the Fotonic Sensor

Rigid displacements of both multilayer actuators were measured by the use of the MTI-2000 Fotonic sensor and the MTI-2062R sensor probe. The MTI-2062R sensor probe was used because its transmitting and receiving fibers are randomly distributed which can give high displacement sensitivity within a short range. The Fotonic sensor utilizes several pairs of light-transmitting and light-receiving fibers. They operate based on the interaction between the field of illumination of the transmitting fibers and the field of view of the receiving fibers. At zero measuring distance, all the light is reflected directly back to the transmitting fibers, so that no light can be captured by the receiving fibers, and no output is produced. By increasing the measuring distance, more light can then be captured by the receiving fibers. The relationship holds until the entire faces of the receiving fibers are illuminated with the reflected light. Further increases in the measuring distance will cause the diverging field of reflected light to exceed the field of view of the receiving fiber, thus causing a reversal in the output-versus-distance signal relationship. Figure 5.9 shows the illustration of the displacement sensing mechanism and Figure 5.10 shows the output-versus-distance response curve [Mechanical Technology Inc. 1991].

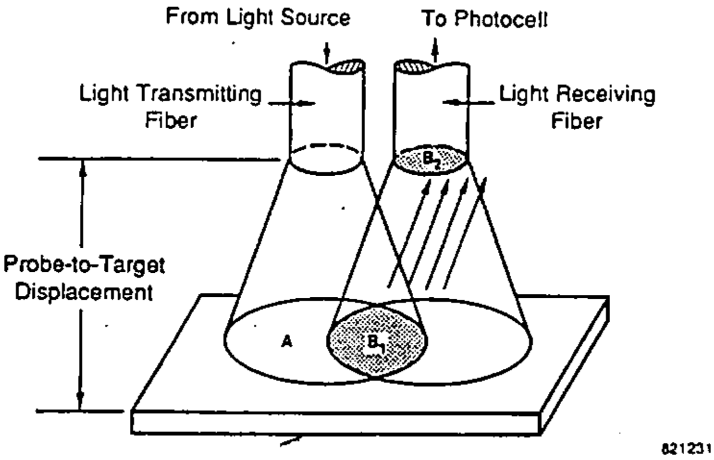

Figure 5.9 Illustration of the displacement sensing mechanism by two adjacent fibers [Mechanical Technology Inc. 1991].

From Figure 5.10, it can be seen that there are two measuring ranges. Range 1 is highly sensitive, it starts from zero measuring distance to the optical peak, the slope of the output-displacement curve is positive. Range 2 is less sensitive but with a longer measuring range. The slope of the output-displacement curve is negative. The output-displacement relationship in Range 1 depends on the fiber diameter, the relative position of the transmitting and receiving fibers, and the numerical aperture of the fibers. While the output-displacement relationship in Range 2 depends on the field intensity which varies according to the inverse square law. [Mechanical Technology Inc. 1991]

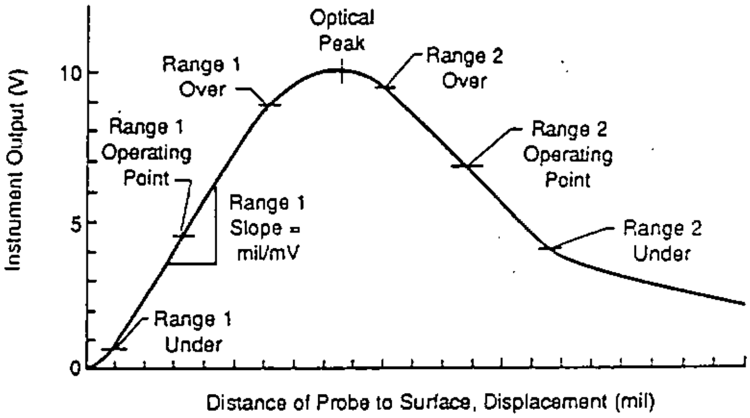

Figure 5.10 Output-versus-distance response curve [Mechanical Technology Inc. 1991].

Figure 5.11 shows the setup for the displacement measurement of PZT and 0.9PMN-0.1PT multilayer actuators. Both actuators were placed vertically under the probe tip so that the displacement generated can be measured when they were driven by a NF electronic instruments HSA 4014 high-speed bipolar amplifier. This amplifier can provide a dc bias voltage together with an ac driving signal. It is more convenient than using two voltage sources with a protection circuit for driving a low voltage actuator.

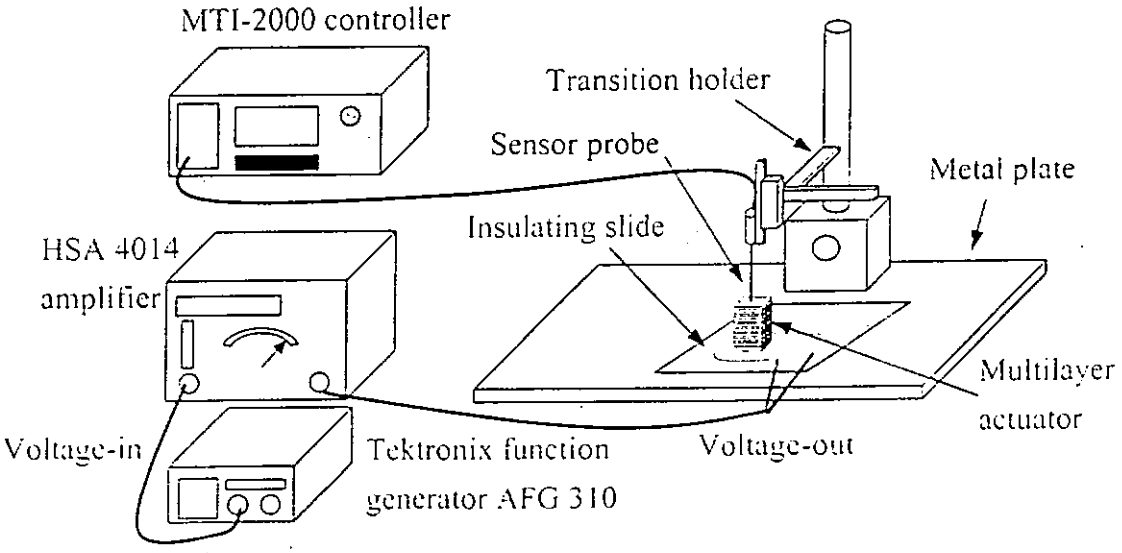

Figure 5.11 Setup of displacement measurement using the Fotonic sensor.

The longitudinal and transverse strain responses of the PZT and 0.9PMN-0.1PT multilayer actuators under a dc field were measured and their effective piezoelectric coefficients d_{33} and d_{31} under high electric fields can be obtained.

5.7.2 Results and Discussion

To operate a PZT multilayer actuator, the polarity has to be identified first. If the actuator is driven in an opposite direction to its polarization direction, it will be depoled and loss its piezoelectric property. Therefore, the actuator would be driven in the positive voltage only. Figure 5.12 shows the longitudinal displacement and strain of the PZT actuator as a function of dc voltage and electric field, respectively. It can generate a 3.8 μm displacement under a dc voltage of 100 V with a hysteresis of about 13 %.

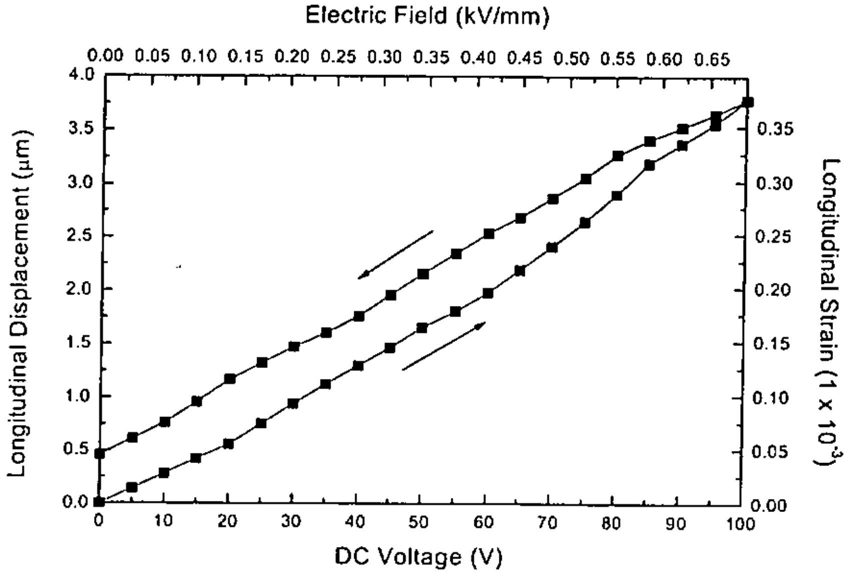

Figure 5.12 The longitudinal displacement and strain of the PZT actuator as a function of dc voltage and electric field, respectively.

Longitudinal strain of an actuator is the ratio of its displacement over the total thickness of all active layers, while the electric field is the ratio of the voltage applied over each active layer. For this PZT actuator, the total thickness of the 70 active layers is 10.15 mm. Calculation of the effective longitudinal piezoelectric coefficient d_{33} of the multilayer actuator is the same as that of a bulk ceramic. It can be expressed as:

$$d_{33} = x_{33} / E \tag{5.10}$$

where x_{33} is the longitudinal strain of the multilayer actuator and E is the electric field. The calculated d_{33} of the PZT multilayer actuator is about 550 pm/V.

Figure 5.13 shows the transverse displacement and strain of the PZT multilayer actuator as a function of dc voltage and electric field, respectively.

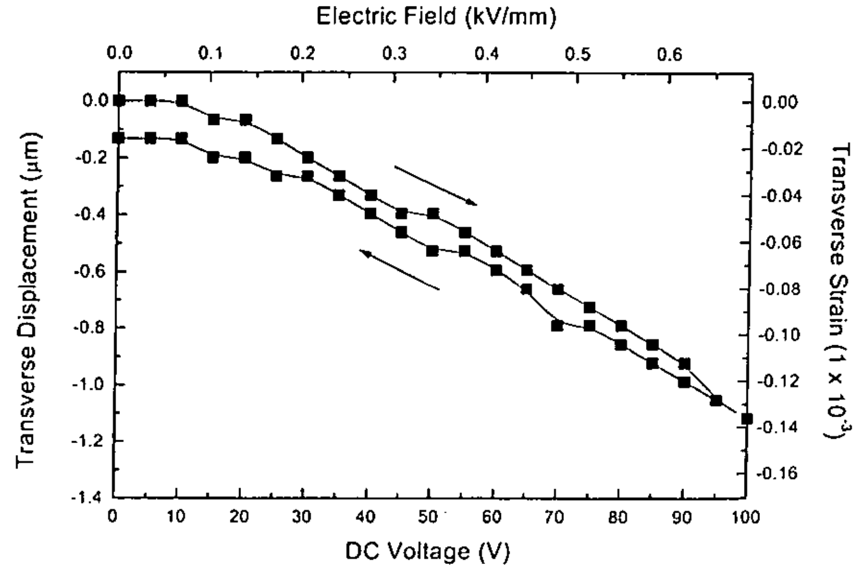

Figure 5.13 Transverse displacement and strain of the PZT multilayer actuator as a function of dc voltage and electric field, respectively.

It can generate a −1.12 μm displacement under a dc voltage of 100 V with a hysteresis of about 9 %. Transverse strain of the PZT actuator is the ratio of its transverse displacement to its width. The effective transverse coefficient of the multilayer actuator d_{31} can be calculated as:

$$d_{31} = x_{31} / E \tag{5.11}$$

where x_{31} is the transverse strain of the multilayer actuator and E is the electric field. The calculated d_{31} of the PZT multilayer actuator is about -201 pm/V.

In order to find the effective electrostrictive coefficient of a 0.9PMN-0.1PT multilayer actuator, it is required to measure the electrostrictive strain. Figure 5.14 shows the longitudinal displacement and strain of the 0.9PMN-0.1PT actuator as a function of ac voltage and ac electric field, respectively at 1 Hz. Its electrostrictive displacement is about 4.8 μm at 145 V and the displacement curve is proportional to the square of the applied voltage without hysteresis. For this 0.9PMN-0.1PT actuator, the total thickness of the 60 active layers is 8.7 mm. Hence, electrostrictive strain of the actuator is about 0.55 x 10^{-3} under an ac electric field of 1 kV/mm.

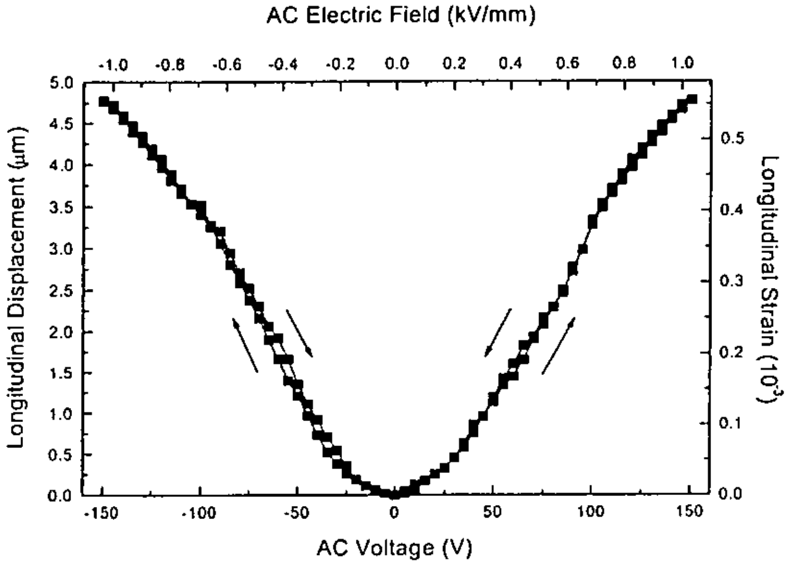

Figure 5.14 Longitudinal displacement and strain of the 0.9PMN-0.1PT actuator as a function of ac voltage and ac electric field, respectively.

When comparing the results of the polarization of the actuator in Section 5.6 and value of the strain value, the effective electrostrictive coefficient Q_{33} of the multilayer actuator can be obtained by the slope of Figure 5.15. The relation of the electrostrictive coefficient of the actuator and its polarization can be expressed as:

$$x_{33} = Q_{33}P^2 \tag{5.12}$$

where x_{33} is the longitudinal strain of the actuator and P is its electric polarization [Cross 1980, Nomura 1982]. The calculated electrostrictive coefficient Q_{33} is 0.203 x 10^{-2} m^4/C^2, while the value of it reported by Pan [Pan 1989] is about 0.21 x 10^{-2} m^4/C^2 for 0.9PMN-0.1PT bulk ceramic.

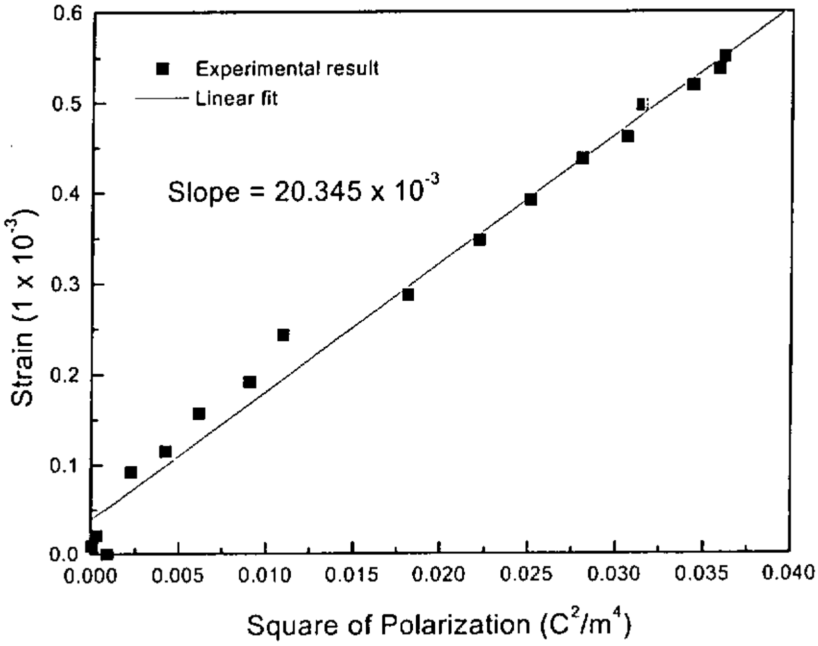

Figure 5.15 Longitudinal strain of the 0.9PMN-0.1PT actuator as a function of the square of its electric polarization.

As discussed in Section 1.3, the 0.9PMN-0.1PT would exhibit piezoelectric effect when a dc bias voltage is applied. This induced piezoelectric effect in the 0.9PMN-0.1PT multilayer actuator is investigated by measuring the displacement of the actuator driven by a dc bias voltage. As shown in Figure 5.16, the 0.9PMN-0.1PT actuator can generate a displacement of 7.3 μm under a dc bias voltage of 185 V. As the applied voltage decreases to zero, a small hysteresis of ~ 2 % is observed. When the driving voltage exceeds 100 V, the displacement tends to deviate from a linear relationship with voltage. Under a dc bias voltage of 145 V, the displacement of the actuator is 6.5 μm which is equivalent to a strain value of 0.75 x 10^{-3} at 1 kV/mm. This value of strain is comparable to that measured in bulk 0.9PMN-0.1PT ceramic reported by Uchino [Uchino 1986]. Hence, it shows no difference between the strain performance of the multilayer actuator and that of a bulk ceramic.

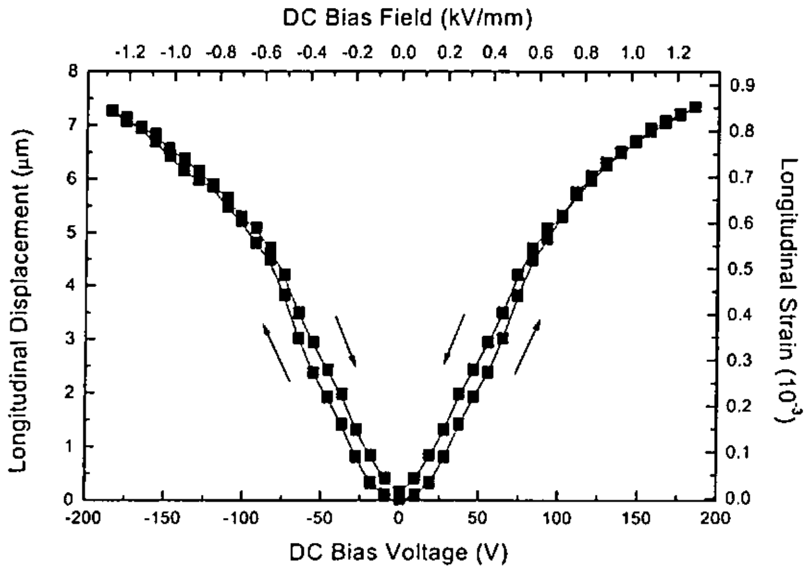

Figure 5.16 Longitudinal displacement and strain of the 0.9PMN-0.1PT actuator as a function of dc bias voltage and dc bias field, respectively.

The dc bias field induced strain is much greater than that of an ac electric field induced strain without dc biased. It is because polarizations induced by a dc bias field would give rise to a strong piezoelectric effect as discussed in Section 1.3 [Pan 1989]. This induced piezoelectric effect is found to be nonlinear w. r. t. the dc bias, and is much larger than that given by PZT materials. Figure 5.17 shows the effective piezoelectric coefficient d_{33} of this actuator as a function of the dc bias field. It is calculated by taking the derivative of the strain curve in Figure 5.16 w. r. t. the electric field ($d\varepsilon/dE$). The largest value of d_{33} is about 1265 pm/V when the dc-bias level rises to 0.38 kV/mm.

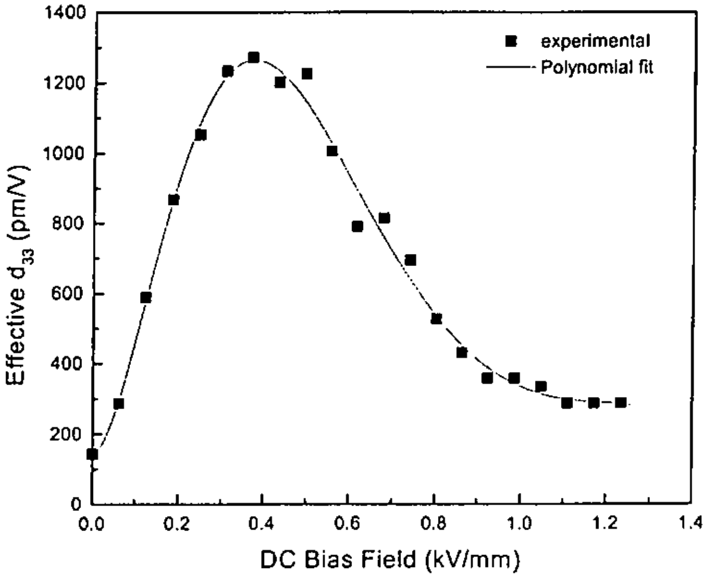

Figure 5.17 Effective piezoelectric coefficient d_{33} of the 0.9PMN-0.1PT actuator.

Figure 5.18 shows the transverse displacement and strain of the actuator as a function of the dc bias voltage and dc bias field at room temperature, respectively. The displacement is -2.1 μm under a dc bias voltage of 145 V which is equivalent to a strain value of -0.25 x 10^{-3} at 1 kV/mm. Effective piezoelectric d_{31} coefficient of the actuator can be estimated by taking the derivative of the strain to electric field curve. Figure 5.19 shows the estimated d_{31} as a function of the dc bias field. Its maximum value is –315 pm/V at a dc bias field of 0.43 kV/mm.

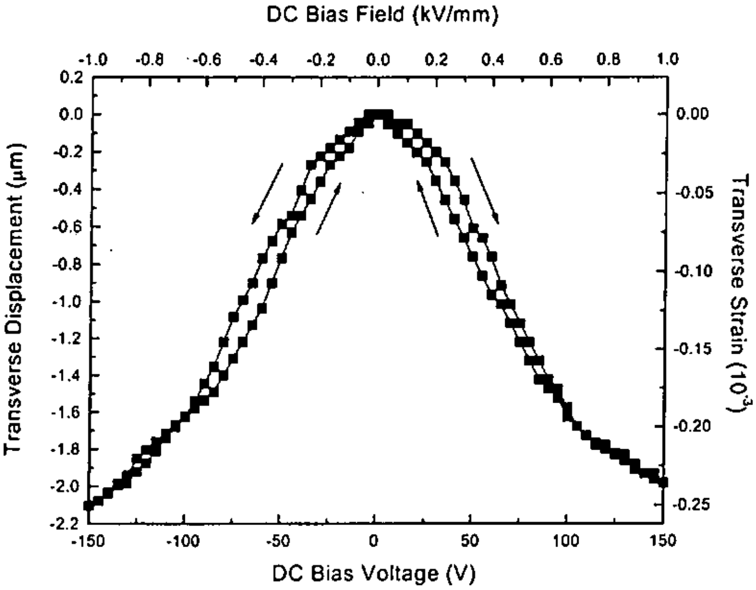

Figure 5.18 Transverse displacement and strain of the 0.9PMN-0.1PT actuator as a function of dc bias voltage and dc bias field, respectively.

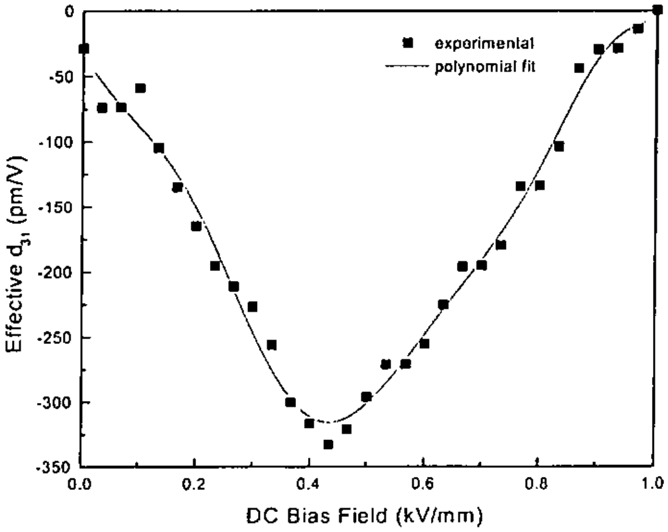

Figure 5.19 Effective piezoelectric coefficient d_{31} of the 0.9PMN-0.1PT actuator.

5.7.3 Operation Principle of the Vibrometer for Out-of-plane Displacement Measurements

Continuous displacements of the PZT and 0.9PMN-0.1PT actuators were measured by the Polytec Vibrometer (Controller: OFV 3001; Sensor Head: OFV 303). Figure 5.20 shows the heterodyne interferometry system of the Polytec Vibrometer sensor head. The HeNe laser is a monochromatic light source, with its polarization orientated at 45° to the horizontal plane. The Bragg cell is an optical modulator that frequency shifted the light beam by a frequency f_B (40 MHz) that is determined by the RF signal. This frequency shift f_B results in a modulation of the detected intensities with the RF carrier used. A polarizing beam splitter, BS1, splits the input beam into orthogonally polarized signal and reference beams. The Bragg frequency shifted signal beam, having passed through BS1 (Bragg cell) and BS2 and the focusing lens system L, hits the object. The special nature of BS2 ensures that the return beam is directed downward to BS3 [Polytec 1998].

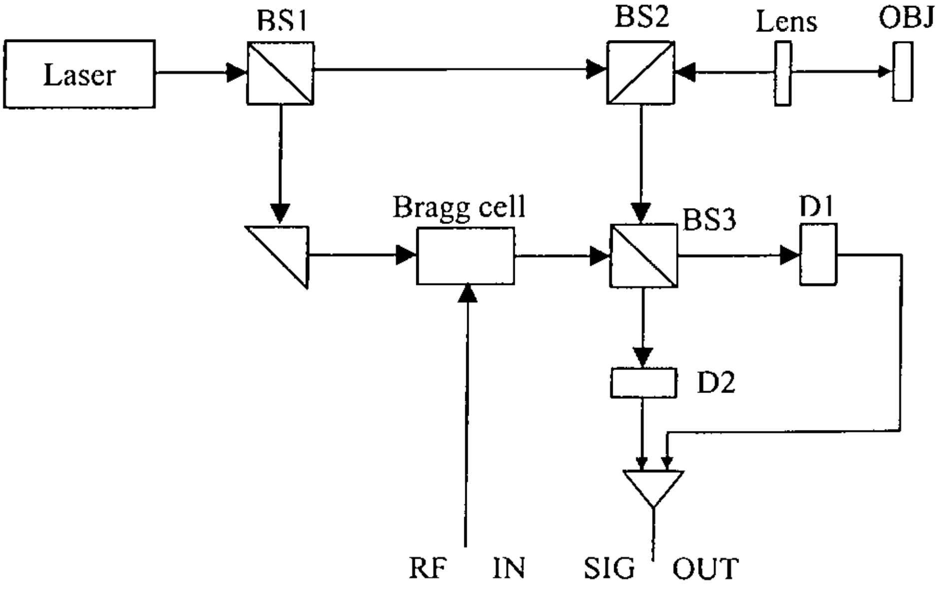

Figure 5.20 Schematic representation of the OFV-303 single point interferometer.

The polarized beam combines with the reference beam to generate the RF modulated interference signals. Both output signals from BS3 are converted to electrical signals by the photodiodes, D1 and D2. These signals vary in anti-phase manners and are combined using a differential pre-amplifier stage. The resulting output voltage is then given by:

$$V = K\cos[2\pi(f_B + 2v/\lambda)t] \tag{5.13}$$

where K denotes the conversion efficiency, its frequency results from an addition of Bragg frequency f_B and the Doppler frequency $f_D = 2v/\lambda$. Voltage V constitutes the output signal of the interferometer and is transmitted to the processor controller where RF signal processing is used to extract the velocity and displacement information. The displacements of the object can be calculated from the equation for a harmonic vibration:

$$V_{peak} = 2\pi f_V\, x_{peak} \tag{5.14}$$

$$x_{peak} = V_{peak} / 2\pi f_V \tag{5.15}$$

where f_V is the driving frequency, x_{peak} is the vibration amplitude; V_{peak} is the peak voltage value. V_{peak} can be obtained from the product of the output voltage and the velocity range of the controller.

The PZT and 0.9PMN-0.1PT multilayer actuators were connected to the NF electronic instruments HSA 4014 high-speed bipolar amplifier which amplified the voltage supplied by the Sony (Tektronix) AFG 310 function generator. One channel of the HP Infinium oscilloscope was connected to the output monitor of the amplifier and the other channel was connected to the vibrometer controller. Signal of vibration recorded by the sensor head was decoded as a voltage signal by the controller and was displayed on the oscilloscope. Laser beam from the sensor head should be directed perpendicularly to the measured surface.

The relation between the displacement of actuators and frequency has been worked out by measuring the displacement as a function of frequency with ac driving voltages of 10 V, 20 V and 30 V. Other than the displacement-frequency relations, response times of the actuators were estimated by observing the time delay between the applied electronic signal and the output displacement.

5.7.4 Results and Discussion

When driving the PZT multilayer actuator with an ac signal, the actuator must be biased at a level such that the applied ac field is unipolar [Tokin 1995]. Although the displacement level is biased, it would not affect the measured value cause the vibrometer would observe the ac vibration only. For all multilayer actuators, generally, it must be operated lower than one third of its resonant frequency. Above this frequency range, the actuator cannot follow such a fast response [Physik Instrumente 2001]. Therefore, the measurement frequency would be in the range of 100 Hz to 30 kHz. Figure 5.21 shows the displacement of the PZT multilayer actuator as a function of frequency. The result shows that displacement would not drop a lot below 1 kHz, after this value, displacement of the actuator drops significantly.

Figure 5.22 shows the displacements of the 0.9PMN-0.1PT multilayer actuator as a function of applied ac driving voltage under three different bias levels:

10 V (0.07 kV/mm), 55 V (0.38 kV/mm) and 100 V (0.69 kV/mm). With respect to Figure 5.17, maximum d_{33} of the 0.9PMN-0.1PT actuator is found at ~ 0.38 kV/mm. Above this value, it drops again. This can be revealed by observing the displacement in Figure 5.22; displacement under a dc bias voltage of 55 V (0.38 kV/mm) is the largest. It can generate a displacement of 2.6 μm under an ac driving voltage of 50 V.

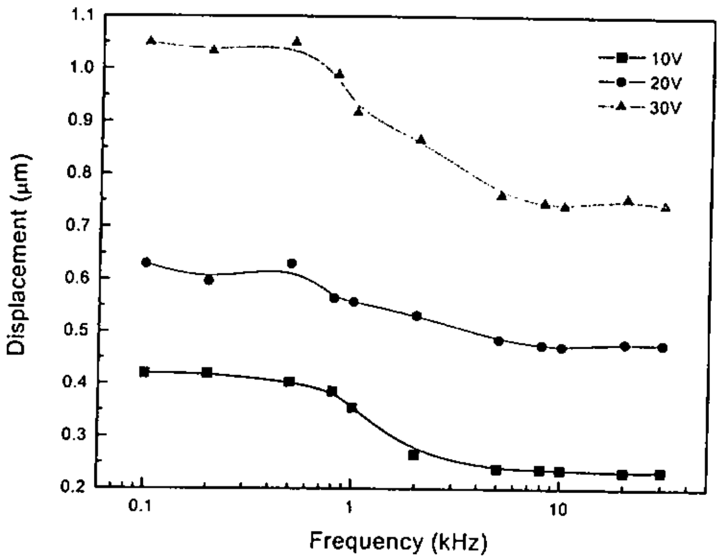

Figure 5.21 Displacement of the PZT multilayer actuator as a function of frequency.

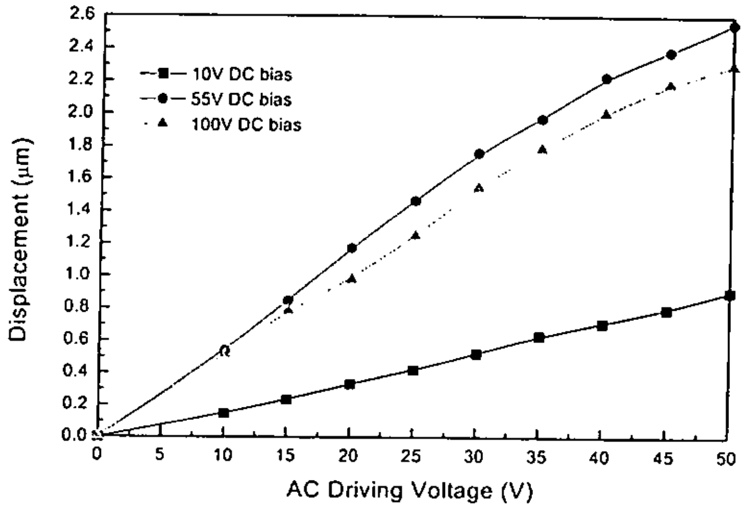

Figure 5.22 Displacement of the 0.9PMN-0.1PT multilayer actuator as a function of ac driving voltage under three different bias voltages: 10 V (square), 55 V (circle) and 100 V (up triangle).

Figure 5.23 shows the displacement-frequency relations of the 0.9PMN-0.1PT actuator. Before driving the actuator with an ac signal, a dc-biased voltage of 55 V is applied such that an instantaneous polarization was induced. Similar to the PZT multilayer actuator, the displacement drops significantly when the driving frequency is higher than 1 kHz.

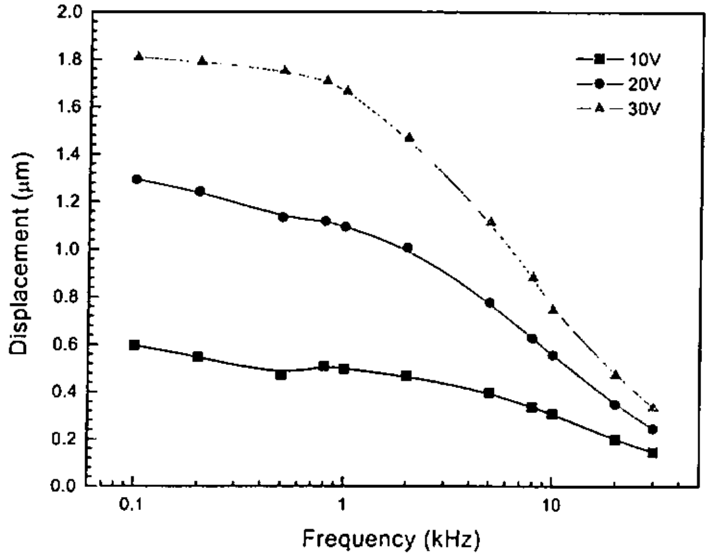

Figure 5.23 Displacement of the 0.9PMN-0.1PT multilayer actuator as a function of frequency.

Figures 5.24 and 5.25 show the time delay between the ac voltage at 1 kHz and the output displacement of the PZT and 0.9PMN-0.1PT multilayer actuators, respectively. The time delay of the first one is about 9 μs while the time delay of the second one is about 27 μs. The longer time delay of the 0.9PMN-0.1PT actuator may be due to its higher dielectric permittivity than that of the PZT actuator. Hence, when utilizing these two materials as actuators, time allowed for the actuator to respond should be taken into account.

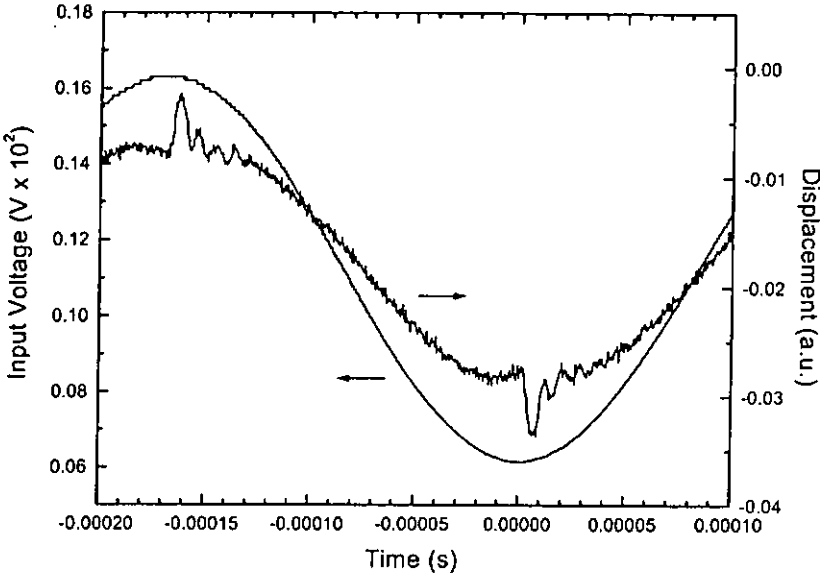

Figure 5.24 Time delay between the input voltage and the output displacement of the PZT multilayer actuator.

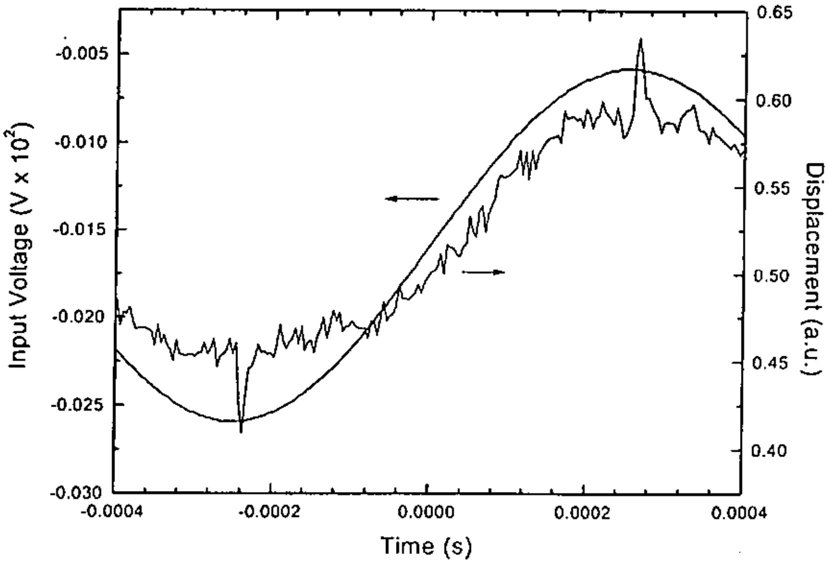

Figure 5.25 Time delay between the input voltage and the output displacement of the 0.9PMN-0.1PT multilayer actuator.

Chapter 6.

Multilayer Actuators for Wireclamp Applications

6.1 Introduction

Further to the detailed discussion on the fabrication and characterization of multilayer actuators, description and evaluation of using these actuators in wireclamp applications would be presented in this Chapter.

Descriptions about the wireclamp mechanism and installations of the two actuators into the metal parts of the wireclamp would be presented in the first part of this Chapter. It is difficult to use piezoelectric / electrostrictive actuator in the wireclamp application as it gives small displacement compared with other electromechanical devices (e.g. solenoid and voice coil). Hence, a mechanical amplifier is necessary for incorporating the actuator into this application.

The second part of this Chapter is the evaluation of the displacements of the two wireclamps by using the Fotonic sensor and the Polytec vibrometer to show the feasibility of using the piezoelectric / electrostrictive actuator in wireclamp applications.

6.2 Guidelines for Actuator Installation

Engineers should be aware of the guidelines for mechanical installation of multilayer actuators before mounting it into a mechanical system. Since the multilayer structure is composed of many fragile internal ceramic pieces, it must be handled with great care. Some points to be noted are discussed in the following paragraphs [Physik Instrumente 2001].

First, the actuator should only be stressed axially. Any tilt and shear forces applied onto the top piece must be avoided. Otherwise, cracks would occur in-between the interfaces of the ceramic layers and thus damage the device. (Figure 6.1)

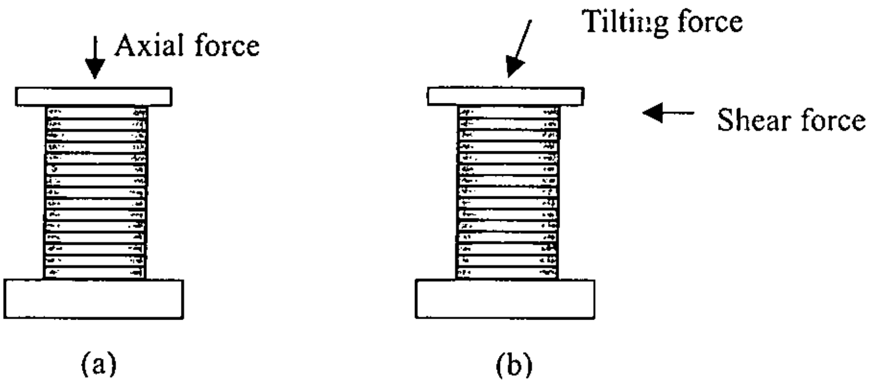

Figure 6.1 (a) Correct preloading force direction and (b) Incorrect preloading force direction.

Second, since the actuator is fabricated without casing, no precompression has been added onto the actuator prior to any applications. Therefore, it is sensitive to any pulling force and a preload is highly recommended.

Third, the actuator cannot be mounted rigidly at both ends. Such an assembly would lead to bending of the actuator and hence cause damage. It can be mounted rigidly at only one end and the other end can be attached to a movable surface. (Figure 6.2)

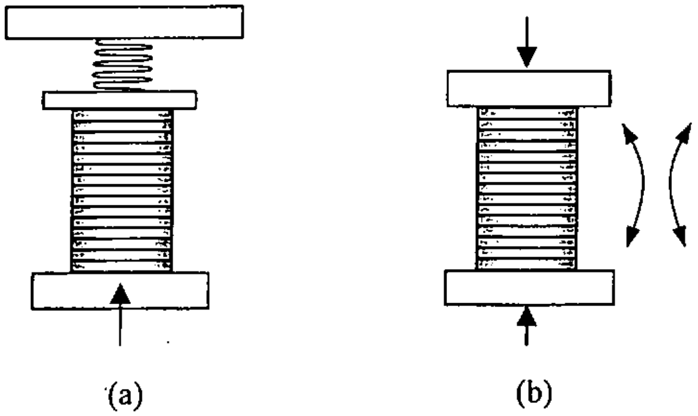

Figure 6.2 (a) Correct installation, one end is rigidly mounted and the other is flexible and (b) Incorrect installation, both ends are rigidly mounted.

Fourth, the surface between the mounting surface and the top or bottom surfaces of the actuator should be in parallel. Ball tip and spherical surfaces are recommended in order to prevent unparallel installation.

6.3 Description of the Wireclamp Structure

The wireclamp is composed of two main parts, one is the metal parts providing clamping motion; the other part is the piezoelectric / electrostrictive actuator for driving. Since most of the piezoelectric / electrostrictive actuators suffer from the problem of having small displacement, so the metal parts have to be designed as a mechanical amplifier such that the displacement of the actuator can be magnified to provide enough opening distance in the wireclamp.

Figure 6.3 shows the five major parts of the wireclamp metal body: 1) *clamping arms*; 2) *mechanical amplifier*; 3) *deformable back plate*; 4) *screws and nuts for preloading*; 5) *base*. Engineering drawings of the wireclamps for the PZT and the 0.9PMN-0.1PT multilayer actuators are given in Appendix B.1 and B.2, respectively. Descriptions of the five portions are given in Section 6.3.2 - 6.3.6.

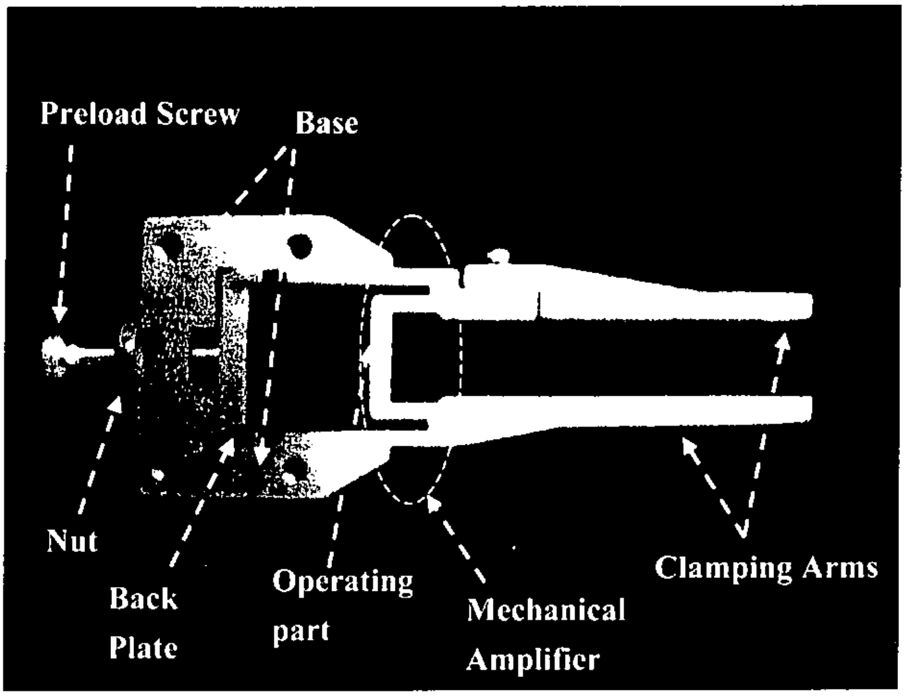

Figure 6.3 Photograph of the metal body of the wireclamp.

6.3.1 Material of the Wireclamp

Dimensions of the wireclamps are varied to fit the two actuators, and their structures are modified in some parts for demonstrating the wireclamp opening mechanism. The wireclamp is made of titanium alloy from Goodfellow (TI000460, 99.6 %, Annealed). Table 6.1 is a list of the material properties of the titanium

TI000460 [Matweb 2001, Goodfellow 2001].

Table 6.1 A list of the material properties of the titanium TI000460 [Matweb 2001].

Mechanical Properties	
Material Condition	Annealed
Material Condition (Tensile Strength) MPa	230-460
Material Condition (Yield Strength) MPa	140-250
Material Condition (Modulus of Elasticity) GPa [Goodfellow 2001]	105-110
Physical Properties	
Boiling Point (°C)	3287
Density @ 20 °C (g cm^{-3})	4.5
Melting Point (20 °C)	1660
Thermal Properties	
Linear Expansion Coefficient @ 0-100 °C ($x10^{-6}$ K^{-1})	8.9
Specific Heat @ 20 °C (J K^{-1} kg^{-1})	523
Thermal Conductivity, @ 0-100 °C (W m^{-1} K^{-1})	21.9

6.3.2 The Clamping Arms

For clamping aluminum / gold wires in ultrasonic wire bonding, a pair of movable arms is necessary. The aim of this wireclamp design is to demonstrate its opening ability; therefore, no clamping pieces are fitted for actual clamping of wires. The part connecting to the two clamping arms is the mechanical amplifier.

6.3.3 The Mechanical Amplifier

In order to provide enough opening displacement of the clamping arms, this mechanical amplifier plays a vital role in the utilization of piezoelectric / electrostrictive actuators in wireclamp applications. It comprises two narrow links for each clamping arm; one link connects the clamping arm and the base part of the main body, while the other link connects the clamping arm and the operating part. The surface of the operating part that contacts the driving element is of spherical shape with large radius in order to avoid unparallel installations as discussed in Section 6.2. When the driving element pushes the operating part, the two narrow links in each arm will push outward such that the two clamping arms are opened.

6.3.4 The Deformable Back Plate

When installing the actuator into the wireclamp, it would be placed between the mechanical amplifier and a back plate. Since the space for installing an actuator must be larger than the length of the actuator, then a preloading force has to be added onto the back plate to lock the actuator together with the whole metal body. In this case, the back plate should be able to deform so that energy can be transferred from the driving element to the opening arms. This deformable back plate is accomplished by wire-cutting a narrow groove at the back of the main metal body.

6.3.5 The Screw and Nut for Pre-loading

A screw would be responsible for providing a preloading force to lock the actuator to the metal body. This screw would pass through the end of the metal base and then pressing against the back plate to deform, then the actuator would be tightly clamped. However, an opposite reacting force from the back plate would push back the screw and loosening the clamping action. Hence, a nut should be used to lock the position of the screw w. r. t. the metal body so that the preload would not be weakened.

6.3.6 The Base

The base is the main body of the wireclamp that connects all the four parts described above. Four holes were drilled on the base so that the wireclamp can be fixed by screws onto a holder for measurements.

6.3.7 Installations

Prior to installing the PZT and 0.9PMN-0.1PT multilayer actuators into the metal body of the wireclamps, the surface of the back plate and the surface of the operating part that contacts the actuators should be polished. It can prevent any stress concentrated on the surface of the actuators due to the roughness of the metal surfaces. When loading the actuator into the space provided, the screw for preload should press onto the back plate such that the actuator was firmly mounted onto the metal body of the wireclamp. However, further preload is not desirable since it will push the actuator forward and open the clamping arm even without driving the actuator. When the preload screw is properly adjusted, the nut must lock the screw at once. Consequently, two wireclamps are fabricated, one is installed with the PZT actuator (PZT-clamp) and the other one is installed with the 0.9PMN-0.1PT actuator (PMNPT-clamp). Figure 6.4 shows the picture of these two wireclamps and Figure 6.5 shows the PMNPT-clamp mounted on a holder for measurements.

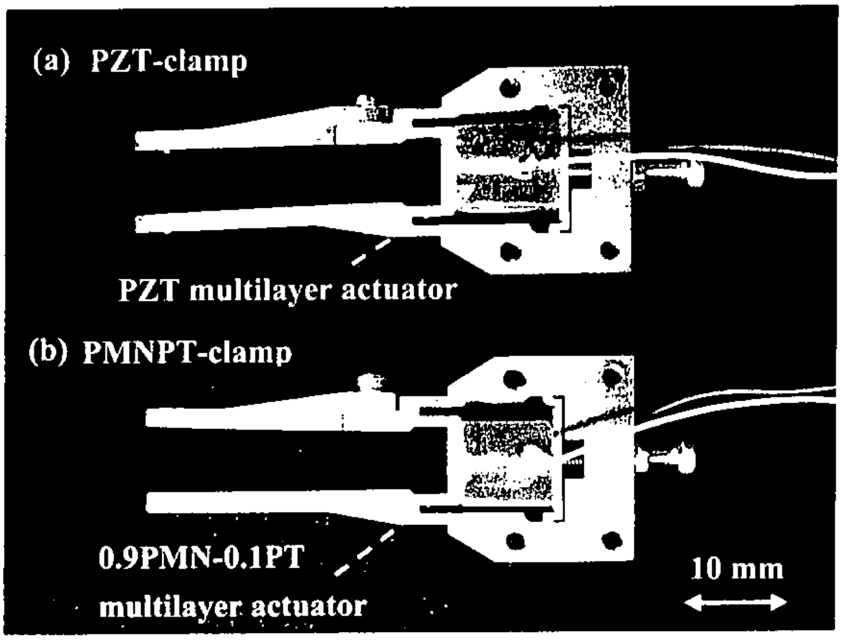

Figure 6.4 (a) The wireclamp installed with a PZT multilayer actuator is denoted as (PZT-clamp) and (b) the wireclamp installed with a 0.9PMN-0.1PT multilayer actuator is denoted as (PMNPT-clamp).

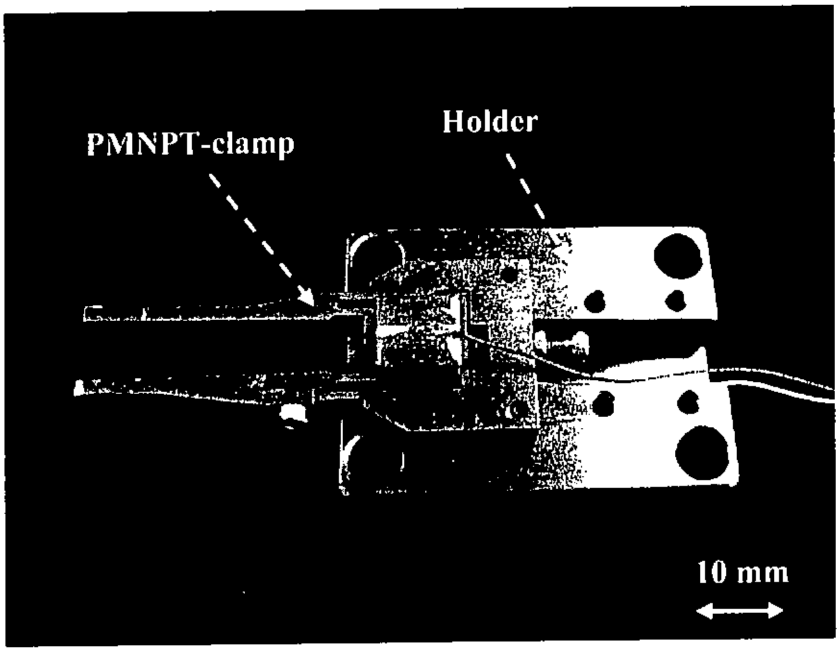

Figure 6.5 PMNPT-clamp mounted on a holder for measurement.

6.4 Opening Displacement Evaluations

When a voltage is applied to the actuator, the actuator elongates in the longitudinal direction. The operating part moves in the same direction as the actuator, as a result, the mechanical amplifier pushes outward so that the clamping arms are opened. This opening displacement of the PZT-clamp and PMNPT-clamp would be evaluated under dc field and ac field, respectively. The Fotonic sensor was used to measure the wireclamp displacement when the wireclamp was driven under a dc field, while the Polytec vibrometer was used to measure its displacement under an ac field.

When measuring the dc displacement of the wireclamp, the Fotonic sensor probe was placed in front of the end-point of the clamping arm. Figure 6.6 shows the position of the Fotonic sensor probe when measuring the dc displacement of the

PMNPT-clamp. It is a narrow gap between the sensor probe and the PMNPT-clamp.

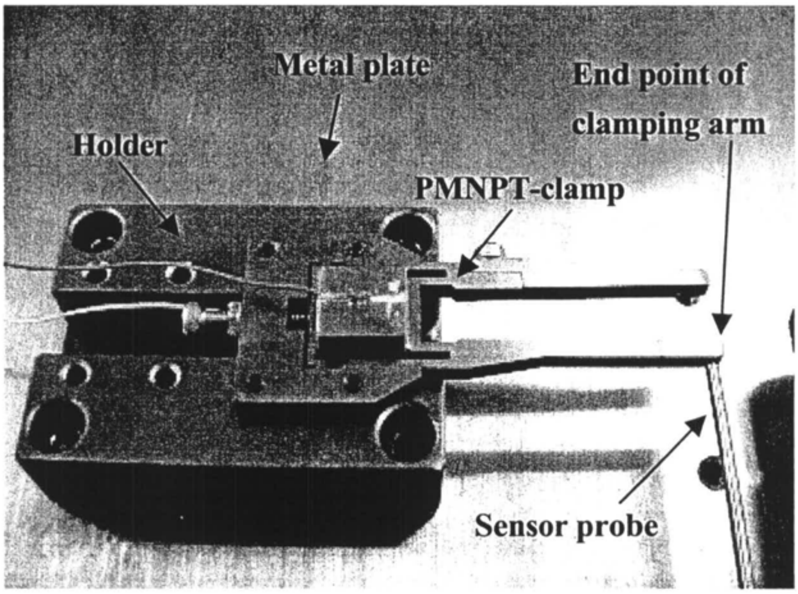

Figure 6.6 Photograph showing the position of the Fotonic sensor probe when measuring the dc displacement of the PMNPT-clamp.

The amplification factor of the wireclamps can be obtained by comparing the displacement generated in the actuators alone (longitudinal) and that of the wireclamps. Displacement of the wireclamp would be measured at different frequencies when the actuators were driven by an ac field. Both experiment require the actuator mounted on a holder where the holder is fixed onto a thick stainless steel plate (Figure 6.6).

The opening distance measured for the wireclamp is for one clamping arm only, it is assumed that the other clamping arm also generates the same displacement, since their structures are the same. Therefore, the total opening displacement can be calculated as two times that of the displacement of one clamping arm. (*2 x measured displacement of one arm*)

6.4.1 Displacement Under DC Voltage

Setup of the experiment is the same as that of measuring the displacement of an actuator described in Section 5.7.1. When driving the PZT-clamp, direction of the applied voltage should be the same as the polarization direction of the PZT multilayer actuator to avoid depoling the actuator. Figure 6.7 shows the displacement of the PZT-clamp and the longitudinal displacement of the PZT multilayer actuator under dc driving signals.

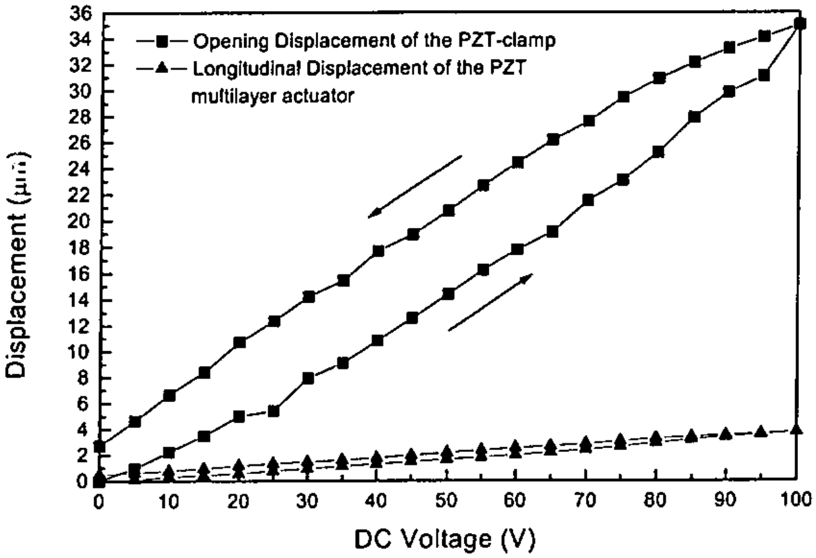

Figure 6.7 Displacement of the PZT-clamp and the longitudinal displacement of the PZT multilayer actuator under dc driving signals.

Similar to the PZT multilayer actuator, displacement hysteresis also occurs in the PZT-clamp. The percentage of displacement hysteresis of the PZT-clamp is about 9 %. Under 100 V, the PZT multilayer actuator can only generate a displacement of 3.8 μm, while the PZT-clamp can generate a displacement of 35 μm for two clamping arms. The amplification factor is about 9.2.

Figure 6.8 shows the displacement of the PMNPT-clamp and the longitudinal displacement of the 0.9PMN-0.1PT multilayer actuator under dc driving signals.

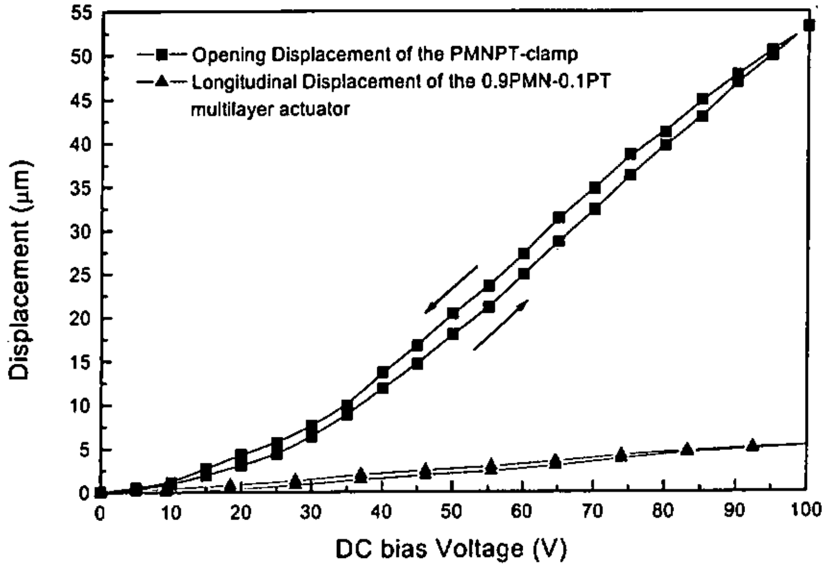

Figure 6.8 Displacement of the PMNPT-clamp and the longitudinal displacement of the 0.9PMN-0.1PT multilayer actuator under dc driving signals.

Under a dc voltage of 100 V, the PMNPT-clamp can generate a displacement of 53 μm while the 0.9PMN-0.1PT multilayer actuator can only generate 5.2 μm under the same driving voltage. The amplification factor is about 10.2. Due to the properties of 0.9PMN-0.1PT ceramic, the generated displacement is not linearly proportional to the applied voltage and no displacement hysteresis can be observed because the 0.9PMN-0.1PT ceramic has no remanent polarization near room temperature.

6.4.2 Discussion

The amplification factors of the two wireclamps are roughly the same, since their structure and dimensions are the same, except for the dimensions of the actuators. However, the PZT-clamp has displacement hysteresis while the PMNPT-clamp has not. The clamping arms open due to the actuator expands and they should return to the original position when the voltage applied to the actuator is cut off. If hysteresis occurs, the clamping arms cannot return to its original position, and hence cannot clamp wires. To compensate for the hysteresis in the PZT-clamp, several methods have been proposed in the literature. These include feedback of the displacement of piezoelectric devices [Okazaki 1990], bridge circuit with additional resistors or capacitors [Dosch 1992], supplied charge control by driving a current source [Newcomb 1982], insertion of an additional capacitance in series [Kaizuki 1988] and combining induced charge feedback with inverse transfer function compensation [Furutani 1998]. All these methods require additional circuitry which increases the manufacturing cost.

6.4.3 Displacement Under AC Voltage

Setup of the experiment is the same as that of measuring the displacement of an actuator under ac voltage described in Section 5.7.3. When driving the PZT-clamp, a dc bias voltage is required to ensure a positive driving voltage. Figures 6.9 and 6.10 show the displacement of the PZT-clamp and PMNPT-clamp as a function of ac driving voltage at 1 kHz, respectively. As shown in Figure 6.9, the opening displacement of the PZT-clamp is linearly proportional to the ac driving voltage. It gives a 19 μm displacement under an ac voltage of 50 V at 1 kHz. For driving the PMNPT-clamp, a dc bias of 55V (0.38 kV/mm) is given. Figure 6.10 shows that the PMNPT-clamp can generate a displacement of about 35 μm under an ac voltage of 50 V at 1 kHz. It displaces nonlinearly w. r. t. the applied voltage.

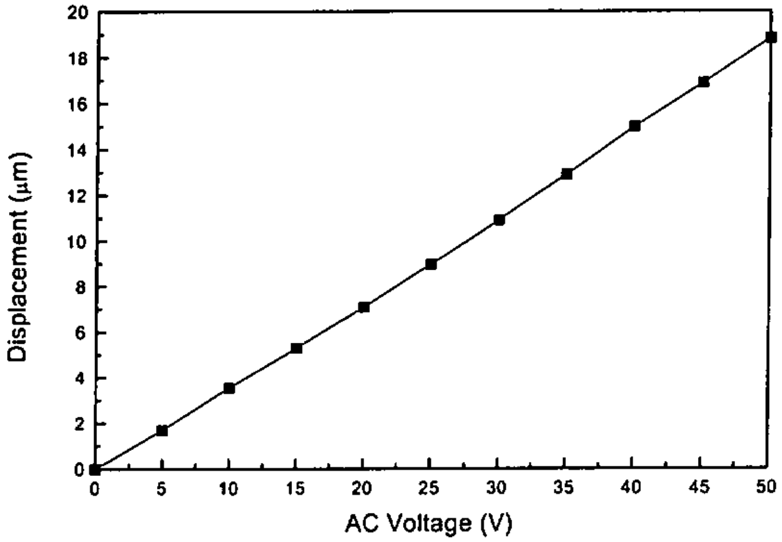

Figure 6.9 Displacement of the PZT-clamp as a function of ac driving voltage at 1 kHz.

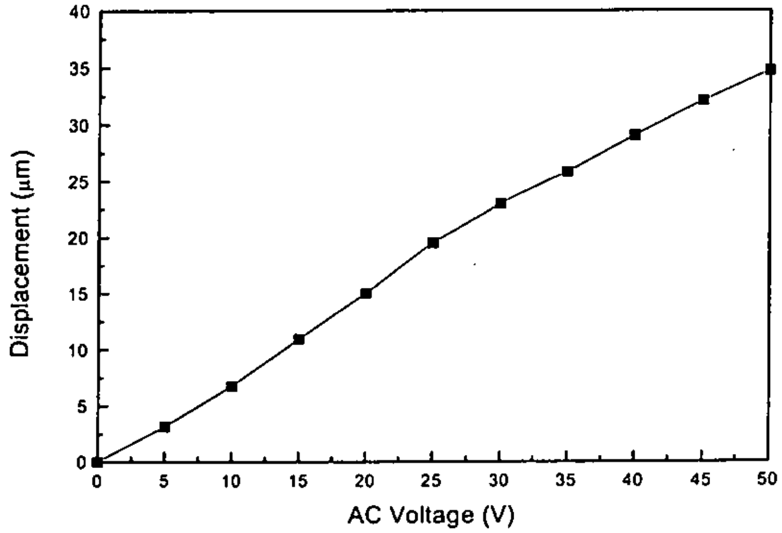

Figure 6.10 Displacement of the PMNPT-clamp as a function of ac driving voltage at 1 kHz with a dc bias voltage of 55V.

6.4.4 Displacement–Frequency Relationship

Figures 6.11 and 6.12 show the opening displacements of the PZT-clamp and PMNPT-clamp as a function of frequency, respectively. Below 1 kHz, the opening displacements are almost the same, but over 1 kHz, it drops significantly.

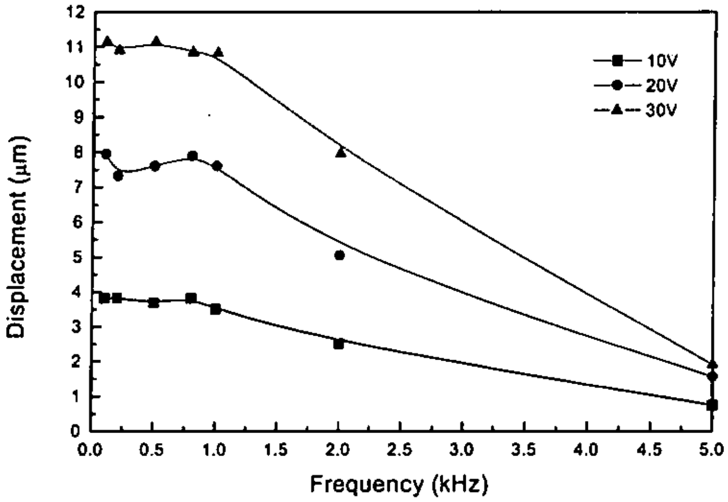

Figure 6.11 Displacement of the PZT-clamp as a function of driving frequency.

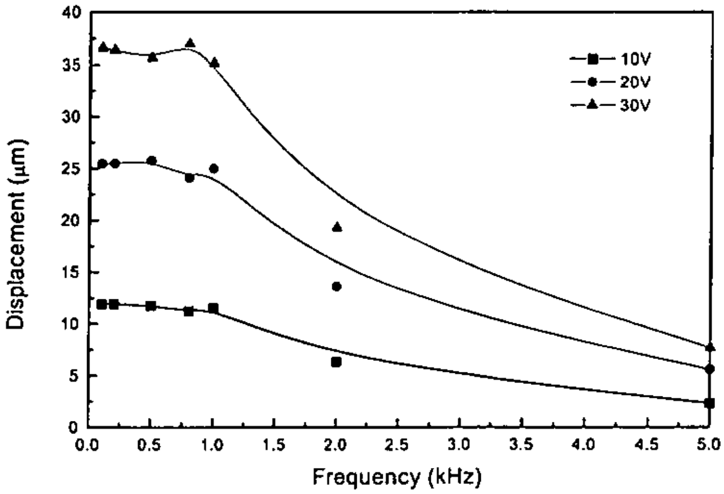

Figure 6.12 Displacement of the PMNPT-clamp as a function of driving frequency.

6.5 Response Time

By observing the time difference between the input voltage and the measured signal, response time of the wireclamp can be obtained. It can be conducted by feeding the "displacement channel" of the Polytec OFV-3001 laser vibrometer controller to one of the HP Infinium oscilloscope channel, and the other channel of the oscilloscope was connected to the "output monitoring" of the NF electronic instruments HSA 4014 high speed bipolar amplifier which drove the wireclamp. Consequently, the two signals can be saved into an electronic file by the oscilloscope. Figures 6.13 and 6.14 show the time differences between the input voltage and the measured signal of the PZT-clamp and PMNPT-clamp, respectively. The response time of the PZT-clamp is about 40 μs while the response time of the PMNPT-clamp is about 110 μs.

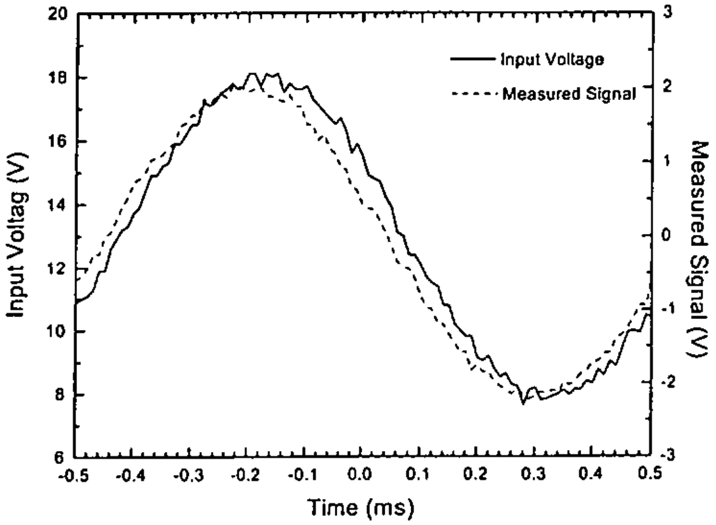

Figure 6.13 Time difference between the input voltage and the measured signal of the PZT-clamp.

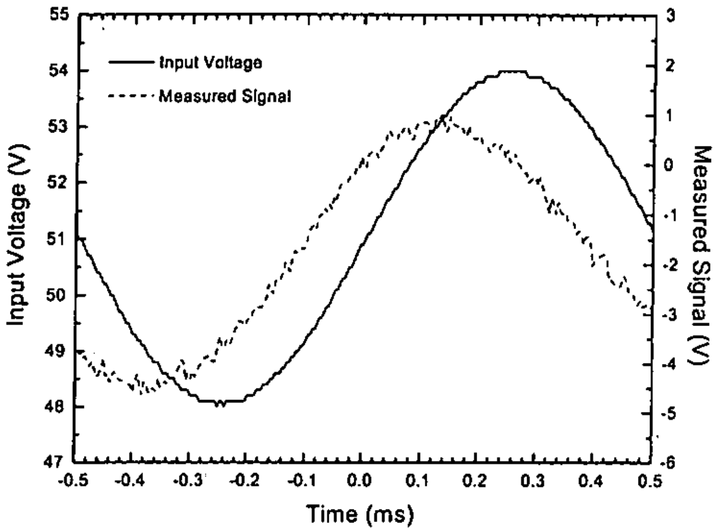

Figure 6.14 Time difference between the input voltage and the measured signal of the PMNPT-clamp.

6.6 Discussion

Although the opening displacements of the two wireclamps are not sufficient for clamping a 2-mil Al wire (~100 μm with adequate clearance), the PMNPT-clamp can be used to clamp a 1.25-mil Al wire (~55 mm with adequate clearance) due to its high piezoelectric effect induced by dc bias voltage. Furthermore, the opening displacement of the two clamps can be improved by two suggestions.

One way is to increase the amplification factor. Amplification factor can be regarded as the ratio of the width of operating part and the length of clamping arms. This ratio can be increased by reducing the width of the operating part or by increasing the length of the clamping arms. For reducing the width of the operating part, an actuator of smaller cross-sectional area should be used.

Performance of an actuator is determined by the material properties and structures of the multilayer actuators. Therefore, the actuator performance can be improved by means of either selecting a piezoelectric material with higher d_{33} or by modifying the multilayer structures. The former can be achieved by modifying the ceramic compositions or by doping with some elements. The later can be achieved by fabricating the multilayer actuator with thinner internal layers or with larger number of layers.

When considering the response time of the wireclamps discussed in the previous Section, it can be seen that the response time for the PMNPT-clamp is much greater than that of the PZT-clamp. This can be explained by considering the RC constants of the two actuators. For the 0.9PMN-0.1PT actuator, its RC constant is about 1.236×10^{-5}, while the RC constant of the PZT actuator is only 2.068×10^{-6}. This is because the dielectric permittivity of 0.9PMN-0.1PT ceramic is much greater than that of PZT ceramic, and hence the capacitance of the 0.9PMN-0.1PT multilayer actuator is larger. This explains why the response time of the PZT-clamp is faster than the PMNPT-clamp.

Chapter 7.
Conclusions and Future Work

7.1 Conclusions

In this thesis, multilayer actuators and their applications in wireclamp application for ultrasonic wire bonders have been studied. The following work have been carried out:

1. Two ceramic materials, PZT and 0.9PMN-0.1PT were used to fabricate multilayer actuators. For PZT ceramics, PKI-552 was chosen because of its large piezoelectric coefficient. Its fabricating process was presented from dry pressing to poling and aging. For 0.9PMN-0.1PT ceramics fabrications, the main problem was the pyrochlore phase formation. Two methods were used to solve this problem. One was by fabricating the ceramics with columbite precursor method and the other was by doping excess magnesium oxide (MgO) and lead oxide (PbO). In the second method, three compositions were tested to find out the one that could achieve optimum properties. They were:
    a. 0.9PMN-0.1PT with 1wt% excess of MgO
    b. 0.9PMN-0.1PT with 1wt% excess of MgO and 1wt% excess of PbO
    c. 0.9PMN-0.1PT with 1wt% excess of MgO and 2wt% excess of PbO

2. Ceramics fabricated by various fabricating conditions were characterized.

Densities of PZT and 0.9PMN-0.1PT ceramics were measured by the Archimedes' principle. Their ferroelectric hysteresis loops were observed by the Sawyer Tower bridge, their elastic properties were found by the ultrasonic immersion method. For PZT, its properties such as the electromechanical coupling factors: k_p, k_t, mechanical Q_m factor, capacitance and loss tangent were evaluated by the HP 4194A impedance / gain phase analyzer. Its piezoelectric properties were also found. For 0.9PMN-0.1PT, its single-phase purity was measured by X-ray diffraction and its grain size was observed by the scanning electron microscope. Dielectric permittivities of 0.9PMN-0.1PT ceramics were calculated from the capacitance measurements. Finally, their electrostrictive properties were measured by the LVDT. The 0.9PMN-0.1PT ceramic with 1 wt% excess of MgO and 1 wt% excess of PbO which was sintered at 1250 °C showed the largest value of polarizations, dielectric permittivity and strain response. Therefore, this condition was selected for multilayer actuator fabrications.

3. PZT and 0.9PMN-0.1PT multilayer actuators were fabricated based on the cofiring technology. The ceramics were sintered together with internal electrodes. The green ceramic films for cofiring were prepared by roll casting. Ceramic films were painted with platinum electrode and were stacked up and hot-pressed to form a green ceramic block. During the binder burnout process, if the binder is burnt out and is expelled rapidly, the sample will be ruined. Two methods were tried to modify the binder burnout process, one was by using thermogravimetric analysis (TGA) to measure the binder decomposition profile and then adjust the burnout profile accordingly. The other was performing the binder burnout process by sandwiching the sample in-between two brass plates. During sintering, alumina

crucible covers were used to apply pressure onto the ceramic multilayers in order to eliminate the delaminations due to shrinkage at high temperatures. After binder burnout and sintering, a multilayer actuator was formed. The 0.9PMN-0.1PT multilayer actuator can be used after connecting the external wires and applying coating resin, but the PZT multilayer actuator needs to be poled at an electric field of 2 kV/mm and at 130 °C before use.

4. In multilayer actuator characterizations, SEM micrographs were taken to detect any defects existing in the actuators and the effective densities of the actuators were measured by the Archimedes' principle. Resonance modes of the PZT actuator were observed by the HP 4194A impedance / gain phase analyzer. Accordingly, vibrational mode frequencies (f_r, f_a), capacitance and loss tangent ($tan\delta$), electromechanical coupling factor (k_{33}) and effective mechanical Q-factor (Q_m) were measured. For the 0.9PMN-0.1PT actuator, its dielectric spectrum at different temperatures was measured by placing the sample in the ESPEC SU-240 temperature chamber. Polarization of the 0.9PMN-0.1PT multilayer actuator was measured by the aixACT TF Analyzer 2000 system. The displacement of these actuators under either ac or dc signal was measured by the Polytec OFV 3001 vibrometer and the MTI-2000 Fotonic fiber-optic sensor, respectively. When the two actuators were driven by a dc voltage of 100 V, the PZT actuator could generate a longitudinal displacement of 3.8 μm, while the 0.9PMN-0.1PT actuator could generate a longitudinal displacement of 5.2 μm. The maximum longitudinal piezoelectric coefficient d_{33} of the 0.9PMN-0.1PT actuator is about 1265 pm/V under a dc bias field of 0.38 kV/mm. Other than the longitudinal strain response, their transverse displacements were also characterized. Their

response times were measured by calculating the time difference between the input voltage and the signal measured by the outplane vibrometer. The time difference of the PZT actuator is about 9 μs while the time difference of 0.9PMN-0.1PT actuator is about 27 μs when they are driven at 1 kHz. This is presumably due to the high dielectric permittivity of the 0.9PMN-0.1PT ceramic.

5. Based on an existing wireclamp design, two wireclamps were fabricated. Descriptions of the wireclamp mechanism and installations of the two actuators into the metal parts of the wireclamp were presented. With the design of a mechanical amplifier, displacements generated from the actuators can be magnified. Displacements of the wireclamps under dc and ac driving signals were evaluated by using the Fotonic sensor and the vibrometer, respectively to show the feasibility of applying piezoelectric / electrostrictive actuator in wireclamp applications. For the displacement measurement under dc driving signal, the PZT-clamp can generate a displacement of 35 μm and the PMNPT-clamp can generate a displacement of 53 μm. The response times are 40 μs for the PZT-clamp and 110 μs for the PMNPT-clamp.

7.2 Future Work

Although there is an extensive study of the multilayer technology presented in this work, there are some areas for further study. One is the improvement of the fabrication technique. The thickness of each layer in the two multilayer actuators is about 145 μm, if it can be reduced to 100 μm or lower, then more ceramic sheets can be inserted without enlarging the overall length of the actuators. As a result, when subjected to the same voltage, the displacement generated can be increased by 50 % or more. The second suggested work is to study the hysteresis behavior of the PZT actuators. Hysteresis is the main difficulty when using PZT actuator in wireclamp applications. Due to this reason, a feedback system or a quick charge-discharge circuit can be used to eliminate this effect.

In order to use these actuators in wireclamp applications, a lot of areas need to be further researched and the design of the wireclamp needs to be improved. This can be achieved by changing the length of the clamping arms or by designing a new mechanical amplifier system. Finite element analysis (FEA) can also be used to simulate the opening motions of the wireclamp which can provide further design information to modify the wireclamp structure.

Other than designing the wireclamp structure, other wire-clamping ability also needs to be further studied. When two clamping plates are installed at the end of the clamping arms, wires can be clamped when the clamping arms open and close. If the clamping force is too large, the wire will deform. If a small gap is left between the two plates, wires cannot be clamped. This clamping force can be adjusted by tuning the preloading force applied by the screw at the back of the wireclamp.

Appendix

A Patents of Wireclamp Designs in the Literature

A.1 Wireclamp Designs in Patents Nos. US5323948, US5388751 and US5435477

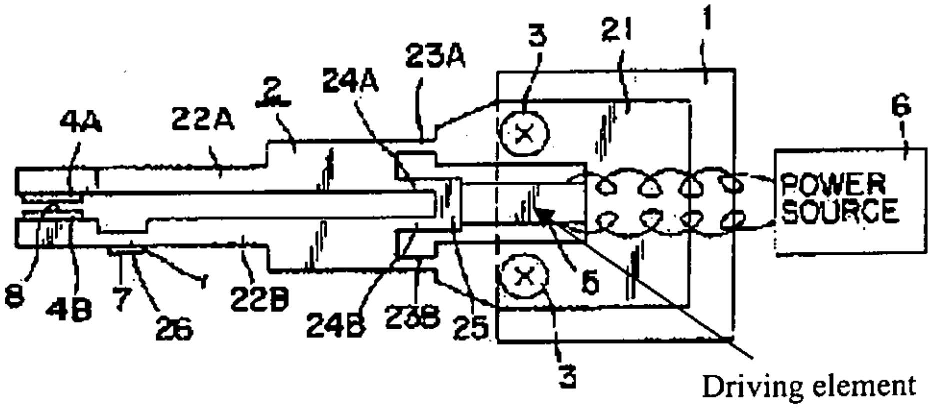

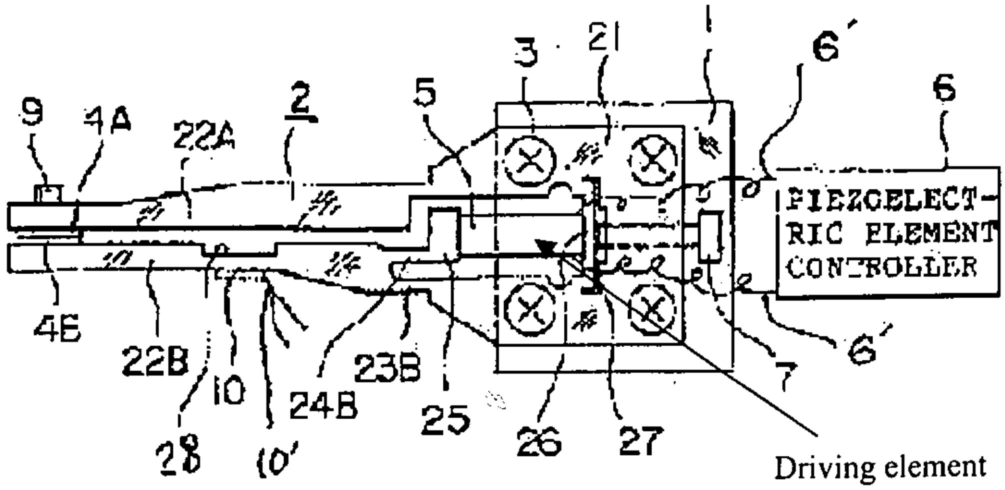

A.2 Wireclamp Design in Patent No. US5746422

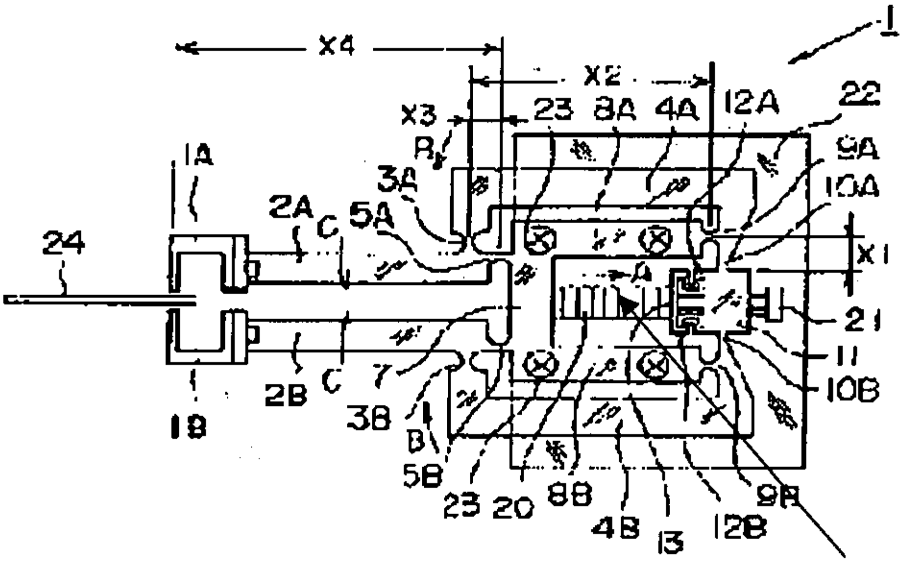

Driving element

A.3 Wireclamp Design in Patent No. US5314175

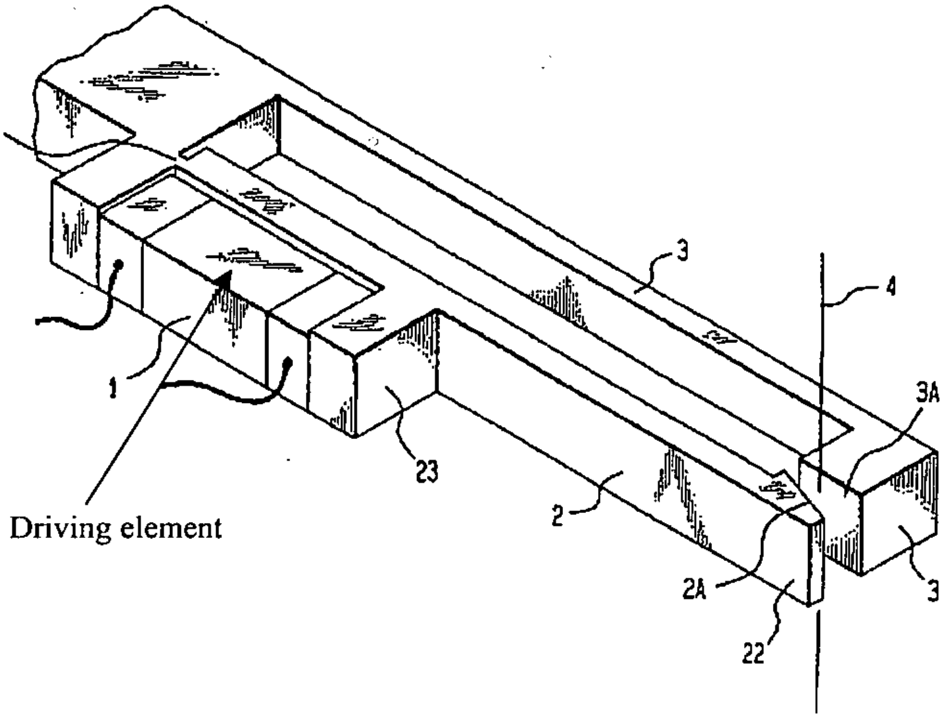

Driving element

A.4 Wireclamp Design in Patent No. JP57159034

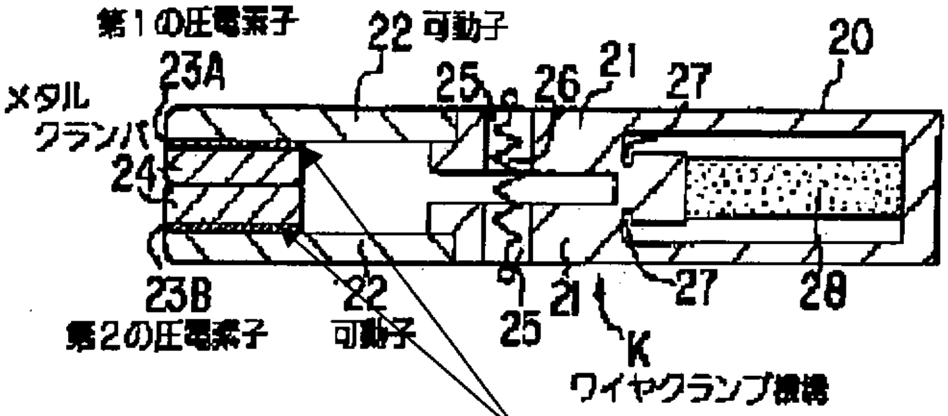

Driving elements

A.5 Wireclamp Design in Patent No. JP10242196

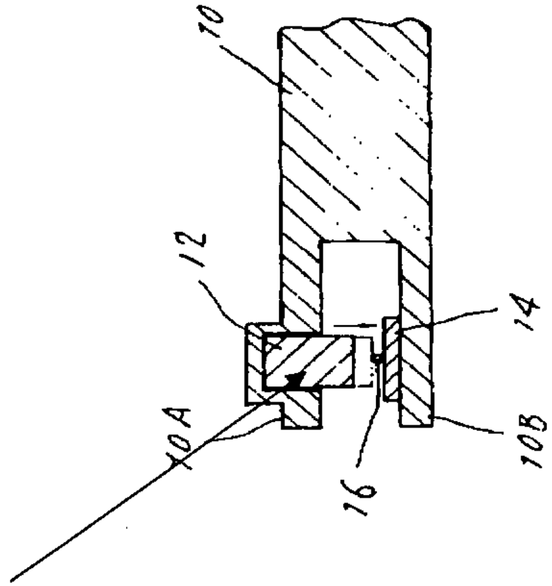

Driving element

A.6 Wireclamp Design in Patent No. JP09051012

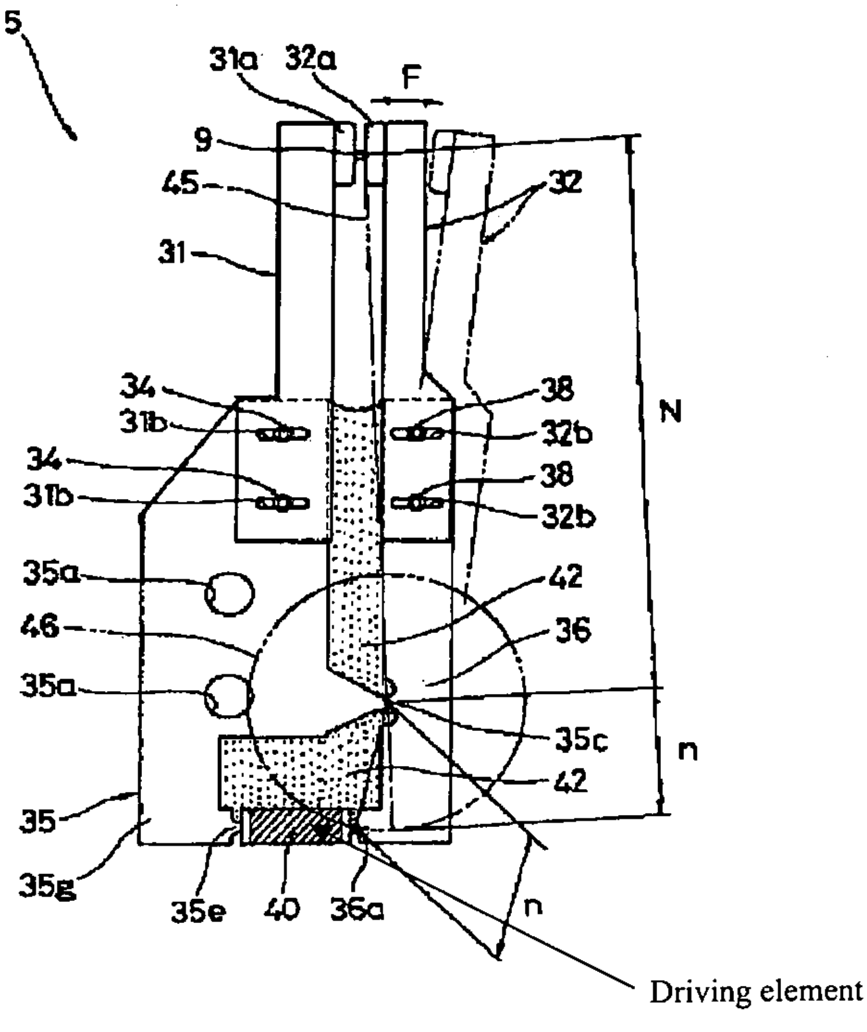

A.7 Wireclamp Design in Patent No. JP09051013

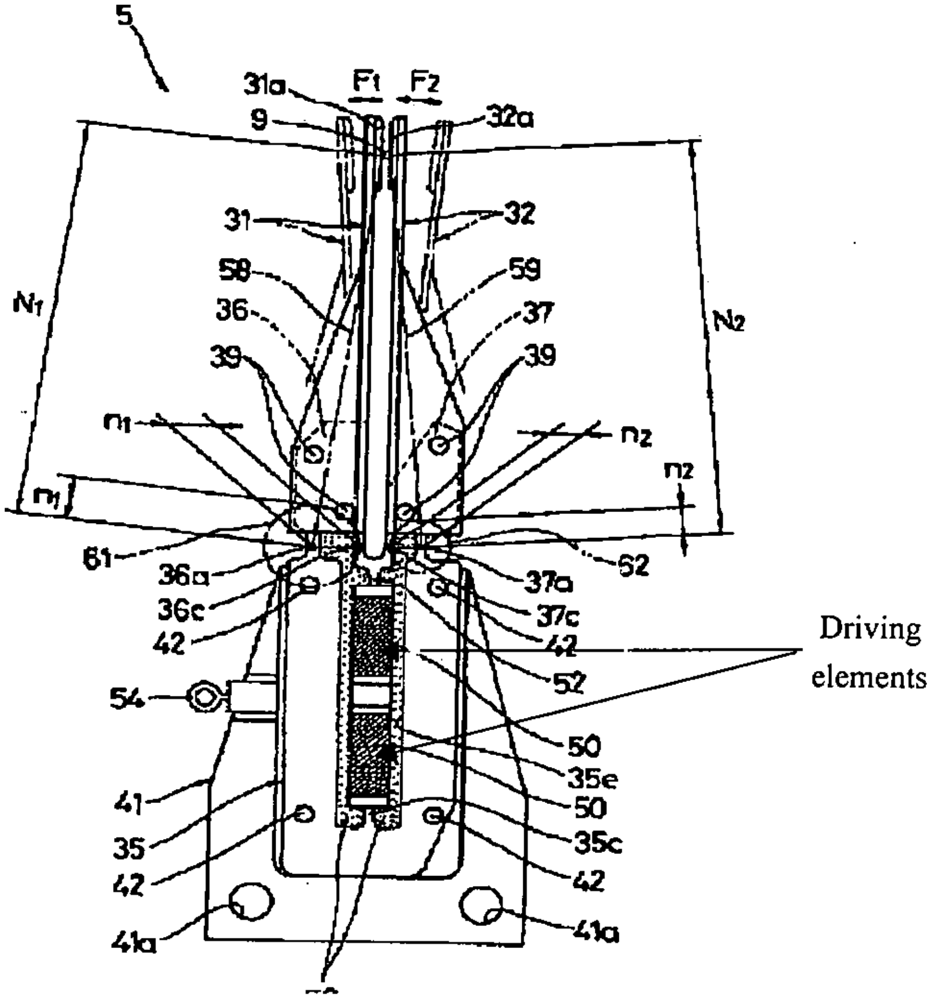

B Engineering Drawings of the Wireclamps

B.1 Engineering Drawing of the PZT-clamp

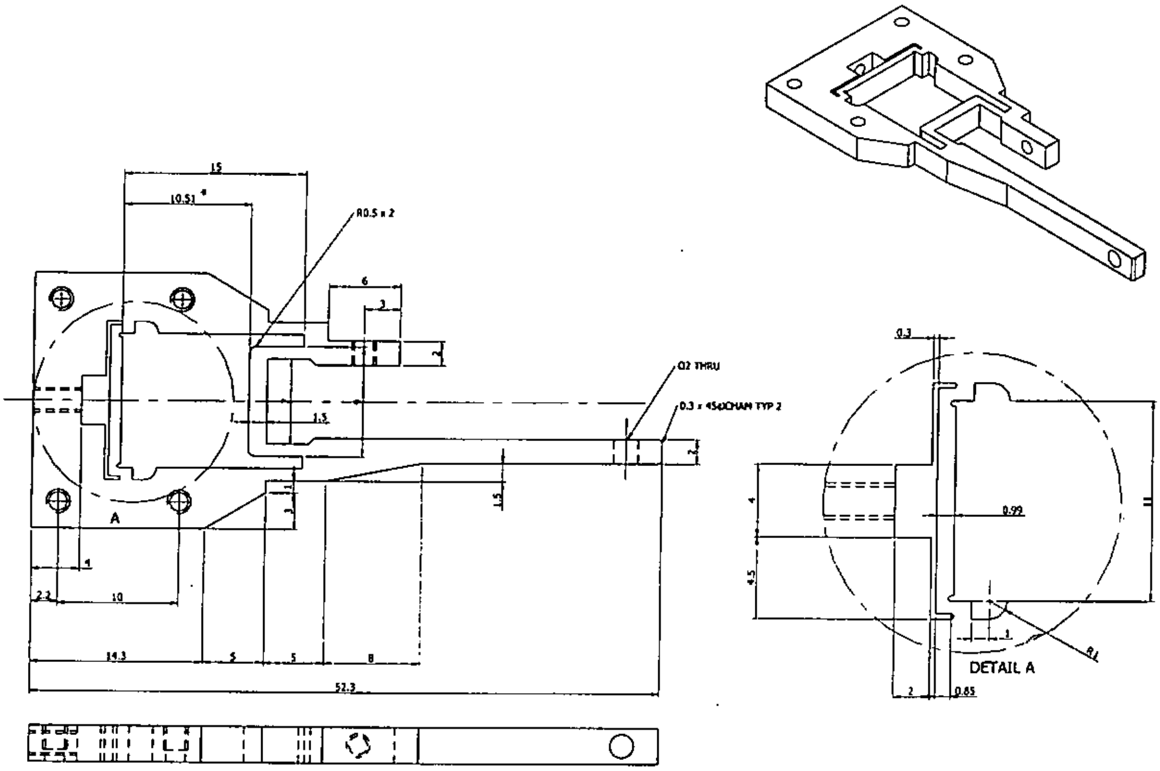

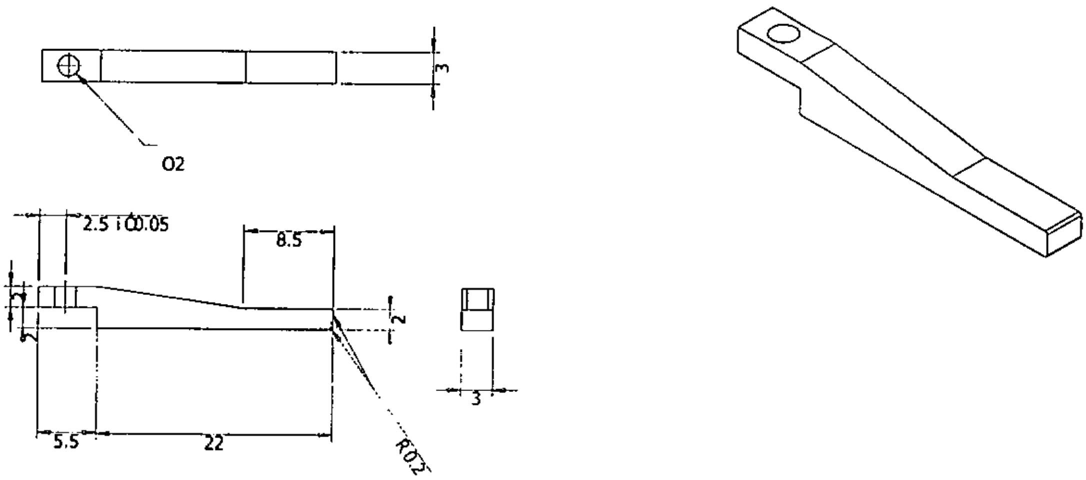

* Not in scale

B.2 Engineering Drawing of the PMNPT-clamp

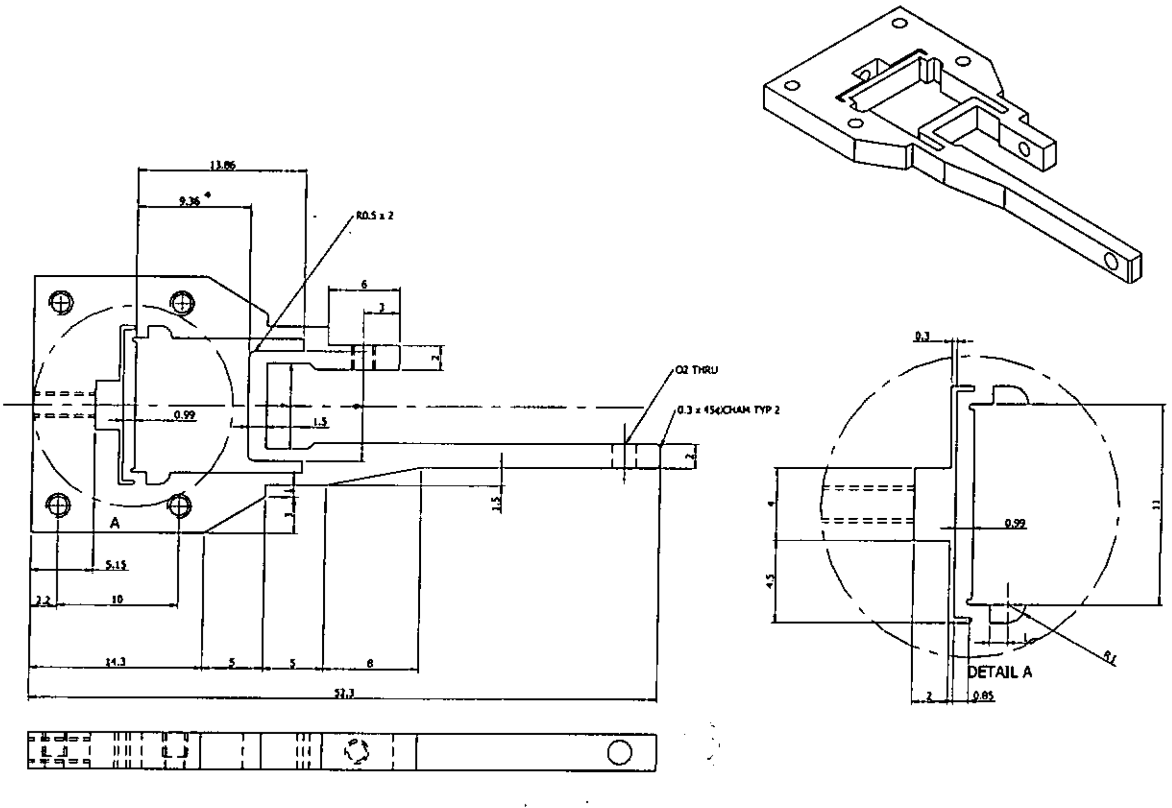

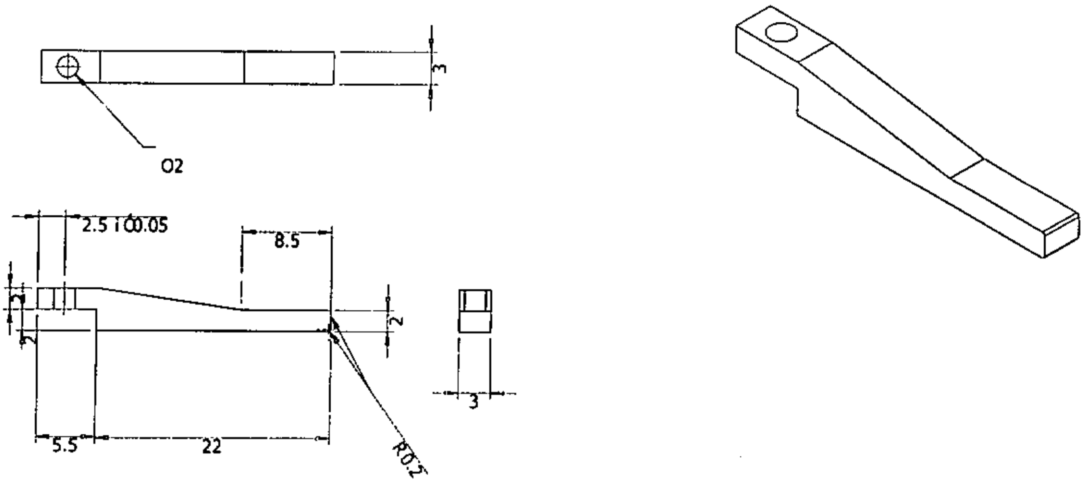

* Not in scale

References

Aburatani, H., Uchino, K., Fuda, A. F. Y., "Destruction Mechanism and Destruction Detection Technique for Multilayer Ceramic Actuators". *Ferroelectrics, Proc. of IEEE Symp.*, Vol. 1, pp.750-752 (1995).

"TF ANALYZER 2000 FE-Module (HV) Instruction Manual". *aix-ACCT*, Germany (2000)

Akihiro, Y., Yasuo, I., Nobuya, M., Yutaka, M., "Wire Clamping Device and Wire Clamping Method". *U.S. Patent*, No. 5314175 (1994)

"An American National Standard: IEEE Standard on Piezoelectricity". *ANSI/IEEE Std. 176-1987*, The Institute of Electrical and Electronics Engineers, Inc., pp. 227-280 (1988)

"ASTM Std. D 150-95: Standard Test Method for AC Loss Characteristics and Permittivity (Dielectric Constant) of Solid Electrical Insulation". *Annual Book of ASTM Standards*, Vol. 10.01, pp. 26-44 (1999)Chai, H. D., "Electromechanical Motion Devices". *Prentice Hall*, New Jersey (1998)

Bechou, L., Mejdi, S., Ousten, Y. and Danto, Y., "Non-destructive Detection and Localization of Defects in Multilayer Ceramic Chip Capacitors using Electromechanical Resonances". *Quality and Reliability Engineering International*, Vol. 12, pp.43-53 (1996)

Bray, D. E. and Mcbride, D., "Nondestructive testing techniques". R. D. Stewart, Series Editor, *Wiley Series in New Dimensions in Engineering*, Wiley and Sons, Chapter 6 (1992)

Bridger, K., Jones, L., Poppe, F., Brown, S., Winzer, S., "High-Force, Cofired Multilayer Actuators". *Proc. of SPIE- The International Society for Optical Engineering*, Vol. 2721, 27-29 February 1996, San Diego, California, pp.341-352 (1996)

Chen, D. R., Zhu, M. G., Zhang, W. Z., Li, G. R., "Preparation and Characterization of PBNN Multilayer Piezoelectric Actuator". *Proceedings of (ISE 9), 9th International Symposium on Electrets*, 25-30 Sept. 1996, pp.1061-1066 (1996)

Chen, J., Harmer, M. P., "Microstructure and Dielectric Properties of Lead Magnesium Niobate-Pyrochlore Diphasic Mixtures". *Journal of the American Ceramic Society*, Vol. 73 [1], pp.68-73 (1990)

Choy, C. L., "Elastic Moduli of Polymer Liquid Crystals". *Mechanical and Thermophysical Properties of Polymer Liquid Crystals*, Brostow, W., Ed., Chapman & Hall, London, Chapter 14 (1998)

Cross, L. E., Jang, S. J. and Newnham, R. E., "Large Electrostrictive Effects In Relaxor Ferroelectrics". *Ferroelectrics*, Vol. 23, pp.187-192 (1980)

Damjanovic, D., "Ferroelectric, dielectric and piezoelectric properties of ferroelectric thin films and ceramics". *Rep. Prog. Phys.*, IOP Publishing Ltd., UK, Vol. 61, pp.1267-1324 (1998)

Dogan, A., Fernandez, J. F., Uchino, K. and Newnham, R. E., "The "Cymbal" Electromechanical Actuator". *ISAF '96, Proc. of the 10th IEEE International Symposium on Appl. of Ferro.*, Vol. 1, pp.213-216 (1996)

Dosch, J. J. et al., "A Self-Sensing Piezoelectric Actuator for Collocated Control". *J. Intell. Mater. Syst. Struct.*, Vol. 3, No. 1, pp. 166-185 (1992)

"Information About High Technology Materials". *Dow Corning Corporation*, 10-026D-87, Michigan, USA (1987)

Ealey, M. A., Davis, P. A., "Standard SELECT electrostrictive lead magnesium niobate actuators for active and adaptive optical components". *Optical Engineering*, Vol. 29, No.11, pp.1373-1382 (1990)

Furutani, K., Urushibata, M. and Mohri, N., "Improvement of Control Method for Piezoelectric Actuator by Combining Induced Charge Feedback with Inverse Transfer Function Compensation". *Proc. of the IEEE- International Conference on Robotics & Automation*, Belgium, May 1998, pp. 1504-1509 (1998)

"Technical Information of Titanium Foil TI000460". *Standard Catalogue Product Search Menu*, Goodfellow Cambridge Limited, England (2001)

Guha, J. P., Hong, D. J., and Anderson, H. U., "Effect of Excess of PbO on the Sintering Characteristics and Dielectric Properties of $Pb(Mg_{1/3}Nb_{2/3})O_3$-$PbTiO_3$-Based Ceramics". *Journal of the American Ceramic Society*, Vol. 71 [3], pp. C152-C154 (1988)

Gupta, S. M. and Kulkarni, A. R., "Role of excess PbO on the microstructure and dielectric properties of lead magnesium niobate". *Journal of Materials Research*, Vol. 10, No. 4, pp. 953-961 (1995)

Haines, P. J., "Thermogravimetry". In Haines, P. J., ed., *Thermal Methods of Analysis: Principles, Applications and Problems*, Blackie Academic & Professional, London, pp. 22-23 (1995)

Harrison, W. B., McHenry, K. D. and Koepke, B. G., "Monolithic Multilayer Piezoelectric Ceramic Transducer". *Proc. of the 6th IEEE Symposium on Application of Ferroelectric, Bethlehem, PA*, pp. 265-272 (1986)

Hartmann, B., "Ultrasonic Measurements". *Method of Experimental Physics*, Vol. 16C, Academic Press, N.Y., USA, pp.59-90 (1980)

Hom, C. L., Pilgrim, S. M., Shankar, N., Bridger, K., Massuda, M. and Winzer, S. R., "Calculation of Quasi-Static Electromechanical Coupling Coefficients for Electrostrictive Ceramic Materials". *IEEE Tran. On Ultra., Ferro., and Freq. Control*, Vol. 41, No. 4, pp. 542-551 (1994)

Im, I. H., Chung, H. S., Paik, D. S., Park, C. Y., Park, J. J., "Multilayer piezoelectric actuator with AgPd internal electrode". *Journal of the European Ceramic Society*, Vol. 20, pp. 1011-1015 (2000)

Jaffe, B., Cook, W. R. and Jaffe, H., "Manufacture of Piezoelectric Ceramics". In Roberts, J. P., Pepper, P., eds., *Piezoelectric Ceramics*, Academic Press, London, pp. 253-263 (1971)

Kahn, M., Krause, D. and Chase, M., "Flaw Detection in d_{33} Mode Multilayer Ceramic Actuators Using Impedance-Frequency Scans". *Materials Evaluation*, pp.749-754 (1996)

Kahn, S. R, and Checkaneck, R. W., "Acoustic emission testing of multilayer ceramic capacitors", *IEEE Trans. Compon., Hybrids, and Manuf. Technology*, CHMT-6, Vol. 14, pp.517-526 (1983)Kamm, L. J., "Understanding Electro-mechanical engineering- An introduction to mechatronics". *IEEE Press*, New York (1996)

Kaizuki, H. et al., "A Simple Way to Reduce Hysteresis and Creep When Using Piezoelectric Actuators". *Japanese Journal of Applied Physics*, Vol.27, No. 5, pp. L773-L776 (1988)

Kang, D. H., Yoon, K. H., "Dielectric properties due to excess PbO and MgO in Lead Magnesium Niobate Ceramics". *Ferroelectrics*, Vol. 87, pp. 255-264 (1988)

Kenji, W., Isamu, Y., Yasushi, I., "Wire Clamping Device". *Japanese Patent*, No. 57159034 (1982)

Kuniyuki, T., Koichi, H., "Wire Clamper". *U.S. Patent*, No. 5388751 (1995)

Kusumoto, K., Sekiya, T., "Processing and properties of

$(1-x)Pb(Mg_{1/3}Nb_{2/3})O_3$-$xPbTiO_3$ solid solutions from PbO- and MgO- excess compositions". *Materials Research Bulletin*, Vol. 33, No.9, pp.1367-1375 (1998)

Leary, S. P. and Pilgrim, S. M., "Determination of Nonlinear Electromechanical Energy Conversion and the Field-Dependent Elastic Modulus of $Pb(Mg_{1/3}Nb_{2/3})O_3$-Based Electrostrictors". *IEEE Transactions on Ultra., Ferro. and Freq. Control*, September 1999, Vol.46 No.5, pp.1155-1163 (1999)

"MatWeb Materials Property Database-Titanium Grade 1". *MatWeb* (2001)

Minoru, T., Koichi, H., Takayuki, L., "Clamping Device". *U.S. Patent*, No. 5746422 (1998)

Minoru, T., Takayuki, I., "Wire Clampers". *U.S. Patent*, No. 5435477 (1994)

Moilanen, H., Lappalainen, J. and Leppavuori, S., "Development of piezoelectric micromovement actuator fabrication using a thick-film double-paste printing method". *Sensors and Actuators*, A43, pp.357-365 (1994)

Moilanen, H., Leppavuori, S. and Uusimaki, A., "Fabrication of piezoelectric thick-film low-voltage multilayer actuators using a new double-paste printing technique". *Sensors and Actuators*, A37-38, pp.106-111 (1993)

"MTI-2000 Fotonic Sensor Instruction Manual". *Mechanical Technology Inc.*, USA (1991)

Newcomb, C. V. and Flinn, I.. "Improving The Linearity of Piezoelectric Ceramic Actuators". *Electronics Letter*, Vol. 18, No.11, pp. 442-444 (1982)

Ng, W. Y., "Studies of PZT/P(VDF-TrFE) 0-3 Composite". *MPhil. Thesis*, The Hong Kong Polytechnic University (2001)

Nobuto, Y., Minoru, T., Koichi, H., Mitsuaki, S., Takayuki, I., "Wire Clamper". *U.S. Patent*, No. 5323948 (1994)

Nomura, S. and Uchino, K., "Electrostrictive Effect in $Pb(Mg_{1/3}Nb_{2/3})O_3$-type

Materials". *Ferroelectrics*, Vol. 41, pp.117-132 (1982)

Okazaki, Y., "A Micro-positioning Tool Post Using A Piezoelectric Actuator for Diamond-turning Machines". *Prec. Eng.*, Vol. 12, No. 3, pp. 151-156 (1990)

Or, S. W., "High Frequency Transducer For Ultrasonic Bonding". *Ph. D. Thesis*, The Hong Kong Polytechnic University (2001)

Ousten, Y., Carbonne, B., Xiong, N. and Danto, Y., "Evaluation of Ceramic Chip Capacitors Using Acoustic Microscopy and Electrical Impedance Analysis". *CART's*, pp.138-142 (1990)

Pan, W. Y., Gu, W. Y., Taylor, D. J. and Cross, L. E., "Large Piezoelectric Effect Induced by Direct Current Bias in PMN:PT Relaxor Ferroelectric Ceramics". *J. Journal of Appl. Phys.*, Vol. 28, No. 4, pp.653-661 (1989)

"Theory and Applications of Piezo Actuators and PZT NanoPositioning Systems". *Physik Instrumente*, Germany (2001)

"PKI data sheet". *Piezo Kinetics Inc.*, USA (2001)

Pilgrim, S. M., Bailey, A. E., Massuda, M., Poppe, F. C., Ritter, A. P., "Fabrication and Characterization of PZT Multilayer Actuators". *Ferroelectrics*, Vol. 160, pp.305-316 (1994)

"Vibrometer Operator's Manual for Polytec Vibrometer Series 3000". *Polytec*, Germany (1998)

Read, B. E. and Dean, G. D., "The Ultrasonic Immersion Method". *The Determination of Dynamic Properties of Polymers and Composite*, Adam Hilger (1978)

Richerson, D. W., "Modern Ceramic Engineering, properties, processing, and use in design". *Marcel Dekker, Inc.*, New York (1982)

Riley, W. F., Dally, J. W., McConnell, K. G., "Instrumentation for Engineering Measurements". *John Wiley & Sons Inc.*, New York (1981)

Ritter, A. P., Bailey, A. E., Poppe, F., Galvagni, J., "Fabrication of multilayer ceramic actuators". In Knowles, G. J. ed., *Act. Matl. Adap. Struct.. Proceedings of the ADPA/AIAA/ASME/SPIE Conference*, Alexandria, VA, USA, 4-8 Nov. 1991, Vol. 36, pp.693-696 (1992)

Sawyer, C. B. and Tower, C. H., "Rochelle Salt as a Dielectric". *Physical Review*, Vol. 35, pp. 269-273 (1930)

Shrout, T. R., Fielding, J. Jr., "Relaxor Ferroelectric Materials". *IEEE Proc. of Ultra. Symp.*, pp.711-720 (1990)

Shrout, T. R., Halliyal, A., "Preparation of Lead-Based Ferroelectric Relaxors for Capacitors", *American Ceramic Society Bulletin*, Vol. 66 [4], pp. 704-711 (1987)

Shrout, T. R., Kumar, U., Megherhi, M., Yang, N. and Jang, S. J., "Grain Size Dependence of Dielectric and Electrostriction of $Pb(Mg_{1/3}Nb_{2/3})O_3$-Based Ceramics". *Ferroelectrics*, Vol. 76, pp. 479-487 (1987)

Stutts, D. S., "A simple example of the relationship between electromechanical coupling and measured impedance". *University of Missouri-Rolla*, pp.1-8 (1995)

Swartz, S. L. and Shrout, T. R., "Fabrication of Perovskite Lead Magnesium Niobate", *Material Research Bulletin*, Vol. 17, pp. 1245-1250 (1982)

Swartz, S. L., Shrout, T. R., Schulze, W. A., and Cross, L. E., "Dielectric Properties of Lead-Magnesium Niobate Ceramics". *Journal of the American Ceramic Society*, Vol. 67 [5], pp.311-315 (1984)

Takamizawa, H., Utsumi, K., Yonezawa, M., Ohno, T., "Large capacitance multilayer ceramic capacitor". *Proceedings of the 31st Electronic Components Conference*, 1981, Vol. CHMT-4, pp.345 (1981)

Tetsutaka, K. (A), "Wire Clamping Mechanism and Wire Bonding Apparatus comprising the same mechanism". *Japanese Patent*, No. 09051012 (1997)

Tetsutaka, K. (B), Hideaki, M., "Wire Clamping Mechanism and Wire Bonding Apparatus Comprising the Same Mechanism". *Japanese Patent*, No. 09051013 (1997)

"Multilayer Piezoelectric Actuators: User's Manual". *Tokin Inc.*, Japan (1995)

Tsuchiya, H., Fukami, T., "Multilayered piezoelectric transformer". *Ferroelectrics*, Vol. 63, pp.299-308 (1985)

Tsuyoshi, S., "Wire Bonding Apparatus". *Japanese Patent*, No. 10242196 (1998)

Uchino, K., "Electrostrictive Actuators: Materials and Applications". *Ceramic Bulletin*, Vol. 65, No.4, pp.647-652 (1986).

Uchino, K., "Piezoelectric Actuators and ultrasonic motors". *Kluwer Academic Publishers*, Boston (1997)

Villegas, M. (A), Caballero, A. C., Kosec, M., Moure, C., Duran, P., and Fernandez, J. F., "Effects of PbO excess in Pb(Mg$_{1/3}$Nb$_{2/3}$)O$_3$-PbTiO$_3$ ceramics: Part I. Sintering and dielectric properties". *Journal of Materials Research*, Vol. 14, No. 3, pp. 891-897 (1999)

Villegas, M. (B), Fernandez, J. F., Caballero, A. C., Samardija, Z., Drazic, G. and Kosec, M., "Effects of PbO excess in Pb(Mg$_{1/3}$Nb$_{2/3}$)O$_3$-PbTiO$_3$ ceramics: Part II. Microstructure development". *Journal of Materials Research*, Vol. 14, No. 3, pp. 898-905 (1999)

Wang, H. C. and Schulze, W. A., "The Role of Excess Magnesium Oxide or Lead Oxide in Determining the Microstructure and Properties of Lead Magnesium Niobate". *Journal of the American Ceramic Society*, Vol. 73 [4], pp. 825-832 (1990)

Watanabe, J., Someji, T. and Jomura, S., "Fundamental Consideration of Piezoelectric Multilayer Actuators with Interdigital-Electrode-type Structure". *Japanese Journal of Applied Physics*, Vol.38, pp. 3331-3333 (1999)

Wersing, W., Schnoller, M., Wahl, H., "Monolithic Multilayer Piezoelectric Ceramics".

Ferroelectrics, Vol. 68, pp. 145-156 (1986)

Xu, Q. C., Dogan, A., Tressler, J., "Ceramic-Metal Composite Actuator". *Proc. of IEEE., Ultra Symp.*, pp.923-926 (1991)

Yao, K., Uchino, K., Xu, Y., Dong, S. and Lim, L. C., "Compact Piezoelectric Stacked Actuators for High Power Applications". *IEEE Trans. Ultrasonic Ferroelectrics, Freq. Contr.*, Vol. 47, pp.819-825 (2000).

Yao, K., Zhu, W., "Improved preparation procedure and properties for a multilayer piezoelectric thick-film actuator". *Sensors and Actuators*, A71, pp.139-143 (1998)

List of Publications

Refereed Journal Papers

[1] K. W. Tang, H. L. W. Chan, C. L. Choy, Y. M. Cheung and P. C. K. Liu, "Fabrication of 0.9PMN-0.1PT Multilayer Actuator". *Ferroelectrics*, in press (2001)

[2] Y. Zhang, K. W. Tang, P. C. K. Liu, Y. M. Cheung, H. L. W. Chan and C. L. Choy, "Fabrication of PZT Multilayer Actuator by a Two-Step Sintering Process". *Ferroelectrics*, in press (2001

[3] K. W. Tang, H. L. W. Chan, Y. M. Cheung and P. C. K. Liu, "Longitudinal Strain Response of a 0.9PMN-0.1PT Multilayer Actuator". *Journal of Materials Chemistry and Physics*, in press (2001)